A two-way approach to adapt small-scale laboratory experiments and corresponding numerical simulations of offshore seismic surveys

Bence Solymosi

ÉCOLE DOCTORALE SCIENCES POUR L'INGÉNIEUR : MÉCANIQUE, PHYSIQUE, MICRO ET NANOÉLECTRONIQUE

Thèse présentée pour obtenir le titre universitaire de Docteur d'Aix-Marseille Université

Discipline: Sciences pour l'Ingénieur
Spécialité: Acoustique

Bence SOLYMOSI

A two-way approach to adapt small-scale laboratory experiments and corresponding numerical simulations of offshore seismic surveys

–

Une approche conjointe pour adapter les expérimentations de laboratoire à échelle réduite aux simulations numériques correspondantes de campagnes de sismique marine

Soutenue publiquement le 20/11/2018 devant le jury composé de:

Hervé CHAURIS	Professeur / Mines Paris Tech	Président
Yann CAPDEVILLE	Directeur de Recherche / CNRS-LPG	Rapporteur
Donatienne LEPAROUX	Directrice de Recherche / IFSTTAR Nantes	Rapporteur
Børge ARNTSEN	Professeur / NTNU, Trondheim	Examinateur
Ivan PIRES DE VASCONCELOS	Professeur Associé / Université d'Utrecht	Examinateur
Nathalie FAVRETTO-CRISTINI	Chargée de Recherche (HDR) / CNRS-LMA	Directrice de thèse
Paul CRISTINI	Chargé de Recherche (HDR) / CNRS-LMA	Co-directeur de thèse
Dimitri KOMATITSCH	Directeur de Recherche / CNRS-LMA	Examinateur (Encadrant)
Bjørn URSIN	Professeur Émérite / NTNU, Trondheim	Membre invité

Numéro national de thèse/suffixe local: 2018AIXM0630/037ED353

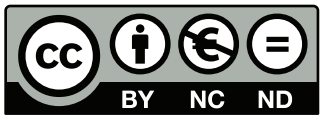

RÉSUMÉ

Les méthodes numériques sont largement utilisées en exploration sismique pour simuler la propagation des ondes et pour le post-traitement des données sismiques avant l'interprétation géologique/géophysique. Les algorithmes sont basés sur différentes hypothèses pour réduire le coût de calcul au détriment de la simplification des modèles et/ou des phénomènes physiques. En raison de leur rôle essentiel en exploration géophysique, la précision des simulations numériques présente un fort intérêt, notamment dans le cas de configurations géologiques réalistes. La comparaison directe des résultats numériques entre eux dans des configurations synthétiques peut avoir des limites, car il peut être difficile de déterminer celui qui donne la meilleure approximation de la solution physique inconnue. Comme dans la réalité le sous-sol n'est jamais connu avec précision, il est également difficile de comparer les résultats synthétiques aux données sismiques réelles acquises in situ. Par conséquent, il y a un grand intérêt à utiliser des mesures de laboratoire sur des modèles physiques aux propriétés connues pour valider la précision des outils numériques. Avant de pouvoir comparer avec précision les mesures et les simulations, nous devons tout d'abord établir un cadre comparatif avec une approche conjointe adaptée aux expériences de laboratoire et à la modélisation numérique. C'est précisément l'objectif de cette thèse. Ainsi, le cadre reproduit d'abord les mesures sismiques marines dans des conditions de laboratoire en utilisant de modèles à échelle réduite, puis les outils numériques sont adaptés à la reconstruction précise des expériences.

Le cadre est introduit pour le modèle Marseille-Benchie. Ce modèle a une topographie complexe, produisant un champ d'ondes à la fois complexe et relativement facile à appréhender. Avant de simuler numériquement la propagation des ondes par méthodes de différences finies (FDM) ou d'éléments spectraux (SEM), nous nous concentrons sur les paramètres d'entrée, tels que les propriétés du matériau et la géométrie du modèle. Les propriétés du matériau sont caractérisées en laboratoire puis calibrées pour les simulations numériques. Les caractéristiques réelles du traducteur piézoélectrique source sont modélisées en utilisant une nouvelle approche qui consiste à caractériser le traducteur, puis à effectuer une étape d'inversion pour obtenir une source numériquement équivalente. La comparaison des résultats numériques et de laboratoire révèle une bonne concordance en termes de temps d'arrivée, de phase et d'amplitude, à la fois pour la SEM et la FDM. Les différences mineures observées au niveau des amplitudes peuvent être attribuées aux imprécisions des positions du traducteur combinées à la forte topographie du modèle, au bruit présent dans les données de laboratoire, aux incertitudes liées à la source numériquement equivalente et à celles liées aux mesures d'atténuation.

Forts de ces constats, nous améliorons la procédure expérimentale avant d'étendre le cadre au modèle WAVES. Ce modèle représente une configuration géologique réaliste avec un dôme de sel enfoui dans des milieux sédimentaires. Nous utilisons la SEM pour reproduire les données de laboratoire 3D zero-offset et offset. La comparaison des résultats synthétiques avec les mesures révèle une très bonne concordance. Les différences mineures observées au niveau des amplitudes peuvent une fois encore être attribuées aux mêmes facteurs que dans le cas du modèle Marseille-Benchie.

Enfin, malgré les incertitudes qui subsistent, l'ensemble de la procédure expérimentale est validé avec succès grâce à l'application de la reverse-time migration (RTM) aux données de laboratoire. En effet, les noyaux de sensibilité RTM résultants montrent une reconstruction précise et cohérente de la plupart des discontinuités du modèle WAVES. Par conséquent, le cadre proposé peut être utilisé pour tester des techniques d'imagerie existantes ou nouvelles.

Mots clés: propagation des ondes, simulation numérique, expérience en laboratoire, reverse-time migration, sismique marine, échelle réduite, ultrasons, atténuation

ABSTRACT

Numerical methods are widely used in seismic exploration to simulate wave propagation and to post-process the recorded seismic data before the geologic/geophysical interpretation. The algorithms are based on various assumptions to reduce the computational cost at the expense of simplifying the models and/or the physical phenomena. Because of their essential role in exploration geophysics, the accuracy of the numerical simulations is of particular interest, especially in the case of realistic geologic setups. The direct comparison of the numerical results with each other in synthetic configurations can have limitations, as it can be difficult to determine the one that gives the best approximation of a physically unknown solution. Because in real life the subsurface is never accurately known, it is also difficult to compare the synthetic results to any seismic data set from field measurements. Therefore there is a strong interest in using laboratory measurements on physical models of known geometries to benchmark the numerical tools. Before comparing measurements and simulations with confidence at high accuracy, we first need to establish a comparative framework with a jointly-adapted approach to both the laboratory experiments and the numerical modeling. This challenging task is the goal of this thesis. Thus, the framework first reproduces offshore seismic measurements in laboratory conditions with the help of small-scale models, and then the numerical tools are adapted to the accurate synthetic reconstruction of the experiments.

The framework is introduced for the Marseille-Benchie model. This model has a complex topography, yielding a wavefield which is both challenging and relatively easily understandable. Prior to the finite-difference (FDM) and spectral-element (SEM) simulations, we focus on the input parameters, such as the material properties and the model geometry. The material properties are characterized in the laboratory and calibrated for the numerical simulations. The real source transducer characteristics are implemented using a new approach, consisting of the laboratory characterization of the transducer, followed by an inversion step to obtain a numerically equivalent source. The comparison of the synthetic and laboratory results reveals a good fit in terms of arrival time, phase, and amplitude, for both the SEM and the FDM, especially in zero-offset configuration. Minor amplitude mismatches (concerning mainly the offset configuration) may be attributed to the inaccuracies of the transducer positions in the laboratory combined with the strong model topography, to the noise recorded in the laboratory data, and to the uncertainties of the proposed source implementation and of the attenuation parameters.

Based on the identified sources of misfits, we improve the experimental procedure before extending the framework to the complex and multi-layered WAVES model.

This model represents a realistic geologic setup with a salt-dome in the middle. We use the SEM to reconstruct the 3D zero-offset and 3D offset laboratory measurements. The comparison of the synthetic results with the laboratory measurements reveals a very good fit for the arrival time, phase, and amplitude. Once again, the revealed minor amplitude mismatches may be attributed to the noise recorded in the laboratory data, as well as to the uncertainties of the proposed source implementation and of the attenuation parameters.

Finally, despite the remaining uncertainties, the entire framework is successfully validated through the application of reverse-time migration (RTM) to the laboratory data sets. Indeed, the resulting RTM sensitivity kernels show an accurate and coherent reconstruction of most of the discontinuities of the WAVES model. Therefore, the proposed framework can be used with confidence to test already existing or new imaging techniques.

Keywords: wave propagation, numerical simulation, laboratory experiments, reverse-time migration, offshore seismic, small-scale, ultrasonic, attenuation

ACKNOWLEDGEMENTS

First of all, I thank my main supervisor, Nathalie, for being there and encouraging me throughout the thesis, as well as for paying attention to even the smallest details of my work. I also say a big thank to my second supervisor, Paul, who was always extremely helpful to discuss any question with me.

I also thank Dimitri Komatitsch for his efforts as a tutor, as well as Vadim Monteiller and Guilherme Machado for helping me with the numerical part and the digitization of the 3D geometry files, respectively. The laboratory part was really a teamwork and I say a huge thanks to Régine, Guy, Vincent, Eric, and Philippe for tackling the challenges of the laboratory experiments with me.

Thanks to the members of the PhD defense committee, especially to the two rapporteurs, Yann Capdeville and Donatienne Leparoux, and to the president of the committee, Hervé Chauris, I received some really useful remarks.

Bjørn Ursin had helped my work even before I knew him, as he consulted Nathalie and Paul on the design of the WAVES model, and later provided me with helpful information about the challenges of (sub)salt-imaging.

I thank Børge Artsen, with who we worked together for several weeks, and who taught me a lot about finite-difference modeling.

My PhD thesis was financed by the EU through the WAVES-ITN Project. I had the opportunity to work with many PhD fellows and researchers in this project, which helped us all to form a lively network.

The WAVES model could not become a reality without the efficient and precise work of La Fonderie de Verre and VN Composites, who continuously consulted us to realize our various ideas before and during they built the physical model.

Of course, I could not finish this thesis without the support of my family, Papa, Mama, Dorka, Marci, Orsi, Petra, and Emma. Thanks to my thesis I got to know some of the nicest friends, Christophe, Clément, Jérôme, and Pierre.

Last, but not least, I thank my fellow PhD colleagues at LMA, Oumar, Mathilde, Alexis, Harold, Masaru, and Louis for the friendly ambiance throughout these three years.

TABLE OF CONTENTS

LIST OF ABBREVIATIONS

FDM: finite-difference modeling

FEM: finite-element modeling

RTM: reverse-time migration

SEM: spectral-element modeling

SNR: signal-to-noise ratio

2D: two-dimensional

3D: three-dimensional

GENERAL INTRODUCTION

The terrain below the Earth's surface plays not only an important role in supplying our society with essential resources – such as water, oil, gas, precious metals - but it has also a huge effect on our daily life through earthquakes, tsunamis, landslides, to name a few. Therefore the knowledge and the understanding of the subsurface are of particular interest. Because in-situ data about the subsurface is usually not available, we need to resort to methods that measure some physical phenomena on the Earth's surface or above that, such as in the case of radar interferometry to investigate volcanic activity (e.g. Hooper, 2008). A better understanding of the applied methods can result in both economic and environmental advantages, such as: finding resources with higher probability; drilling wells in the optimal position with better precision; better understanding the geological processes of the past and the present, and their possible future consequences; better assessing the risks of landslides, earthquakes and tsunamis on people and infrastructure (e.g. on nuclear power plants and water dams).

The general approach of geophysical exploration is summarized in Figure 1. Let us suppose that we want to understand the geological setup of a given part of the subsurface. The first step is the preparation, using all available information to make plans for the future measurements. These preliminary information may include already existing measurements (e.g., large-scale regional seismic measurements in exploration geophysics, previous ground-penetrating radar surveys or geomechanical characterization of soil samples in civil engineering); potential hypotheses about the geological history of the investigated site; and small-scale physical models to better understand the problems at laboratory scale (e.g. geodynamic modeling of the lithospheric deformation like in Dombradi et al., 2010); to name a few. Based on all the preliminary information, the necessary geophysical methods can be selected, such as seismic, gravitational and electromagnetic methods. The data acquisition can also be optimized in advance, by choosing, for example, the suitable frequency and acquisition geometry. The actual data acquisition and its subsequent processing is the second step. The details of this step are out of the scope of this thesis, but they play an essential role in the overall understanding of the subsurface. In the third step, the measured data sets are interpreted and put into a general context. Most of the time the understanding of the subsurface is a complex iterative process, using the measured data and the preliminary information as well. Usually, a theoretical model is supposed, based on the a priori information and the first interpretation of the measurements. Then the numerical simulations are conducted for this initial model and the results of

the numerical simulations (called synthetic results) are compared to the measured data. By interpreting the differences between the synthetic and the measured data, and again possibly considering the preliminary information as a constraint, the theoretical model is modified to decrease the misfit between the simulations and the measurements. By repeating these steps, we hope that the theoretical model is approaching the real-life setup. The term 'hope' is used here because the subsurface is never known exactly. Because there are numerous other parameter sets leading to the same solution (e.g. different density-velocity combinations provide the same reflectivity), this approach leads to a mathematically non-unique solution. It requires extensive knowledge and experience to choose the geologically/geophysically feasible solution out of all the mathematically possible ones.

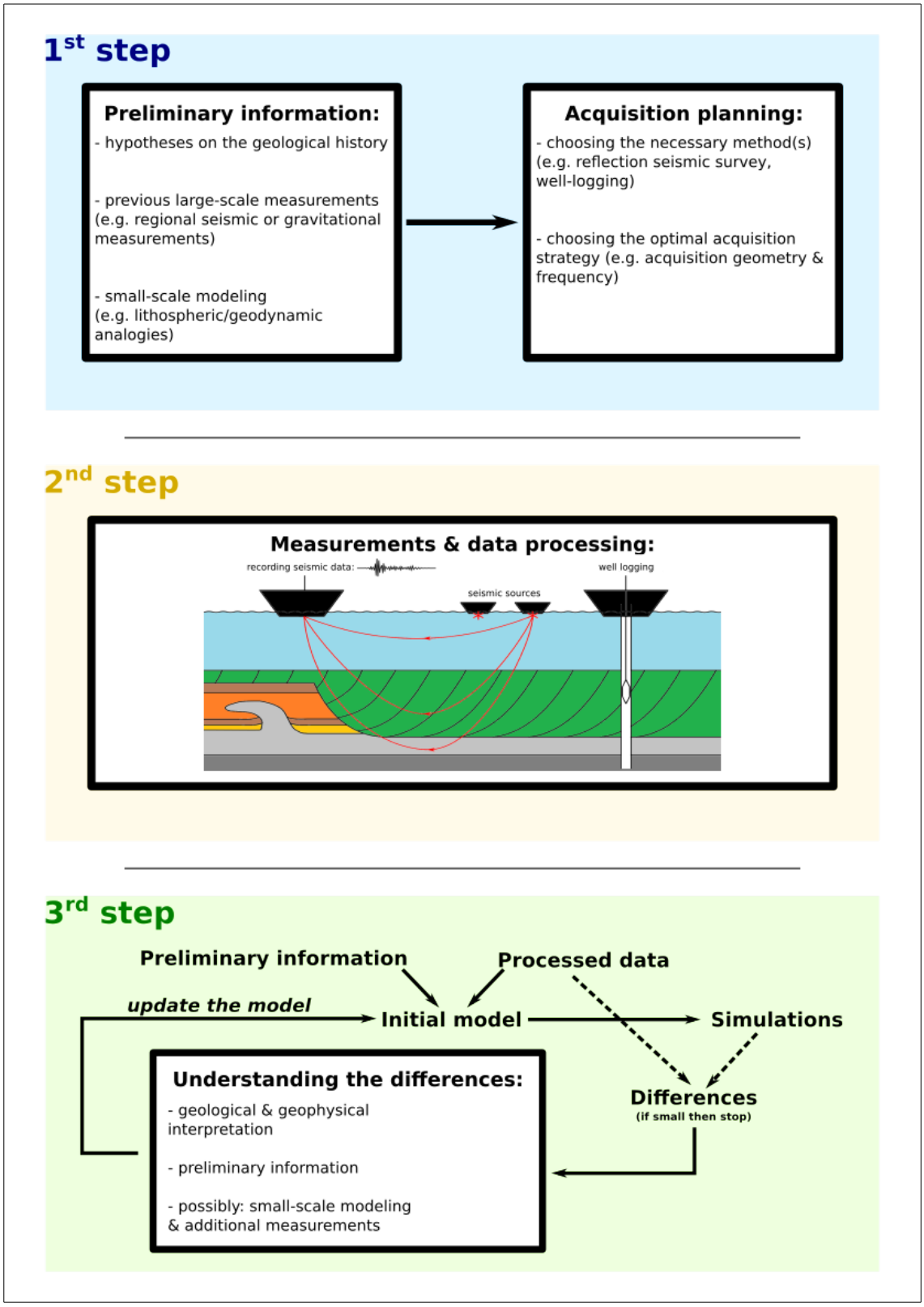

Figure 1. Flowchart of a typical exploration geophysics project from the initial planning phase to the understanding of the subsurface.

As mentioned above, numerous geophysical methods can be used to investigate the subsurface, but the seismic/seismological method is one of the most generally used (e.g. Ikelle and Amundsen, 2005). *Seismology* is the term used for regional and global scale applications, such as the investigation of the structure of the Earth's interior, global seismicity or earthquake epicenter determination. *Seismic* is the term used in exploration geophysics at a rather local scale (e.g., for hydrocarbon exploration, water extraction, CO_2 storage); and in engineering geophysical applications (e.g., for near-surface mapping for civil engineering and archaeological applications). Although 'seismic' and 'seismology' are two terms practically denoting the same method, which uses seismic waves propagating in the subsurface from either natural or artificial sources, they utilize different frequencies[1]. The seismic method is widespread in applied geophysics due to the possibility to image even deeply overburden structures, as well as the high resolution of the measured data. The method is especially efficient on the sea, where a large area can be surveyed in a short period of time.

Seismic exploration uses the so-called wave equation to describe the propagation of the seismic waves in the subsurface. The analytical solution of this equation can be deduced only for rather simple models, such as a homogeneous, isotropic half space (e.g., Lamb, 1904, de Hoop, 1958), or a layer-cake geologic model (e.g. Kennett, 1981). However, these simple models do not represent the complexity of the real life, e.g. an arbitrary 3D geometry with complex material properties, including heterogeneities, anisotropy, and numerous thin interbedded layers. Therefore exploration geophysics relies heavily on numerical tools to approximate the solution of the governing equations for realistic geologic setups. Numerical algorithms are used in seismic exploration during survey design, data processing and interpretation (e.g. Robertsson et al., 2007), as well as in seismic imaging and inversion (e.g., Chauris and Benjemaa, 2010, Virieux et al., 2011). Conventional methods (e.g., ray-tracing, Kirchhoff integral, and finite-difference methods), widely used in seismic exploration, are efficient to simulate realistic wavefields in environments with simple structures and slowly-varying material properties. However, difficulties arise for environments with large and rapid structural changes, as well as in the presence of shadow zones and (multiple) diffractions. Thus, different methods have been developed to improve seismic modeling in realistic geologic environments, including steeply-dipping faults, curved interfaces, salt bodies, etc. (e.g. Mittet, 2017).

1 Typical frequency ranges: 0.1-4 Hz in seismology, and 4-150 Hz in seismic exploration.

Before real applications, newly developed numerical algorithms are typically tested against other numerical methods using synthetic configurations. Several projects have focused on the comparison and validation of the different numerical results (e.g., Igel et al., 2000, Moczo et al., 2006, 2010, Fehler and Keliher, 2011, Chaljub et al., 2015). Since each numerical algorithm is based on mathematical assumptions – i.e. to some extent simplifying the underlying physics and/or the geometry of the real life to save computational cost –, their direct comparison for realistic and complex models can have limitations, as it can be difficult to determine the one that gives the best approximation of a physically unknown solution. Therefore there is a strong interest in using physical data sets to benchmark synthetic results. However, because in real life the subsurface of the Earth is never accurately known, it is difficult to compare the synthetic results with any seismic data set from field measurements.

An alternative approach to test and validate the performance of the numerical methods in realistic cases can be the comparison of the synthetic results with experimental data, obtained for a small-scale physical model in laboratory conditions. This implicitly assumes that the scaled physical mechanisms are identical to those at seismic scale (Ebrom and McDonald, 1994), and this assumption is fulfilled in the case of the linear wave equation. Considered as obsolete in the 1990's – essentially due to the drastic increase in computing capacities –, laboratory experiments have recently been re-introduced into the ideas-to-applications pipeline. The laboratory can be considered as a halfway point between numerical modeling and field observations. Indeed, laboratory experiments are repeatable, more controllable than real seismic surveys, versatile in terms of the acquisition setup and provide high-quality data for a known configuration. Furthermore, similar to real seismic acquisitions and unlike some numerical data, laboratory measurements contain random and signal-generated noise, multiples, mode conversions, and uncertainties due to position inaccuracies. As these sources of noise and uncertainties can be better assessed than in the case of field data sets, the laboratory experiments are valuable tools to validate numerical simulations against real physical data sets.

Initially, small-scale physical modeling was extensively developed for a better understanding of the underlying physics of seismic wave propagation (e.g, Wapenaar and Berkhout, 1987, Pant et al., 1992), and for the validation of theoretical predictions (Favretto-Anrès and Rabau, 1997). Laboratory experiments are still used nowadays to investigate physics that is not sufficiently understood to be numerically modeled with confidence (Cooper et al., 2010, Stewart et al., 2012, Ekanem et al., 2013, Xu et al., 2016, Chang et al., 2017). Data from laboratory experiments are also used as input to inverse problems (Pratt, 1999, Favretto-Anrès and Sessarego, 1999, Bretaudeau et al., 2013, Chai et al., 2015), to test new data processing algorithms (Campman et al., 2005), and in time-lapse 3D studies (Sherlock et al., 2000). More recently, small-scale modeling has been used again as another tool to validate numerical modeling and seismic imaging methods in the context of onshore and offshore seismics (Bretaudeau et al., 2011, Favretto-Cristini et al., 2014, 2017, Tantsereva et al., 2014a, b, Pageot et al., 2017, Solymosi et al., 2018). In particular, by using physical measurements of wave propagation for a known model (considered as the reference data), and by investigating any misfit between the measurements and the simulations, it has been shown that there is a need for further development of the numerical tools, in order to obtain more accurate results in specific complex configurations (e.g. in the case of strongly curved interfaces). These works thus clearly show the advantage of the laboratory data sets as part of the benchmarking options for numerical algorithms.

These works also highlight the fact that an efficient benchmarking procedure requires a carefully chosen and jointly-adapted approach to both the laboratory experiments and the numerical modeling. On the one hand, the numerical tools must be adapted to the experimental configuration (e.g., implementing the real source characteristics, material properties, and acquisition conditions). On the other hand, the laboratory experiments have to be carried out keeping in mind the capabilities of the numerical tools (e.g. choosing the acquisition geometry such that the future computational cost will be the lowest possible). In addition, experimental uncertainties must be identified and subsequently minimized in order to obtain high-quality data, and numerical simulations may also contribute to this identification. As a consequence of this two-way adaptation, we always need to keep in mind the experimental and numerical aspects, for example, in the choice of the scaling factor, material properties or model geometry. Establishing a framework, which ensures an efficient reconstruction of the laboratory measurements with numerical simulations, using small-scale physical models with a geologically relevant geometry and material properties, is therefore essential in order to better understand the capabilities, limitations and possible future developments of the numerical tools. This highly challenging task is the goal of this

PhD thesis. More specifically, we do a cross-validation of the laboratory experiments and the numerical simulations to discover the points to be improved on both sides of the framework.

In this work, two small-scale models have been used: the Marseille-Benchie model and the WAVES model. The Marseille-Benchie model has a complex topography and is made out of one material with a flat bottom surface. Therefore a complex wavefield can be obtained, including reflections, diffractions, and multiples, but the interpretation of the measurements is relatively straightforward. This is advantageous for the calibration phase when the framework is established. Following that, the WAVES model provides a challenging task by closely representing both the geometry and the material properties of a realistic 3D geologic setup. The model consists of a salt-dome in the middle, surrounded by several sedimentary layers of varying material properties, including a zone with an inverted velocity profile (where the velocity decreases with depth). The geometry of this model was motivated by the difficulties encountered in seismic exploration concerning the salt structures.

For the numerical simulations, we resorted mainly to the spectral-element modeling (SEM) as a full-wave method, which is not based on strong underlying assumptions, as opposed to for instance the discretized Kirchhoff integral method (e.g., Tantsereva et al., 2014a, Favretto-Cristini et al., 2017). The SEM becomes more and more popular with time in the seismic community since it is well-suited for high-performance computing (Komatitsch et al., 2003). As it combines the accuracy of a pseudo-spectral method with the flexibility of a finite-element method, the SEM allows the handling of complex geometries by using a non-structured mesh and different element sizes in the computational domain (Komatitsch and Tromp, 2002, Oliveira and Seriani, 2011). Because the necessary trade-off between accuracy and computational cost is usually sought-after, we are also interested in the ability of the SEM to accurately simulate complex 3D wavefields including (multiple) diffractions at the lowest possible computational and man-hour cost. Few papers are devoted to the comparison of the SEM with other numerical methods (e.g., Capdeville et al., 2002, 2003, Moczo et al., 2010, De Basabe and Sen, 2014, Chaljub et al., 2015). Pageot et al. (2017) recently compared laboratory and synthetic data sets in an onshore configuration to investigate surface wave propagation and amplitude transformation between 2D and 3D. But to the best of our knowledge, no paper compares laboratory data with 3D SEM results in offshore configuration. As part of

our collaboration within the WAVES ITN Project[2] and more specifically with Børge Arntsen (NTNU, Trondheim, Norway), we also compared some of the SEM and laboratory data sets with finite-difference results. The goal of the comparison was to benchmark the finite-difference code developed at the NTNU, as well as to investigate the necessary computational cost of the different numerical methods to reach a given accuracy in reconstructing the laboratory measurements. Finite-difference modeling (FDM) is the most widely used numerical method in seismic exploration and is also a full-wave method. The FDM is based on a different approach to spatial discretization than the SEM, as it can only consider structured grids, which do not explicitly honor the discontinuities (e.g., Virieux, 1984, 1986, Holberg, 1987, Mittet 2002).

In seismic exploration the migration of the acquired field data is essential to account for the fact that seismic data is always recorded in the time domain, in which the geometry of the subsurface is not represented correctly. Numerous imaging techniques exist and the choice of the algorithm depends, for example, on the type of the data set to be processed, as well as on the complexity of the geologic setup (e.g. Yilmaz, 1987). The result of the seismic migration is a data set in the depth domain which can be used for the mapping of subsurface discontinuities, geologic formations, and potential hydrocarbon reservoirs, to name a few. In this thesis, we use one of the most common seismic imaging techniques, the reverse-time migration (RTM). The RTM is based on the imaging principle (Claerbout, 1971), and it is capable to reconstruct the reflectors related to reflection coefficient contrasts (e.g., Zhang et al., 2003, Zhu et al., 2009). Applying the RTM to the laboratory data measured for a small-scale model is an optimal benchmarking opportunity for the established framework. More specifically, if the resulting RTM data set shows a precise reconstruction of the known model geometry, then it suggests a successful validation of the entire framework, including the laboratory measurements and their numerical implementations.

---

2 This work is one of the fifteen theses of the WAVES ITN Project (2015-2018), funded by the European Commission through Horizon 2020. The participants include Sorbonne Université, University of Edinburgh, Norwegian University of Science and Technology (NTNU), Delft University of Technology (TU Delft), University of Oxford, Centre National de la Recherche Scientifique (CNRS), Institut National de la Santé et de la Recherche Médicale (INSERM), Schlumberger Cambridge Research Ltd., Eidgenössische Technische Hochschule Zürich (ETH), Shell Global Solutions International, École Supérieure de Physique et de Chimie Industrielle (EPSCI), Columbia University (ColU), Ludwig-Maximilians-Universität München, Universitetet I Oslo, and Statoil.

The manuscript is divided into two parts.
Part 1 (entitled 'Framework for the high-precision reconstruction of the laboratory measurements with numerical simulations - the Marseille-Benchie model as a tool') discusses in details all the preparatory steps used to elaborate the framework. First, Chapter 1 introduces the Marseille-Benchie model, the experimental setup and the interpretation of the laboratory data sets. Note that the laboratory techniques to characterize the properties of the material of the model, together with the measured values at different frequencies and their associated uncertainties are presented in Appendix A. Then in Chapter 2 the basics of the applied numerical methods are discussed, as well as the meshing, the numerical implementation of the real transducer characteristics, and the numerical calibration of the material properties. Note that we propose an optimization technique for the non-structured meshing of the spectral-element simulations to reduce the computational cost while keeping the same level of accuracy in Appendix B. In Chapter 3 the laboratory measurements are compared with the synthetic results. Chapter 4 is dedicated to the discussion of the (mis)fits between the data sets. Finally we draw the conclusions, as well as some necessary short-term and long-term improvements are proposed to decrease the identified misfits.

Part 2 is entitled 'Application to a realistic geologic setup – the WAVES model'. Chapter 1 introduces the WAVES model, including its geometry and the most important material properties (see also Appendix A); as well as the improvement of the experimental setup compared to Part 1. The interpretation of some of the laboratory data sets is also presented here. Chapter 2 is dedicated to the numerical aspects, discussing the numerical implementation of model geometry, and the calibration of the material properties for the multi-layered geometry. In Chapter 3 the laboratory measurements are compared with the synthetic results, and the (mis)fit between the two is also discussed in details. In Chapter 4 we showcase the RTM as an example of the possible seismic imaging techniques that can be tested using the WAVES model, including the necessary laboratory measurements and the resulting sensitivity kernels. Finally, the conclusions and perspectives are presented.

The manuscript ends with general conclusions and perspectives regarding both the experiments and the numerical tools, including a proposal for new imaging techniques to be tested with the help of the proposed framework.

We note that some parts of this manuscript are included in (submitted or) already published works:

- Solymosi, B., Favretto-Cristini, N., Monteiller, V., Cristini, P., Ursin, B., Komatitsch, D., and Arntsen, B., 2017, Comparing spectral-element numerical results with laboratory data: an example for a topographical model: 79th EAGE Conference & Exhibition, Extended Abstract, EAGE, We B4 02.

- Solymosi, B., Favretto-Cristini, N., Monteiller, V., Komatitsch, D., Cristini, P., Arntsen, B., and Ursin, B., 2018, How to adapt numerical simulation of wave propagation and ultrasonic laboratory experiments to be comparable - A case study for a complex topographic model: Geophysics, **83**(4), T195-T207.

PART 1

FRAMEWORK FOR THE HIGH-PRECISION RECONSTRUCTION OF THE LABORATORY MEASUREMENTS WITH NUMERICAL SIMULATIONS - THE MARSEILLE-BENCHIE MODEL AS A TOOL

PART 1

Introduction

As mentioned in the General Introduction, previous works (e.g., Bretaudeau et al., 2011, Favretto-Cristini et al., 2014, 2017, Tantsereva et al., 2014a, b, Pageot et al., 2017) have highlighted the need for a framework if numerical simulations are meant to be compared with laboratory measurements with high confidence and accuracy. This framework must be concerned with both the laboratory ultrasonic measurements on small-scale physical models in order to mimic offshore seismic surveys and the accurate numerical reconstruction of these experiments. The goal of this part is therefore to elaborate this framework.

We use the Marseille-Benchie model, which is based on French's model (French, 1974), but also includes additional structures with steep flanks, sharp edges, corners, and curved interfaces. This geometry enhances multiple reflections and diffractions, as well as shadow zones and interactions between the different structures. This complexity provides a significant challenge to any numerical method to reproduce the wavefield. The model has already been used in previous works. In particular, Tantsereva et al. (2014a) evaluated the ability of the 3D discretized Kirchhoff integral method (DKIM) to accurately simulate complex diffractions using a zero-offset laboratory data set measured for this model. The comparison of the numerical and laboratory data sets showed that the DKIM could correctly reproduce the wavefield, except in the vicinity of secondary shadow boundaries, created by the interaction with the edges of the topographic structures. As a follow-up, Favretto-Cristini et al. (2017) quantitatively analyzed the effect of multiple scattering and surface curvature on the wavefield, in order to define the cases where these effects may be neglected in the numerical modeling without a significant loss of the overall accuracy. As the results of Tantsereva et al. (2014a) and Favretto-Cristini et al. (2017) show, the Marseille-Benchie model has been proved to be a suitable tool to validate the results of the numerical tools and point out the necessary future developments. Therefore we also chose this model for the elaboration of the framework presented in this thesis.

This part is divided into three chapters.
Chapter 1 is dedicated to the laboratory aspects of the framework. In Section 1.1 the geometry of the small-scale physical model is introduced, as well as its most important material properties. The experimental setup is presented in Section 1.2 together with the characteristics of the ultrasonic transducers. Then some exemplary cross-sections from the laboratory data sets in both zero-offset and offset configurations are interpreted in Section 1.3.

PART 1

Chapter 2 contains the numerical aspects, starting with the introduction of the numerical algorithms commonly used in seismic exploration (Section 2.1). Then in Section 2.2, the spectral-element modeling (SEM) is presented as the primary numerical method used in this thesis. This section focuses on the most important aspects of the method, such as the weak form of the seismic wave equation, its approximation by the polynomial basis functions, the applied integral quadrature, the time-stepping scheme, the stability condition, the implementation of the point source, and the boundary conditions. The main contribution of our work is the numerical implementation of the physical transducers, including a laboratory characterization and a subsequent inversion process, is also detailed here. Section 2.3 is dedicated to the adaptation of the Specfem software package to our framework, including the non-structured hexahedral meshing of the model geometry, the implementation of the viscoelasticity, and the numerical calibration of the material properties used for the simulations.

The comparison of the synthetic results with the laboratory measurements is presented in Chapter 3. 3D zero-offset and 3D offset cases are compared, using both the spectral-element and the finite-difference algorithms. The general good fit between synthetic and laboratory traces are showcased for both methods. The misfits between the numerical and physical results are also discussed in details, as well as the differences between the numerical results obtained with the two numerical approaches.

Chapter 1
Small-scale seismic experiments

1.1 The small-scale physical model

The Marseille-Benchie model was designed to represent a moderately complex geometry, as it contains various topographic features, such as a dome, a truncated smaller dome, a truncated pyramid and two flat parts separated by a ramp (Figure 2). The model is entirely made of polyvinyl chloride (PVC), which was chosen because its properties are considered to be close to those of the typical sedimentary layers. Table 1 shows the measured properties of the PVC (together with the associated uncertainties), which is considered to be a homogeneous, isotropic and viscoelastic material. These values are valid for the frequency range of interest of this thesis, namely 250-650 kHz (see Appendix A). A scaling factor of 1:20 000 was used to scale down the real-life dimensions of typical seismic setups to the laboratory scale. Hence the experimental frequency of 500 kHz corresponds to a seismic frequency of 25 Hz, and an experimental distance of 1 mm corresponds to 20 m at seismic scale. The velocities and density of the material are not affected by the scaling, however, the attenuation can vary significantly with the frequency, as it is generally higher for materials used for laboratory experiments than in the case of real geologic formations. Because exploration geophysics, and therefore the numerical tools used in seismic exploration as well, rely on Q-factors instead of the direct attenuation values, we present Q-factors hereafter (see Appendix A). The model has a size of 600 x 400 mm^2, corresponding to 12 x 8 km^2 at seismic scale. Its thickness varies between 30-70 mm, depending on the geometry. The radii of the dome and the truncated dome are both 100 mm, and the base of the pyramid is 90 x 90 mm^2 (Figure 2).

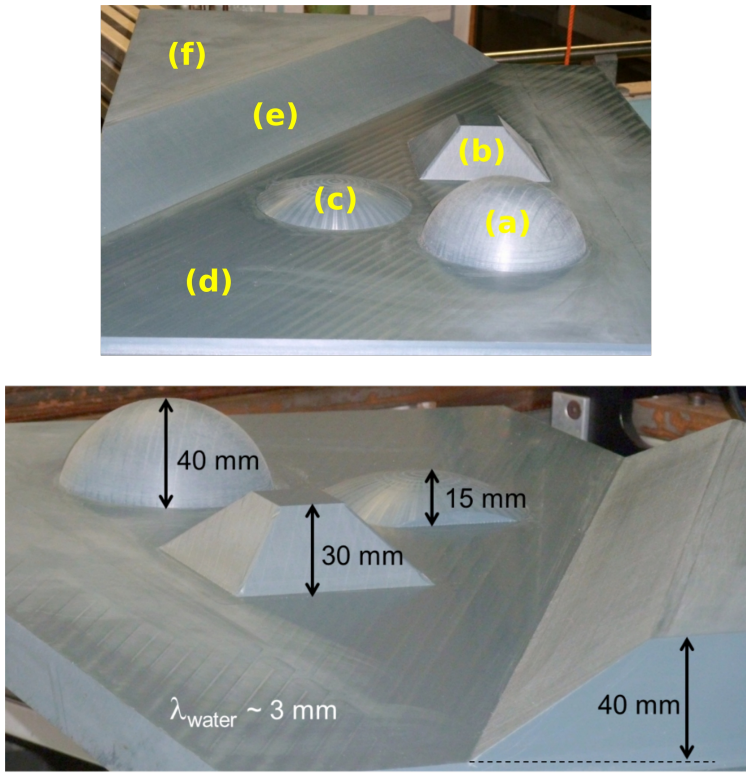

Figure 2. The Marseille-Benchie model. (Top) Its topography: dome (a), truncated pyramid (b), truncated dome (c), flat part (d), ramp (e) and elevated plateau (f). (Bottom) The height of the objects.

Density (kg/m^3)	**V_p (m/s)**	**V_s (m/s)**	**Q_p**	**Q_s**
1440 ± 10 (± 0.7 %)	2205 ± 20 (± 0.9 %)	1056 ± 462 (± 44 %)	86 ± 1 (± 1.1 %)	13 ± 9.6 (± 73 %)

Table 1. Properties of the PVC for the frequency range of interest (250–650 kHz), and the associated uncertainties.

1.2 Experimental setup and data acquisition

The model was immersed in a water tank during the measurements (Figure 3). The tank is equipped with a computer-controlled acquisition system that allows for the accurate positioning of the source and the receiver transducers. At the time of the laboratory measurements for the Marseille-Benchie model, there was no a posteriori control of the precision of the transducer movements by optical rulers, so the precision was assumed to be ±0.5 mm (i.e. ±10 m at seismic scale). The water

temperature was continuously monitored during the measurements (with an accuracy of ±0.1°C), providing an accurate knowledge of the speed of sound waves in water, typically around 1480 m/s. The precision of the measurement of the water speed is ±0.01785 m/s. Water was considered to have a density of 1000 kg/m^3 and a negligible attenuation.

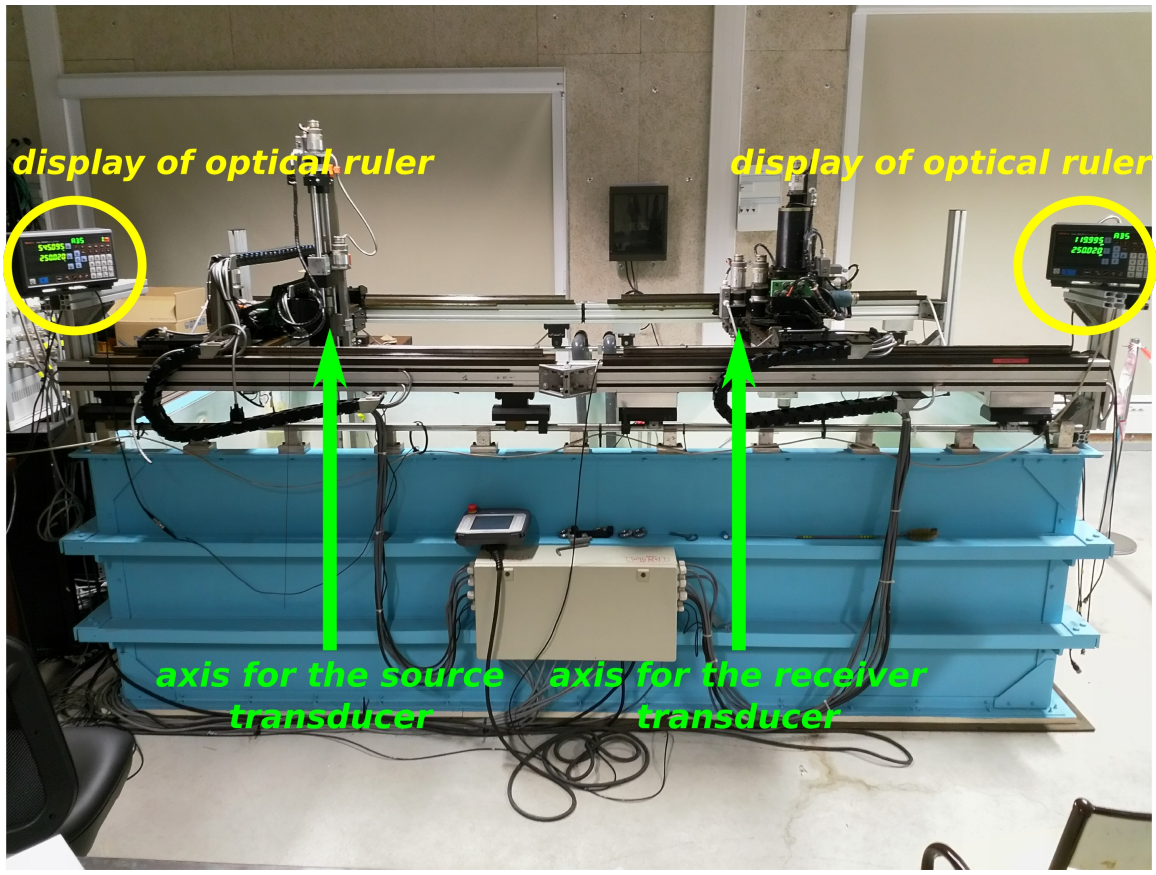

Figure 3. The water tank used for the experiments. Transducers can be attached to two axes, and the three-dimensional movement of each transducer is ensured by stepping-motors, controlled by a PC. The recently installed optical rulers provide a posteriori control of the transducer movements.

A conventional pulse-echo technique (Figure 4) was used to collect reflection data in both zero-offset and offset configurations (Figure 5). Zero-offset measurements were performed by using a custom-made Imasonic® transducer as both the source and the receiver. It has a diameter of 3 mm and was located 180±0.5 mm above the flat part of the model (labeled as (d) in Figure 2), corresponding to 3.6 km at seismic scale. The transducer has a dominant frequency of 500 kHz, and – contrary to the conventional transducers – a broad-beam radiation pattern, as the width of the main lobe is 35° at -3 dB. This radiation pattern allows for a large area to be illuminated and therefore more

3D effects to be captured (Tantsereva et al., 2014a), such as the interaction of the waves with multiple topographic features and multiple wave scattering (Favretto-Cristini et al., 2017) (Figure 6). The source signal and its associated frequency spectrum for the frequency range of interest are shown in Figure 7.

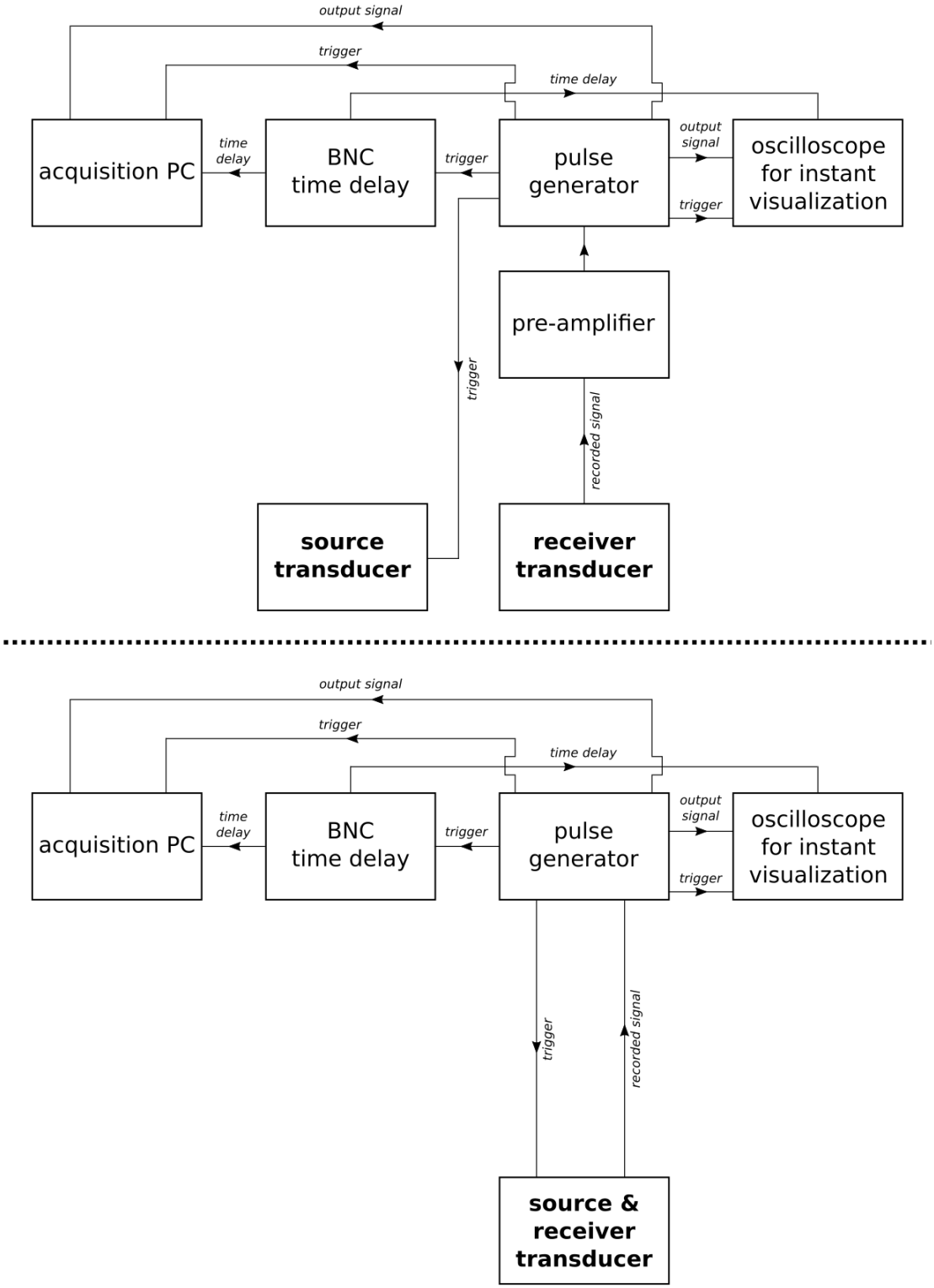

Figure 4. Sketch of the acquisition system in the offset (top) and zero-offset (bottom) configurations. The BNC time delay is used to increase the dynamics of the recorded signal.

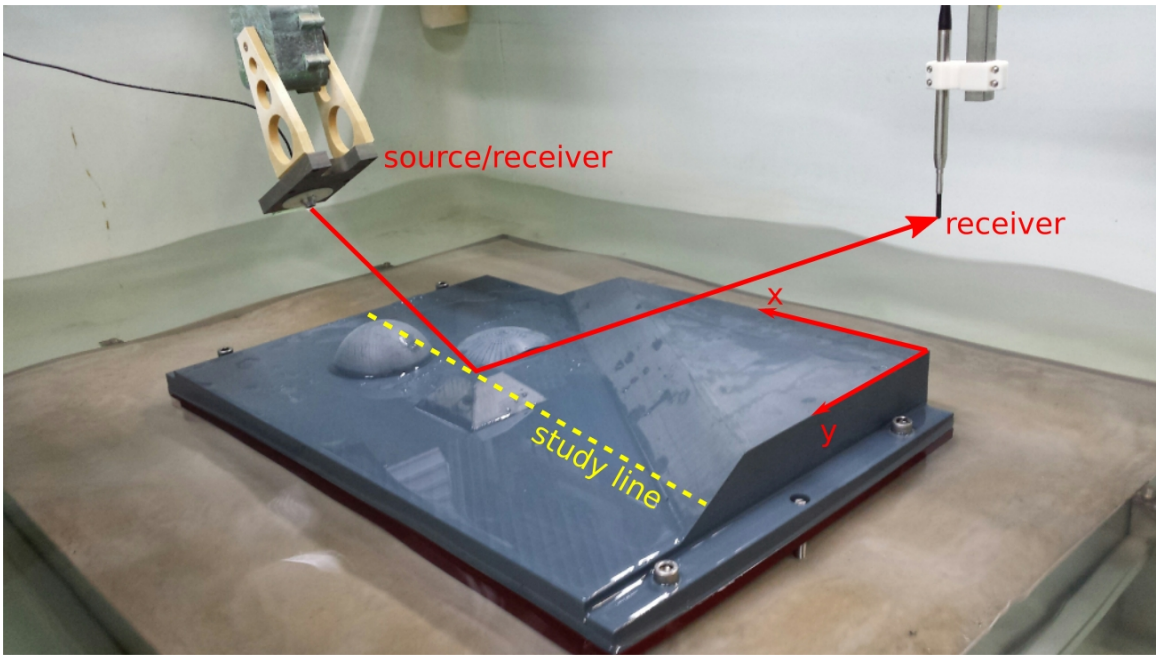

Figure 5. Illustration of the small-scale seismic experiments performed in the water tank. The model is illuminated by a piezoelectric transducer (left). The wavefield is recorded by a hydrophone (right) in the offset configuration. In the zero-offset configuration, the piezoelectric transducer is used also as the receiver.

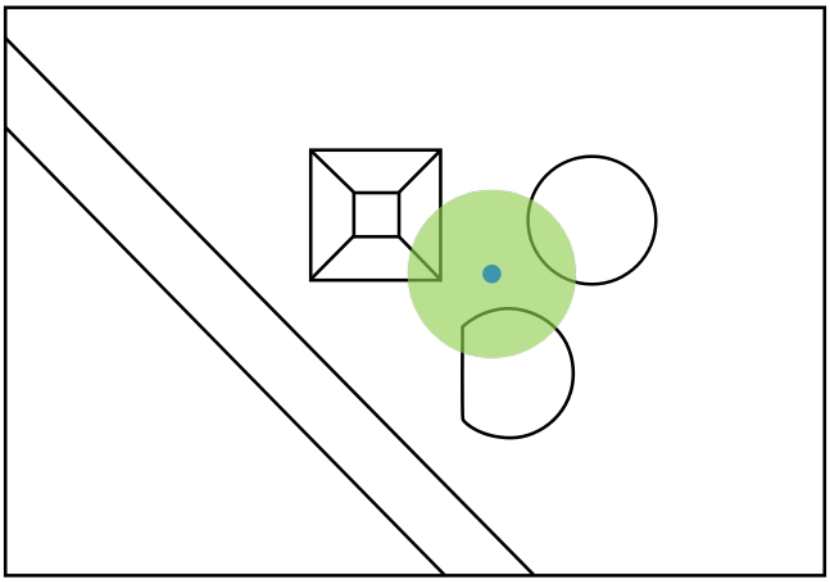

Figure 6. Illustration of the illumination area superimposed on the Marseille-Benchie model for a conventional narrow-beam transducer (blue) and the broad-beam Imasonic® transducer used in this thesis.

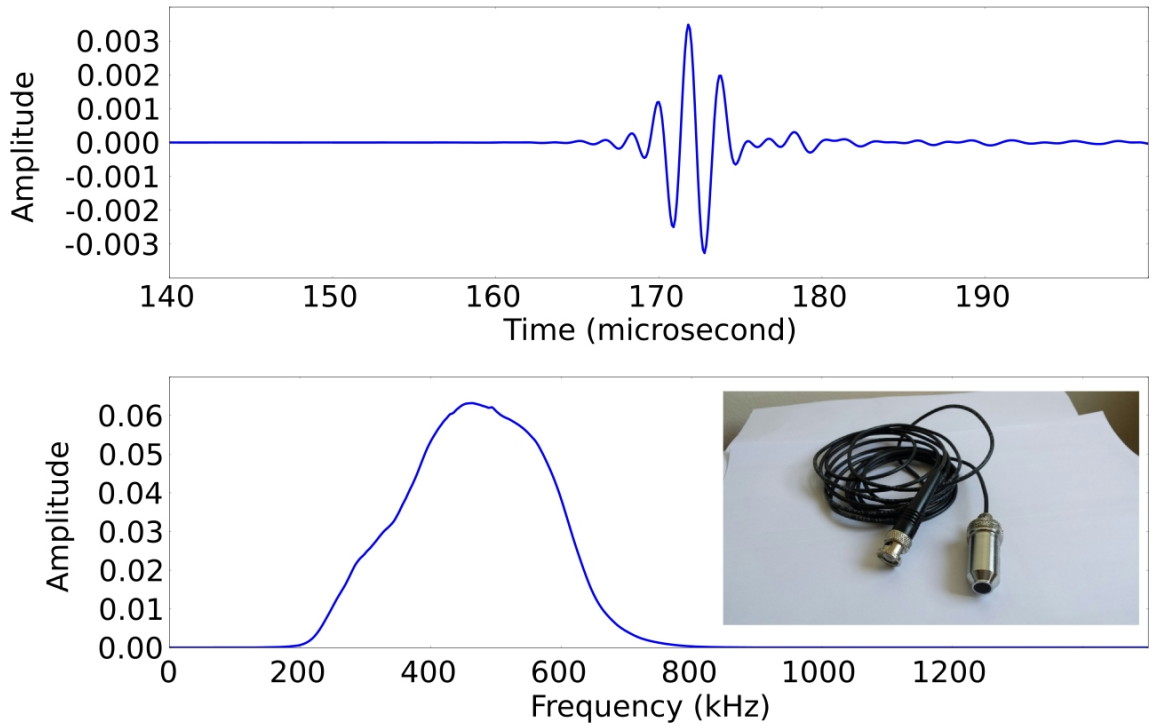

Figure 7. (Top) the signal (filtered between 250-650 kHz) generated by the piezoelectric transducer and recorded by the hydrophone in opposite position, (bottom) the associated amplitude spectrum.

Offset measurements were performed by using two transducers: the above-mentioned transducer as the source, and an omnidirectional Teledyne Reson® hydrophone as the receiver. Both transducers were located 150±0.5 mm above the flat part of the model (labeled as (d) in Figure 2), corresponding to 3 km at seismic scale. The source can be tilted with various angles to illuminate different parts of the model or to enhance some particular effects, such as shadow zones. The hydrophone has an active diameter of 4 mm and its sensitivity is constant between 50-800 kHz (Figure 8). The directivity of the hydrophone in both the vertical and the horizontal planes are also shown in Figure 8.

PART 1

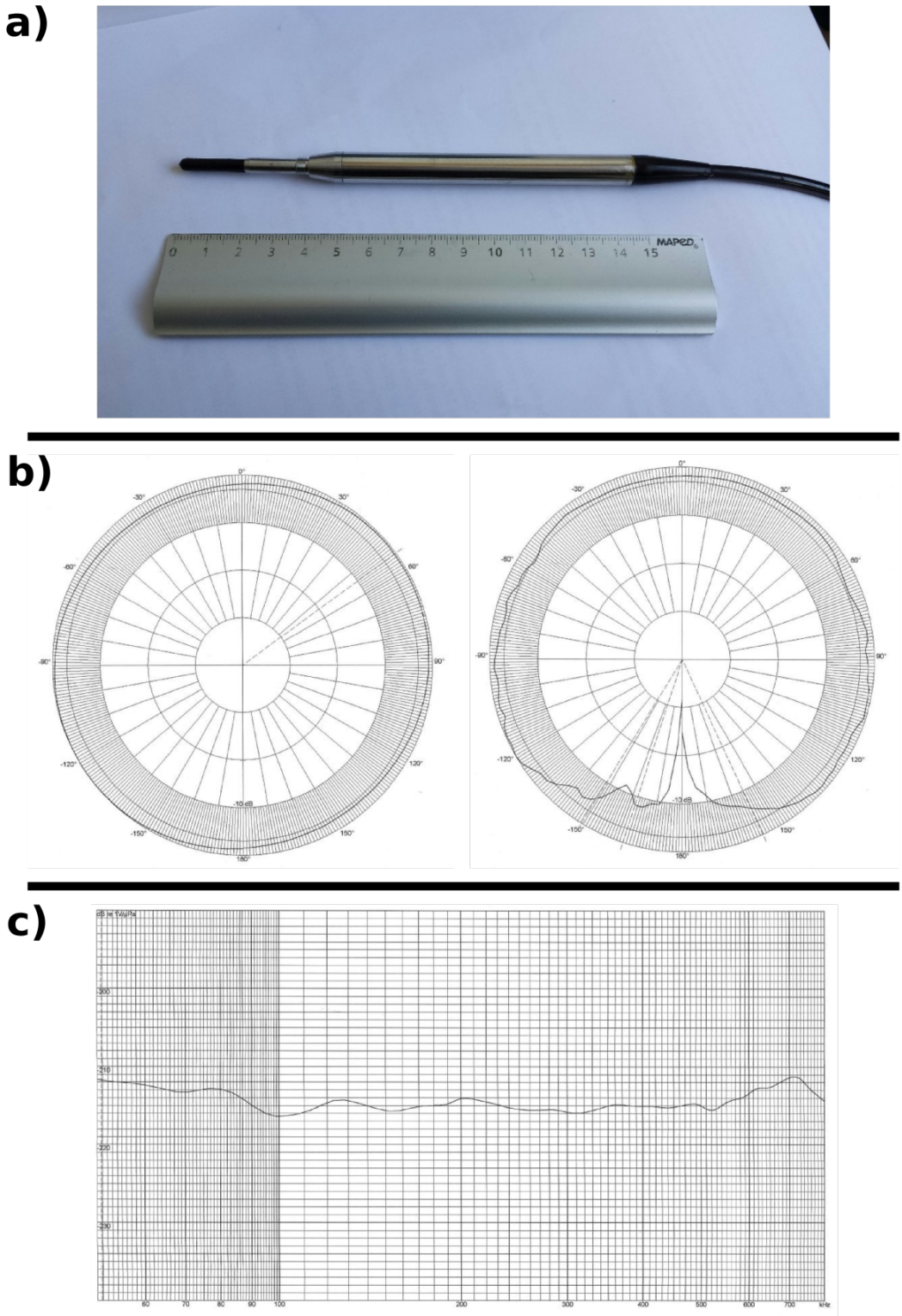

Figure 8. a) The hydrophone used as the receiver in offset configurations, b) its directivity in the vertical (left) and horizontal (right) planes, c) its sensitivity. Figures 8 b) and c) are the courtesy of Teledyne Reson®.

Acquisitions were performed along x-lines (Figure 5) with a sampling distance of 0.5 mm (corresponding to 10 m at seismic scale). The collected data set thus consists of numerous parallel profiles, providing a set of reflection data for a dense grid (with a receiver spacing of 0.5 mm in both x- and y-directions). In order to enhance the signal-to-noise ratio (SNR), a stacking technique was applied before recording the data. The water column above the transducers was always at least 0.6 m and the tilt angle of the source transducer was 39±1° for the offset measurements.

1.3 Illustration of the laboratory data sets

For the sake of brevity, here we focus on a study line, located above the full dome and the truncated pyramid in the x-direction (yellow dashed line in Figure 5). This acquisition line provides complex diffraction effects, (multiple) reflections and arrivals corresponding to curved interfaces. Figure 9 shows the laboratory zero-offset data set for the study line, together with the interpretation of the recorded events. For the sake of clarity, only the main events are interpreted in Figure 9. Events a) and c) represent the arrivals related to the top surfaces of the PVC, corresponding to the pyramid and the dome, and to the flat parts, respectively. Event a) mainly consists of reflections (see positions between 90-115 mm for the pyramid and 95-410 mm for the dome). There are also some diffraction hyperbolas corresponding to the edges of the top surface of the pyramid, for positions less than 90 mm and greater than 115 mm. Moreover, due to the angle of the truncation of the pyramid, there are two smaller hyperbolas in the center of the pyramid, partly overlapping with the reflections from the top flat surface of the object. Similarly to event a), event c) mainly consists of reflections, as well as some diffraction hyperbolas related to the junctions of the pyramid and the dome with the flat part. Events b) and d) correspond to reflections from the bottom of the PVC, below the pyramid and the dome, and below the flat part, respectively. Since Figure 9 is a time section, a classical velocity pull-up effect can be seen in the different arrival times of events b) and d). Indeed, depending on the overburden, reflections from the same horizontal bottom surface of the PVC arrive at different times. Event e) represents reflections from the small truncated dome (Figure 2). This out-of-plane arrival is due to the broad-beam radiation pattern of the source transducer, and it would not be recorded if the source transducer was a conventional one. We note that the diffractions on the right side of the section after 200 μs and for positions 300-420 mm are related to the side of the physical model.

PART 1

Figure 10 shows the laboratory offset data set (i.e. a common shot gather) for the study line together with the interpretation of the main events. Event a) shows the direct arrival from the source, and event b) the reflections from the dome. All the interpretations marked with c) correspond to reflections/diffractions from the pyramid. Event d) illustrates the reflections from the flat part of the PVC. Event e) is related to reflections from the small truncated dome and event f) to reflections from the ramp. Event g) is not related to the model, but to spurious arrivals from the acquisition system.

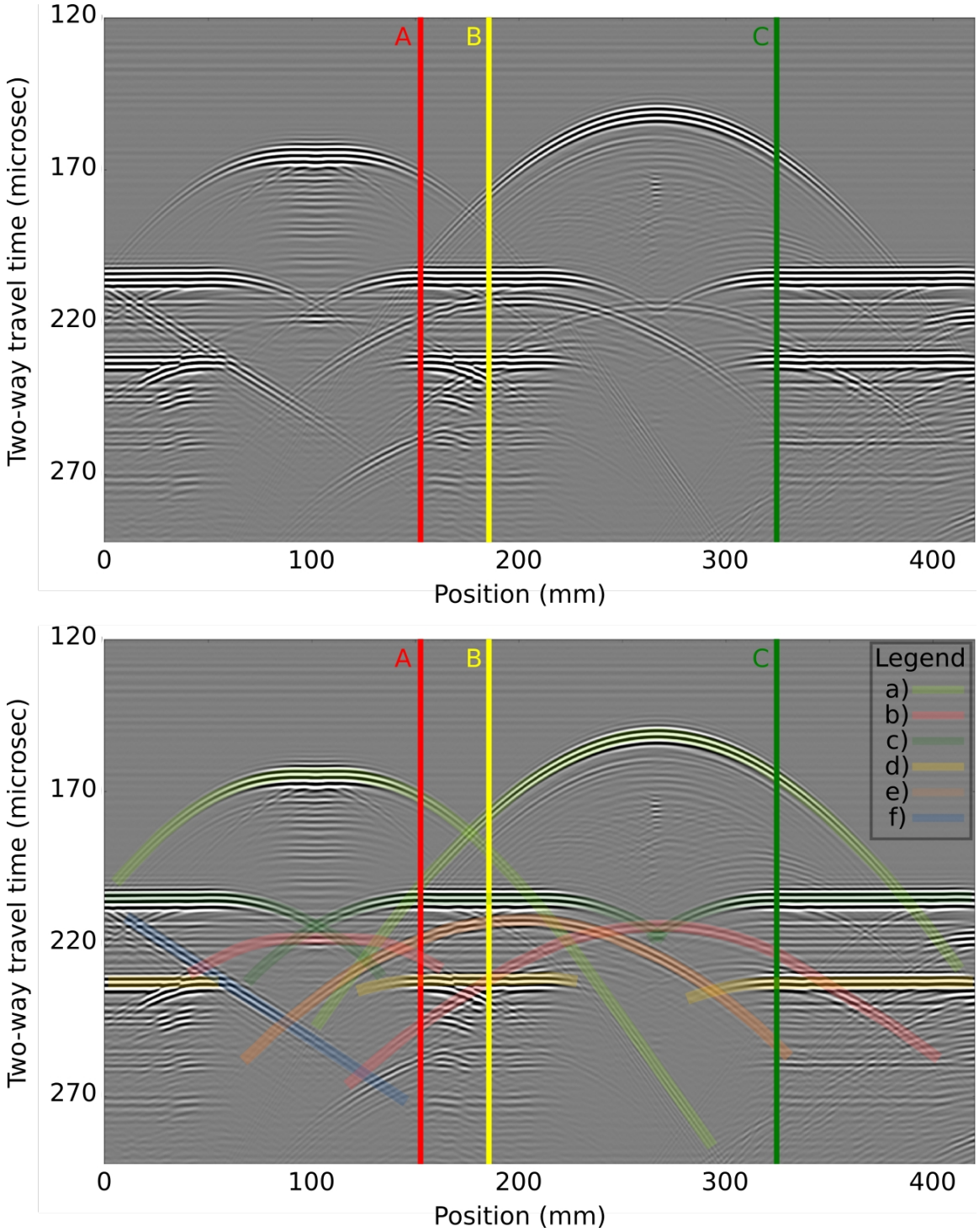

Figure 9. Top: cross-section of the laboratory zero-offset data set along the study line. The data was filtered between 250-650 kHz. Bottom: interpretation. Annotated events: (a) & (b) top & bottom of the pyramid and the dome, (c) & (d) top & bottom of the flat part, (e) truncated dome, (f) ramp. The vertical lines denote the zero-offset traces chosen for comparison with numerical data, presented subsequently in Section 3.1.

PART 1

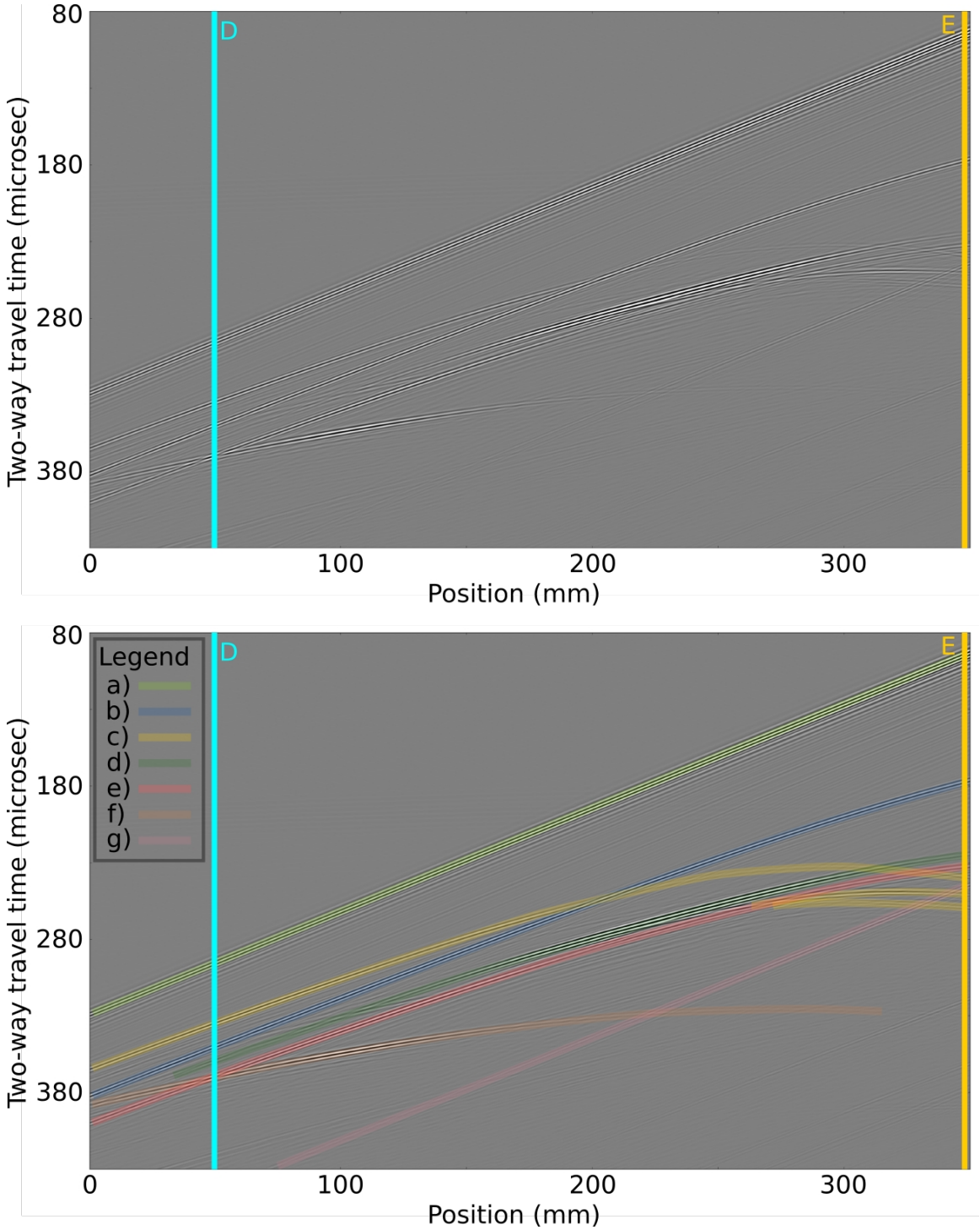

Figure 10. Top: cross-section of the laboratory offset data set (i.e. common shot gather) along the study line. The data was filtered between 250-650 kHz. Bottom: interpretation. Annotated events: (a) direct arrival, (b) dome, (c) pyramid, (d) flat part, (e) truncated dome, (f) ramp, (g) spurious reflection from the acquisition system. The vertical lines denote the offset traces chosen for comparison with numerical data, presented subsequently in Section 3.2.

Chapter 2
Numerical modeling of the laboratory measurements

2.1 Brief overview of some popular numerical methods in seismic modeling

If we considered a block of a homogeneous material with a single source inside, the wave propagation could be easily described both in fluids:

$$\rho \partial_t^2 \boldsymbol{u} = -\nabla p + \boldsymbol{f} \quad , \quad (1)$$

and in solids:

$$\rho \partial_t^2 \boldsymbol{u} = \nabla \cdot \boldsymbol{\sigma} + \boldsymbol{f} \quad , (2)$$

where ρ denotes the mass density, $\boldsymbol{u}=\boldsymbol{u}(\boldsymbol{x},t)$ is the displacement field, $\boldsymbol{x}$ is the spatial coordinates, t is the time, p is the pressure, $\boldsymbol{f}$ is the source term, and σ is the stress tensor, respectively. The derivation of equations 1 and 2 is extensively discussed in the literature (e.g., Aki and Richards, 1980, Dahlen and Tromp, 1998). As noted in the General Introduction, the analytical solution of equations 1 and 2 usually cannot be deduced for realistically complex models, and they must be numerically approximated. By discretizing the continuous derivatives in the governing equations, the numerical algorithms are capable to approximate the wavefield. The accuracy of this approximation depends on the applied method and the parameters of the numerical calculations. Several numerical methods have been developed in the last few decades, which all have advantages and drawbacks, and the selection of the suitable method depends on the application. For instance, what accuracy is needed? What computational cost is affordable? How quickly are the results needed? How difficult/time-consuming is the numerical implementation of the model?

For instance, ray tracing methods are used from the early days of seismic tomography. These algorithms determine the travel path of the seismic rays for a given model and a given source-receiver pair, based on Snell's law (e.g., Julian and Gubbins, 1977, Červený, 1987, Virieux and Farra, 1991, Červený, 2001). Rawlinson et al. (2008) provide a short summary of the different ray tracing methods, which are accurate, but

may not be robust enough, and may encounter instabilities even in slightly heterogeneous models. Due to these drawbacks, grid-based schemes, which calculate the wavefield at each grid point of the model became popular with time. While the different methods are based on very different approaches to discretize the model in time and space, their mathematical formulation can be synthetized. Following the spatio-temporal discretization of the governing equations, we need to solve large algebraic systems and ordinary differential equations in time. As recalled by, for example, Fichtner (2010), formally the discretized algebro-differential equations can be written in the following form:

$$\boldsymbol{M}\cdot\ddot{\bar{\boldsymbol{u}}}(t)+\boldsymbol{K}\cdot\bar{\boldsymbol{u}}(t)=\bar{\boldsymbol{f}}(t) \quad , \quad (3)$$

where **M** is called the mass matrix, **K** is the stiffness matrix, and $\bar{\boldsymbol{u}}(t)$ and $\bar{\boldsymbol{f}}(t)$ are the displacement field and the source term at time t, respectively. The double dot over $\bar{\boldsymbol{u}}(t)$ denotes the second time derivative. In this form, $\bar{\boldsymbol{u}}(t)$ and $\bar{\boldsymbol{f}}(t)$ are vectors, containing, for instance, the discrete values at the grid points (finite-difference approach) or the coefficients describing these quantities (finite-element approach). The mass and stiffness matrices are usually sparse and their structures strongly depend on the formulation of the wave equation and the applied numerical method. Depending on the requirements of some numerical algorithms, equations 1 and 2 may be reformulated as a function of different quantities. For instance equation 1 may be reformulated as a function of only the pressure, only the particle velocity or only the displacement potential to describe the wave propagation in fluids. In solid materials, the common formulations are the displacement-stress, the displacement, and the velocity-stress formulations.

These time-dependent ordinary differential equations can be solved either in the time domain or in the frequency domain. Time-domain simulations are based on the replacement of the time derivatives by finite-difference approximations. There exist various time-stepping schemes, for instance, the leapfrog method, the Newmark scheme, or the more expensive predictor-corrector methods (e.g., Newmark, 1959, Chaljub et al., 2007, Fichtner, 2010). Frequency-domain simulations are based on the Fourier-transformed algebro-differential equations. These solvers provide an accurate solution at a low computational cost if the solution is searched for in 2D, or for only a few given frequencies in 3D. Because of the high memory requirements, especially in the case of wide-band 3D simulations, frequency-domain solvers are outperformed by time-domain iterative solvers.

As we have seen above, most of the time-domain methods use the finite-difference approach for the time-discretization. The main difference between the numerous methods, therefore, lies in their different approaches to the spatial discretization. A very popular approach to the spatial discretization as well is the finite-difference method (FDM). The basic method uses evenly distributed grid points across the model domain and replaces the continuous derivatives with a finite-difference approximation, evaluated only at the grid points. For more details about the basic concept, see for example Alterman and Karal (1968), Boore (1972), Kelly et al. (1976), and Virieux (1986). In 3D the use of a staggered grid helps to significantly reduce the numerical dispersion, although this grid layout presents some difficulties, for instance in the implementation of anisotropy or the free-surface boundary condition (e.g., Madariaga, 1976, Virieux, 1984, 1986, Holberg, 1987, Mittet, 2002). The FDM is usually considered to have a low computational cost (mainly on CPUs), especially for models with relatively simple and slowly-varying geometries. Any arbitrary model geometry can be easily implemented in the FDM (with the exception of the free surface), however curved and tilted interfaces require a fine grid spacing in order to avoid artifacts due to the staircase representation of the geometry, which may inflate the computational cost.

The pseudospectral method (PM) uses the same spatial discretization as the FDM. The spatial derivatives are then calculated in the wavenumber domain, following the Fourier-transformation of the wavefield. In the wavenumber domain, the spatial derivation becomes a simple multiplication by i$\mathbf{k}$, where $\boldsymbol{k}$ is the wavenumber (e.g., Kosloff and Baysal, 1982, Carcione, 2010). Chebyshev transformation can also be used in the vertical direction, instead of the Fourier transformation, to better handle the boundary conditions (e.g., Kosloff et al., 1990, Tessmer and Kosloff, 1994). In general, the PM has much less numerical dispersion than the FDM, but it has also a huge memory requirement, necessary for the Fourier/Chebyshev transformations. This makes it difficult to parallelize the pseudo-spectral algorithms with currently available computing facilities.

The finite-element method (FEM) is based on the weak form of the wave equation. The main advantage of the weak form is that it implicitly satisfies the free-surface condition, not like in the case of the FDM. The computational domain is decomposed into disjoint elements, and the Galerkin method is used to approximate the exact solution of the wavefield by the superposition of several basis functions, which usually depend only on the space. The approximation is based on low-order polynomials, and the continuity of the wavefield among the elements must be

explicitly imposed. Therefore the FEM mathematically reduces to the calculation of the polynomial coefficients for each element (e.g., Lysmer and Drake, 1972, Toshinawa and Ohmachi, 1992, Bao et al., 1998). The main advantage of the FEM is its ability to account for the real geometry by explicitly honoring each discontinuity, as well as its suitability for parallel computing. However, the classical FEM algorithms suffer from a significant numerical dispersion due to the low-order polynomial approximation, as well as from the non-diagonal mass matrix in equation 3, making its inversion expensive. Because of these disadvantages, hybrid methods have been proposed, which couple the classic FEM algorithms with other methods. This exploits the advantage of the FEM of explicitly honoring the discontinuities, while the inner parts of the model are simulated with other numerical methods (e.g., Moczo et al. 1997, 2007).

Today's numerical simulations are often based on multi-core processors and supercomputers, using a massively parallel computing approach. *Multi-core processor* refers to a computing unit with multiple processing units, often called *cores*. These *cores* are placed on the same integrated circuit die, and can independently read and execute program instructions. This increases the overall computing capacity if the programs are suitable for parallel computing. A massively parallel computer has numerous processors working together to solve a large problem. Separate parts of the problem/data are fed to different processors, which all do the same mathematical operation, and at the end, the results are recombined. As of 2018, supercomputers of petaflop[3] capacities are accessible for the scientific community. Thanks to the still ongoing evolution of the computational resources, more and more complex problems can be simulated for, or earlier simulations may be re-performed at higher resolution, using fewer approximations. Although this is out of the scope of this thesis, some numerical algorithms may be more suitable for parallel calculations than others, at least using the currently available technology. As the technology evolves in the future, other numerical algorithms may become more affordable with time, for example, algorithms with a high memory requirement.

3 petaflop: 10^{15} floating point operations per second

2.2 The spectral-element method

In this work, we use primarily the spectral-element method (SEM) for the numerical simulations. This choice was motivated by the facts that the SEM:

- is a full-wave method with high accuracy,
- can use a non-structured mesh to honor irregular discontinuities and topographies, therefore, the uncertainty of the numerical implementation of the model geometry can be mostly ruled out in the case of any future misfit between the measurements and the simulated data,
- can use different element sizes in the mesh, hence, it is suitable for models with varying material properties,
- can accurately account for the fluid-solid coupling and surface waves without requiring a high number of grid points, such as in the case of the FDM.

The SEM can be considered as a special type of the FEM, which uses higher order basis functions than the classic FEM. This way the SEM combines the accuracy of the pseudo-spectral method with the flexibility of the FEM. The SEM was first developed in fluid dynamics by Patera (1984). The method is also widely applied in seismology (e.g., Seriani et al., 1995, Faccioli et al., 1997, Komatitsch and Vilotte, 1998, Seriani, 1998, Komatitsch et al., 2004, Fichtner et al., 2009, Komatitsch and Tromp, 2002, Chaljub et al., 2003, 2007, Peter et al., 2011), and in ocean acoustics (e.g., Cristini and Komatitsch, 2012, Bottero et al., 2016).

Here we focus only on some of the most important features of the method using solid materials for demonstration, and we refer the reader to Komatitsch and Vilotte (1998), Fichtner (2010), or Peter et al. (2011) for more details.

2.2.1 Weak form of the wave equation

Similar to the classic FEM, the SEM is also based on the weak form of the wave equation. Considering solid materials, equation 2 describes the propagation of seismic waves. Under the assumption of small perturbations, the stress tensor $\boldsymbol{\sigma}$ in equation 2 is linearly related to the displacement field by the constitutive relationship (Hooke's law):

$$\boldsymbol{\sigma} = \boldsymbol{C} : \nabla \boldsymbol{u} \quad , (4)$$

where $\boldsymbol{C}$ denotes the stiffness tensor, describing the elastic properties of the material.

Equations 2 and 4 together provide the displacement-stress formulation of the wave equation. The weak form of the wave equation can be obtained by multiplying equation 2 with a time-independent arbitrary test function $\boldsymbol{w}$, and then integrating by parts over the total volume $\boldsymbol{\Omega}$ and surface $\boldsymbol{\delta\Omega}$ of the model:

$$\int \rho \boldsymbol{w} \cdot \partial_t^2 \boldsymbol{u} \, d^3x = \int \hat{\boldsymbol{n}} \cdot \boldsymbol{\sigma} \cdot \boldsymbol{w} \, d^2x - \int \nabla \boldsymbol{w} : \boldsymbol{\sigma} \, d^3x + \boldsymbol{D} : \nabla \boldsymbol{w}(\boldsymbol{x}_s) S(t) \quad , (5)$$

where $\hat{\boldsymbol{n}}$ denotes the unit outward normal vector on $\boldsymbol{\delta\Omega}$, and **D** is the moment tensor of a point source, which can be described as the source term $\boldsymbol{f(t)}$ in equation 2 as:

$$\boldsymbol{f}(t) = -\boldsymbol{D} \cdot \nabla \delta(\boldsymbol{x} - \boldsymbol{x}_s) S(t) \quad , (6)$$

where $\boldsymbol{x}_s$ denotes the source position, δ is the Dirac distribution, and $S(t)$ is the source wavelet. Equation 5 can be reformulated in the same form as equation 3, i.e. using a mass matrix and a stiffness matrix to describe the wave propagation.

2.2.2 Galerkin approach

Identical to the classic FEM, the model domain $\boldsymbol{\Omega}$ is divided into disjoint subdomains $\boldsymbol{\Omega}_e$ (called elements), and the Galerkin method is used to approximate the wavefield in each element with the help of local basis functions. These basis functions depend only on the material properties of the given element, therefore the continuity of the displacement field has to be explicitly imposed on the element boundaries.

2.2.3 Basis functions and integral quadrature

The uniqueness of the SEM among the other finite-element algorithms lies in the choice of the basis functions, and the quadrature to compute the integrals for the mass and stiffness matrices in equation 3. Although there are other options (e.g. using Chebyshev polynomials (Patera, 1984)), here we focus on the most common choice when N+1 Lagrange polynomials of degree N are used to approximate the wavefield (e.g. Davis and Rabinowitz, 1984); and the Gauss-Lobatto-Legendre (GLL) quadrature to compute the integrals. This combination leads to a perfectly diagonal mass matrix in equation 3, which then enables the use of an explicit time scheme that can be efficiently parallelized (Komatitsch et al., 2003, Carrington et al., 2008, Vos et al., 2010). The choice of Lagrange polynomials to approximate the wavefield requires that only rectangular elements are used in 2D and only hexahedral elements in 3D.

2.2.4 Accuracy and stability

Using N+1 Lagrange polynomials of degree N in combination with the GLL quadrature provides an exact integration of polynomial functions of degree 2N-1 or lower at the collocation points. That is, the numerical error is negligible at the GLL points, but not exact at other points, and the error of the approximation depends on the element size, the time step, and the order of the polynomial basis functions too. Because the numerical dispersion is cumulative, this inexact approximation can be especially important in the case of wave propagation for long ray paths. To overcome the numerical dispersion, one should use basis functions of the highest possible order, but that would inflate the computational cost as well. Therefore the order of the basis functions is usually between 4 and 8. The element size usually depends on the wavelength, and the order of the polynomials of the shape functions (see section 2.2.5). The CFL condition defines a stability criterion, which serves as an upper limit to ensure the stability of the simulations (Courant et al., 1928). The CFL condition varies with the method, as it depends on the time-stepping scheme and on the order of the basis functions as well. The CFL number is proportional to the wavelength and inverse-proportional to the time step:

$$CFL\,number \sim \frac{wavelength}{timestep} \quad . (7)$$

Satisfying the CFL condition ensures only the stability of the simulation, but not its accuracy. To increase the accuracy of the approximation one could choose a small element size and time step, but this would also increase the computational cost. Therefore a trade-off must be found, where stability and accuracy are ensured at the lowest possible computational cost.

2.2.5 Remapping onto a reference element

Using the currently available computational infrastructure, it is highly advantageous to perform the same mathematical operation on many elements at the same time. Therefore each element is mapped onto a reference element (e.g. in the case of a hexahedral element onto a cube). The extent of this reference element is $[-1, 1]^n$, where *n* denotes the number of spatial dimensions. Because of the usually complex shaped elements in a non-structured mesh, the mapping is also based on a polynomial approximation. *Shape functions* are used to describe the shape of a given element, and the wavefield is evaluated on so-called *anchor nodes*. The shape functions are usually 1^{st} or 2^{nd} order Lagrange polynomials, depending on the complexity of the element shapes. Figure 11 illustrates the positions of the anchor nodes in the case of 1^{st} and 2^{nd}

order hexahedral elements. In the 1st order case the 8 corners are the anchor nodes, while in the 2nd order case there are additional anchors in the centers of the edges, surfaces and the volume as well, altogether 27 nodes. One can clearly see the advantage of the 2nd order case, as it can account for curved surfaces and edges as well. It can be especially advantageous if bigger and/or significantly deformed elements are to be used in a mesh (Appendix B). Thanks to the mapping, the wave equation can be easily solved for each element without the need to know the material properties of the full domain $\boldsymbol{\Omega}$. It also translates into less memory requirement during the calculations.

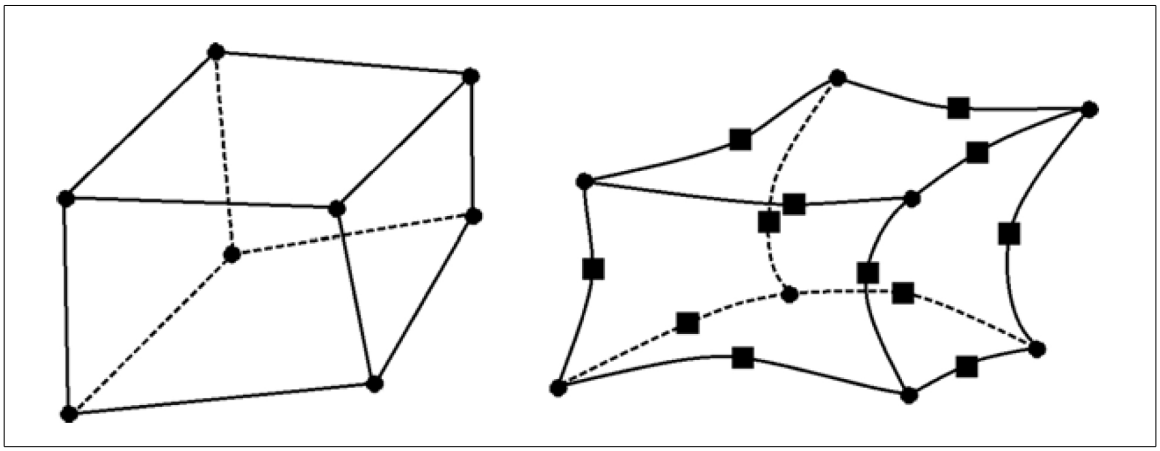

Figure 11. Distribution of the anchor nodes to evaluate the wavefield in a given element for the remapping onto the reference cube. Left: 1st order elements with eight anchor nodes, using linear shape functions. Right: 2nd order elements with additional anchor nodes, using shape functions of degree 2. Adding anchor nodes to the center of the volume and of each face, the total number of nodes becomes 27 (Figure 4.4 in Fichtner, 2010).

2.2.6 Point source implementation

As noted above, the SEM has an exact integration only at the GLL points. Therefore, any source should preferably inject energy into the model in a smooth way (both in time and space) to avoid numerical instabilities. However, in seismic exploration/seismology, the source is usually point localized (equation 6), which is a perfectly non-smooth distribution of the source energy. To overcome this, we use once again Lagrange integrals to approximate the delta function in space (Faccioli et al., 1997). Because this solution inevitably yields a low-pass-filtered version of the real delta function, the source implementation is not perfect in the near-field. Faccioli (1997) and Nissen-Meyer et al. (2007) show that this issue remains limited to the element containing the source.

2.2.7 Time stepping

As noted above, most of the time-domain numerical methods use an iterative scheme, based on the finite-difference approach to advance the wavefield in time in discrete time steps *Δt*. As seen in Section 2.2.3, a perfectly diagonal mass matrix in equation 3 can be ensured by a smart choice of the basis functions and the integral quadrature. Then an explicit time scheme can be used to advance in time the algebro-differential equations. In this thesis we use the second-order explicit Newmark scheme for time stepping (Newmark, 1959, Hughes, 1987), defined as:

$$\boldsymbol{u}(t+\Delta t)=\boldsymbol{u}(t)+\Delta t\,\dot{\boldsymbol{u}}(t)+\frac{1}{2}\Delta t^2\ddot{\boldsymbol{u}}(t) \quad , (8)$$

and

$$\dot{\boldsymbol{u}}(t+\Delta t)=\dot{\boldsymbol{u}}(t)+\Delta t\,\ddot{\boldsymbol{u}}(t)+\frac{1}{2}\Delta t[\ddot{\boldsymbol{u}}(t+\Delta t)-\ddot{\boldsymbol{u}}(t)] \quad , (9)$$

The following iterative scheme is used to advance equation 3 in time:

1) compute $\ddot{\boldsymbol{u}}(t)$ for $t=t_0$, using equation 3, where we omit the upper bar signs for the sake of clarity:

$$\ddot{\boldsymbol{u}}(t)=\boldsymbol{M}^{-1}[\boldsymbol{f}(t)-\boldsymbol{K}\boldsymbol{u}(t)] \quad , (10)$$

2) compute $\ddot{\boldsymbol{u}}(t+\Delta t)$, using $\boldsymbol{f}(t+\Delta t)$, $\boldsymbol{u}(t)$, $\dot{\boldsymbol{u}}(t)$, and $\ddot{\boldsymbol{u}}(t)$:

$$\ddot{\boldsymbol{u}}(t+\Delta t)=I^{-1}\times[-K\boldsymbol{u}(t)-\Delta t\,K\dot{\boldsymbol{u}}(t)-\frac{1}{2}\Delta t^2K]\ddot{\boldsymbol{u}}(t)+f(t+\Delta t) \quad , (11)$$

where I is the identity matrix,

3) compute $\boldsymbol{u}(t+\Delta t)$ from $\boldsymbol{u}(t)$, $\dot{\boldsymbol{u}}(t)$, $\ddot{\boldsymbol{u}}(t)$ and $\ddot{\boldsymbol{u}}(t+\Delta t)$, using equation 8,

4) compute $\dot{\boldsymbol{u}}(t+\Delta t)$ from $\dot{\boldsymbol{u}}(t)$, $\ddot{\boldsymbol{u}}(t)$, and $\ddot{\boldsymbol{u}}(t+\Delta t)$, using equation 9,

5) replace t by $t+\Delta t$ and return to 2).

2.2.8 Boundary conditions

In order to save computational cost, we may need to limit the computational domain and introduce artificial boundaries. To avoid spurious reflections from these boundaries, a careful treatment of the wavefield is necessary. Namely, the incident waves must be efficiently absorbed, and no energy should be reflected backward. *Absorbing boundary condition* methods are based on the paraxial approximations of the wave equation (Engquist and Majda, 1977, Clayton and Engquist, 1977, Stacey, 1988, Quarteroni et al., 1998). Although these methods have a low computational cost and are efficient to absorb seismic waves at close to normal incidence, waves at grazing incident angles are reflected back (Keys, 1985, Higdon, 1991). Moreover, the method can be unstable for elastic materials if the V_p/V_s ratio is bigger than about 2.17 (Emerman and Stephen, 1983, Mahrer, 1986); or if the simulations are for a long period of time (Mahrer, 1990).

We prefer using the approach of perfectly matched layers (PML), introduced by Berenger (1994). Contrary to the absorbing boundary techniques, PML methods use thin layers around the external surfaces (Collino and Tsogka, 2001, Zheng and Huang, 2002, Komatitsch and Tromp, 2003, Festa and Vilotte, 2005, Festa et al., 2005, Kristek et al., 2009, Xie et al., 2016). In these layers, the wave equation is modified such that, the amplitude of the incident waves decays rapidly. The term 'perfect' refers to the fact that, the wave equations in the normal computational domain and in the PML zone are coupled in a way that no reflections are produced on the artificial boundaries. Because the SEM uses the weak form of the wave equation, the modified equations in the PML region have singularities that need to be explicitly removed (Xie et al., 2016).

2.3 Adapting the Specfem software package to our framework

We used Specfem (Komatitsch and Vilotte, 1998), an open-source software package for the spectral-element simulations of this thesis. The software package has 2D, 2.5D (axisymmetric), 3D Cartesian and 3D Globe versions. Specfem was initially developed for the simulation of earthquakes, but it is also used for other applications in exploration geophysics and global seismology (e.g., Komatitsch and Vilotte, 1998, Seriani, 1998, Komatisch and Tromp, 2002, Fichtner et al., 2009, Peter et al., 2011);

ocean acoustics (e.g., Cristini and Komatitsch, 2012, Bottero et al., 2016); and non-destructive testing (e.g. Nagaso et al., 2016). Efficient parallel computing is available in the package due to the use of message passing interfaces (MPI). A typical workflow of the software package is shown in Figure 12. The first step is generating a hexahedral mesh, either by importing it from an external tool or using the internal mesher. The second step is used only in the case of parallel computations when the mesh is decomposed into partitions, which will be distributed to the different processors during the actual simulations. The third step is the generation of databases to be used during the simulations. The last step is the simulation of the wave propagation, i.e. running the actual solver.

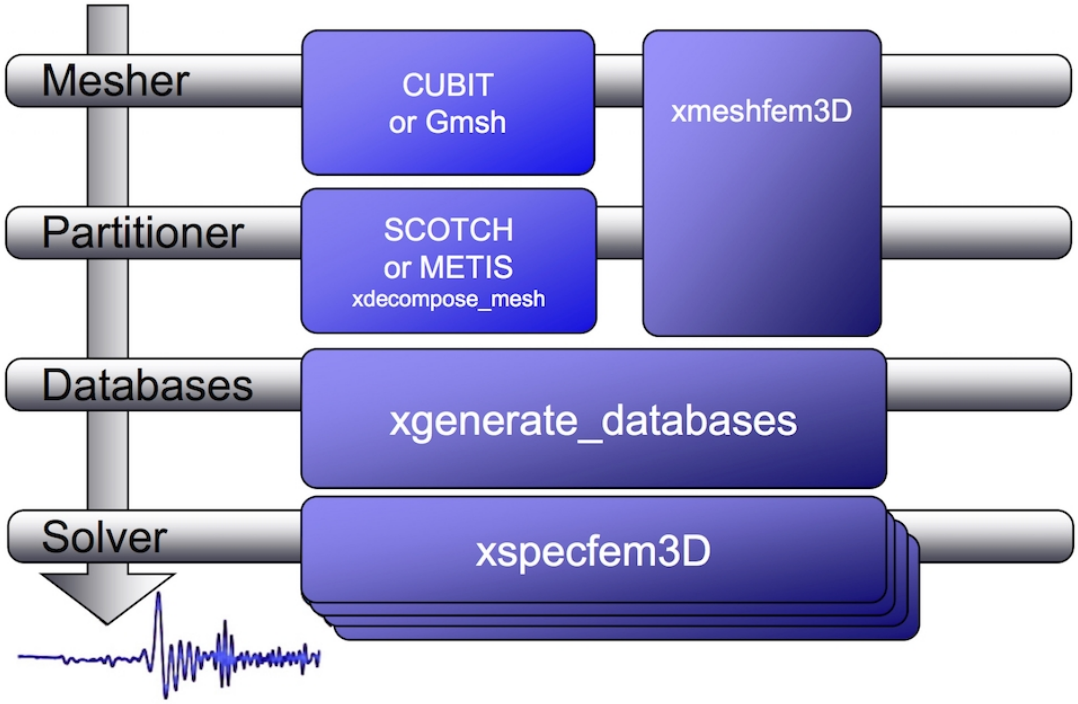

Figure 12. The typical workflow of simulating the propagation of seismic waves with the Specfem3D Cartesian software package. Courtesy of Computational Infrastructure for Geodynamics.

2.3.1 Non-structural meshing of the Marseille-Benchie model

Creating a non-structured hexahedral mesh for a complex geometry is a challenging and lengthy task (Shepherd and Johnson, 2008, Staten et al., 2010). We used Cubit/Trelis (Blacker, 1994) as a software to mesh the Marseille-Benchie model in

3D. In the case of a non-structured mesh, we need to keep in mind the future computational cost and the accuracy by considering three points. First, the element size must be small enough to accurately model the highest frequencies of interest. Second, the size of the different elements in one material should be as equal as possible (depending on the geometry) to avoid too small elements. This is important because smaller elements require smaller time steps according to the CFL-condition (equation 7), i.e. higher computational cost and more memory. Finally, one needs to avoid creating too distorted/elongated elements, which could result in a mesh of poor quality, making the simulation unstable. Because the model has a complex overall geometry, fully automatic hexahedral meshing algorithms could not be used. Our solution was to cut the domain into several subdomains, which were easier to handle for the meshing software (Figure 13). The challenge of the task was to find the order in which the individual subdomains had to be meshed, such that the entire computational domain could be meshed at the end. Due to these difficulties, and also to reduce the computational cost, we considered only a part of the full model for the numerical simulations (Figure 13). As a result, the truncated dome was excluded from the simulations because this object proved to be too complex to be meshed, mainly due to its small dimensions combined with sharp edges and narrow corners. With our decomposition strategy, we first obtained approximately 15.6 million elements, including the water column above the PVC. Figure 14 shows the distribution of the element size for the part of the Marseille-Benchie model under consideration with the applied decomposition and meshing strategies. The maximum edge length is about four times bigger than the smallest one, being approximately 1.6 and 0.4 mm, respectively. It is important to note that the accuracy of the spectral-element simulations is not directly constrained by the element size, but rather by the number of GLL points per wavelength. The initial meshing strategy was designed for fourth-order polynomial basis functions, requiring five GLL points per wavelength, which is approximately five GLL points per edge (Mulder, 1999). Considering the minimum velocity of the model – namely, 1050 m/s for the S-waves in PVC – and the maximum target frequency (650 kHz), the goal was to have all the edge lengths below 1.6 mm. We present an optimized meshing strategy in Appendix B, which allowed us to reduce the number of elements to about 1.4 million and the computational cost by a factor of four to six.

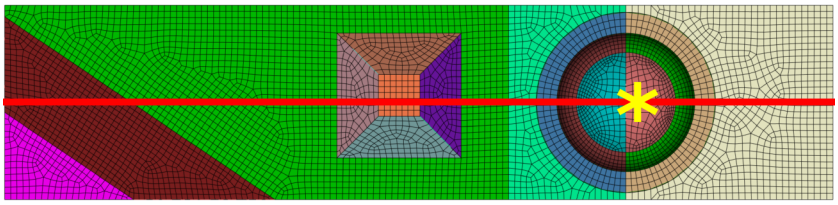

Figure 13. Part of the model used for the numerical simulations with a coarse mesh. The red line denotes the position of the study line discussed in Part 1. The yellow asterisk shows the source position for the offset study line. The different colors show the subdomains necessary for the non-structured meshing.

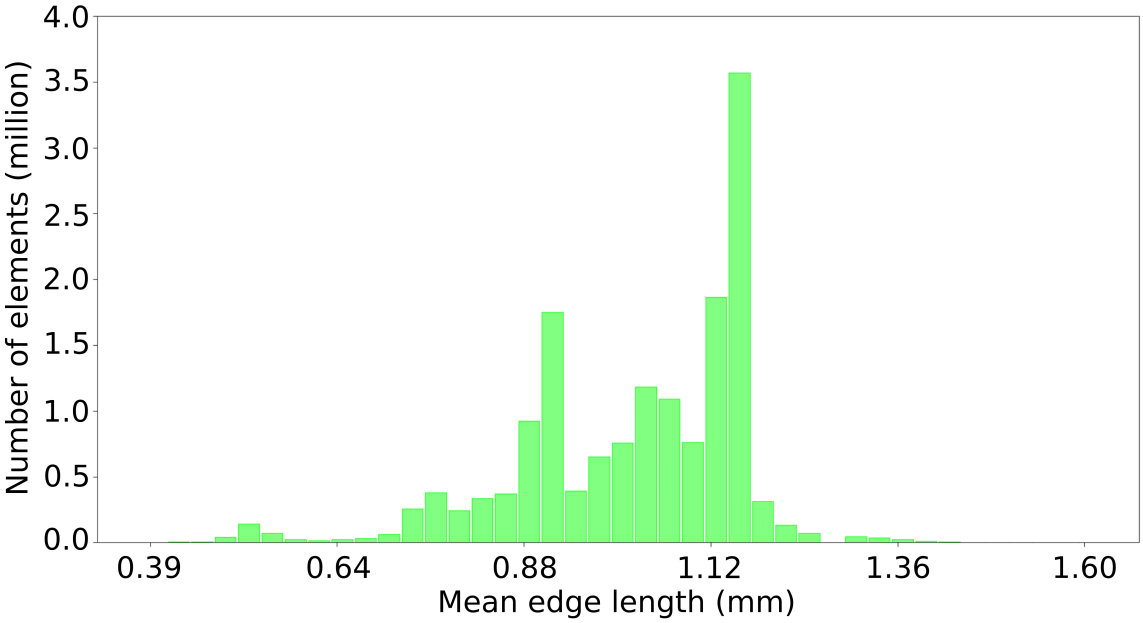

Figure 14. Distribution of the element size of the mesh for the part shown in Figure 13.

2.3.2 Viscoelasticity in the simulations

Because the Marseille-Benchie model is made of strongly attenuating PVC (Table 1), viscoelasticity had to be incorporated in the simulations. In reality, the initial energy of the seismic waves decays with time, due to heat dissipation, grain boundary relaxation, thermal diffusion, etc. In order to account for this energy decay, equation 4 has to be modified such that the stress is determined by the entire strain history:

$$\boldsymbol{\sigma}(t) = \int \partial_t \boldsymbol{C}(t-t') : \nabla \boldsymbol{u}(t')\, dt' \quad . (12)$$

Even in the case of viscoelastic rheology in seismic exploration, we can still suppose a linear relationship between the stress and the strain. The overall effect of all the

energy dissipating mechanisms can be modeled using the technique of Liu et al. (1976), which approximates the absorption with a set of standard linear solids. This standard approach usually assumes that the quality factor Q does not depend on the frequency, which is the usual case in both seismic exploration and global seismology. This assumption is also confirmed for the Marseille-Benchie model by our laboratory measurements, which show very similar Q factors for the PVC when measured between 250-650 kHz (Appendix A). In practice, the approximation of the viscoelasticity with the Zener model requires fitting Q in the frequency range of interest by using a set of relaxation mechanisms. The rule of thumb is to use two-three relaxation mechanisms per order of magnitude in the frequency range, to achieve a good fit of the constant Q model. In our work, we use three standard linear solids. The relaxation times are represented by points in the frequency range and their associated weights. A linear approach can be used by presetting the points at given frequencies in the frequency range of interest and then optimizing the fit only for the weights (Emmerich and Korn, 1987). However, this approach does not ensure the positivity of the weights and thus the decay of the total energy over the time may not be ensured.

An alternative approach is introduced by Blanc et al. (2016) to ensure that the weights are always positive and their nonlinear optimization is also more accurate in terms of fitting the constant Q approximation in the frequency range of interest. The nonlinearity means that both the points and the weights are optimized to obtain a better fit of Q for the frequency range of interest. We use this non-linear approach for the simulations presented in this thesis.

2.3.3 Numerical implementation of the transducer characteristics

One of the most important tasks was to accurately implement the real characteristics of the transducers in the numerical simulations. Because it is omnidirectional and has a frequency-independent sensitivity in the frequency range of interest (250-650 kHz), the Teledyne Reson® hydrophone (used as the receiver for offset measurements) was implemented as a point receiver. However, the Imasonic® source transducer has a unique radiation pattern that cannot be described by the classical analytical formulation of Zemanek (1971), nor by an approximate radiation pattern valid only for the dominant frequency (Tantsereva et al., 2014a). The latter does not provide an optimal solution because other frequencies also contribute to the radiation pattern. Therefore, we propose a new, two-step approach to implement the real transducer characteristics in the numerical simulations, accounting for all frequencies of interest.

The procedure consists of the laboratory characterization of the source followed by an inversion step to obtain a numerically equivalent source. Because point sources are implemented in most of the numerical tools, we built an equivalent disk source of several point sources in order to be able to use the same implementation with various numerical solvers. This approach is based on the theory of wave superposition (Koopmann et al., 1989). The disk is described by three parameters: the thickness, the radius, and the number of point sources distributed on its surface. The different point sources are independent, i.e. they can have any arbitrary (smooth) source signal and are constrained only by the measured data set of the laboratory characterization. The goal of the inversion is to determine the source signal of each point source, such that the resulting overall source signal of the whole equivalent source is the same as the one measured at each angle. At this point, we need to distinguish the procedures to obtain the numerically equivalent source in zero-offset and offset configurations because they require a slightly different approach (Figure 15). We first introduce the procedure for the offset case, and the differences for the zero-offset case are discussed afterward.

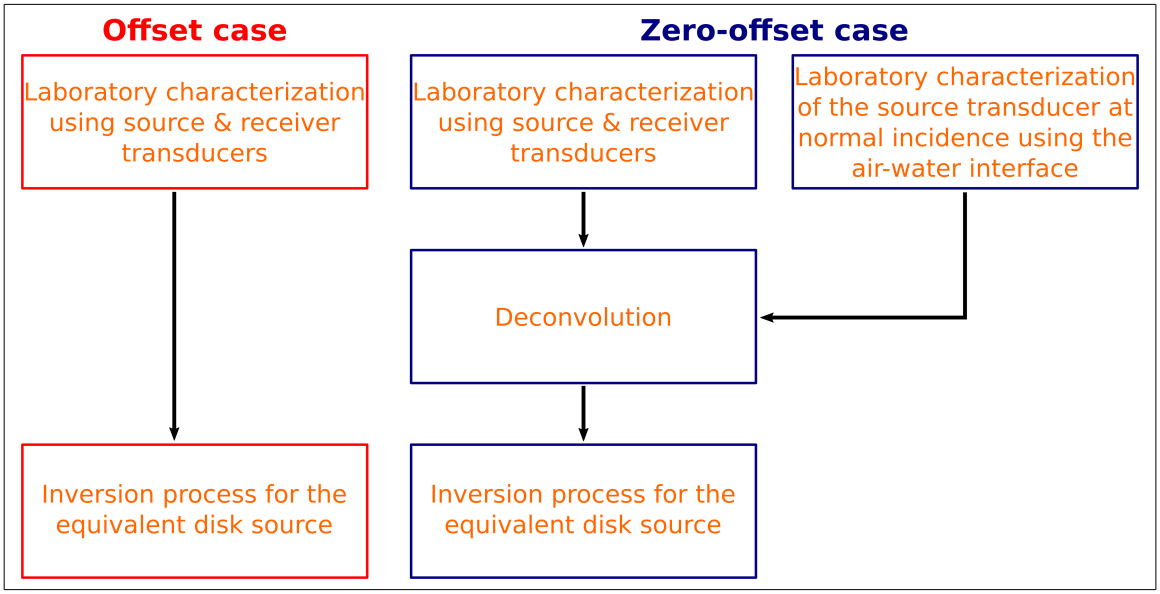

Figure 15. Workflow of the procedures used to implement the numerical equivalent of the real source transducer in offset and zero-offset configurations.

For the offset case, only the laboratory characterization of the source transducer with the receiver is required to obtain a numerically equivalent source. The characterization of the source transducer was performed in a water tank. The source transducer was connected to a pulse generator and kept fixed, and its impulse response was recorded with the hydrophone at every 0.2°, covering an angle range of

200°, at a constant distance of 259 mm (Figure 16). The recorded data set was the input for the subsequent inversion step.

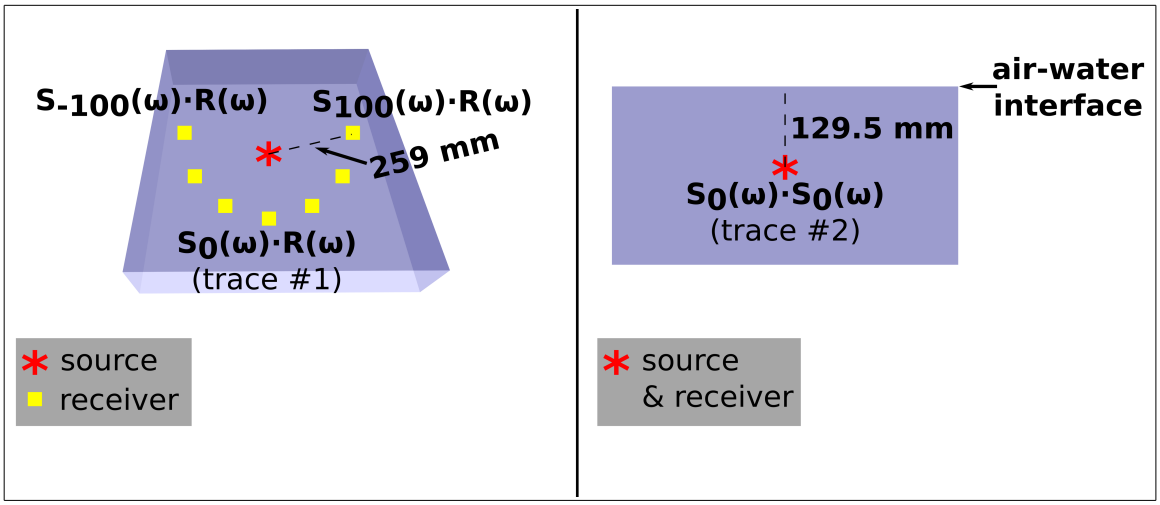

Figure 16. Schematic diagrams of laboratory characterization of the source transducer using the source and receiver transducers (left), and the source transducer illuminating the air-water interface at normal incidence (right).

The initial guess for each point source distributed on the surface of the equivalent disk source was a constant zero pressure, and the cost function was computed using the L2-norm:

$$\Phi^{(k)} = \sum_i \sum_i \left(m_{ii} - c_{ii} \right)^2 \quad , (13)$$

where $\Phi^{(k)}$ denotes the cost function after the k^{th} iteration, and m_{ij} and c_{ij} are the recorded and the calculated impulse responses at the i^{th} time sample and j^{th} hydrophone position, respectively. During the inversion step, some parameters, namely, the radius of the equivalent disk, the number of point sources distributed on the disk, the number of layers in the disk, and the number of iterations, were tested to find the best fit with the measured data. We found that a radius of 3 mm with 253 point sources distributed on only one disk layer gives the best fit between the measured and the inverted radiation patterns (Figure 17). Using more than 10 000 iterations did not result in any significant change in the results. The comparison of simulated traces using the inverted equivalent source with the measured traces shows an angle dependency in the goodness of fit (Figures 17-18). Indeed, the main lobe of the radiation pattern (corresponding to ±30° around the center of the transducer) is accurately recovered. For example, the correlation coefficients between the measured and simulated traces at 0° and 20° are 0.99 and 0.98, respectively (Figure 18).

However, outside of the range of ±30°, the goodness of fit drastically decreases with increasing angle from the center of the transducer (Figure 17). For example, the correlation coefficient between the measured and simulated traces at 60° is 0.64. Therefore, the secondary lobes of the real radiation pattern are less accurately recovered. This can be explained by the fact that the recorded signals corresponding to the secondary lobes have far less energy than those of the main lobe (less than −20 dB at high angles). Hence, they can be overshadowed by the noise recorded in the laboratory data.

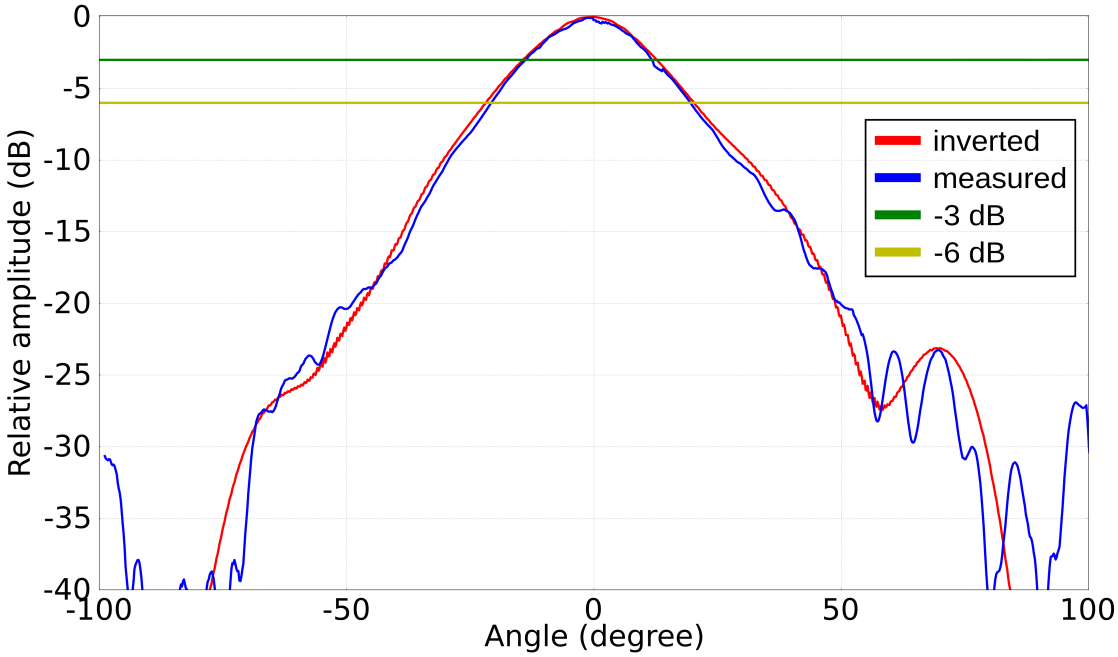

Figure 17. Comparison of the measured (blue) and inverted (red) radiation patterns of the transducer in the offset configuration. The amplitude is maximal opposite to the transducer (0°).

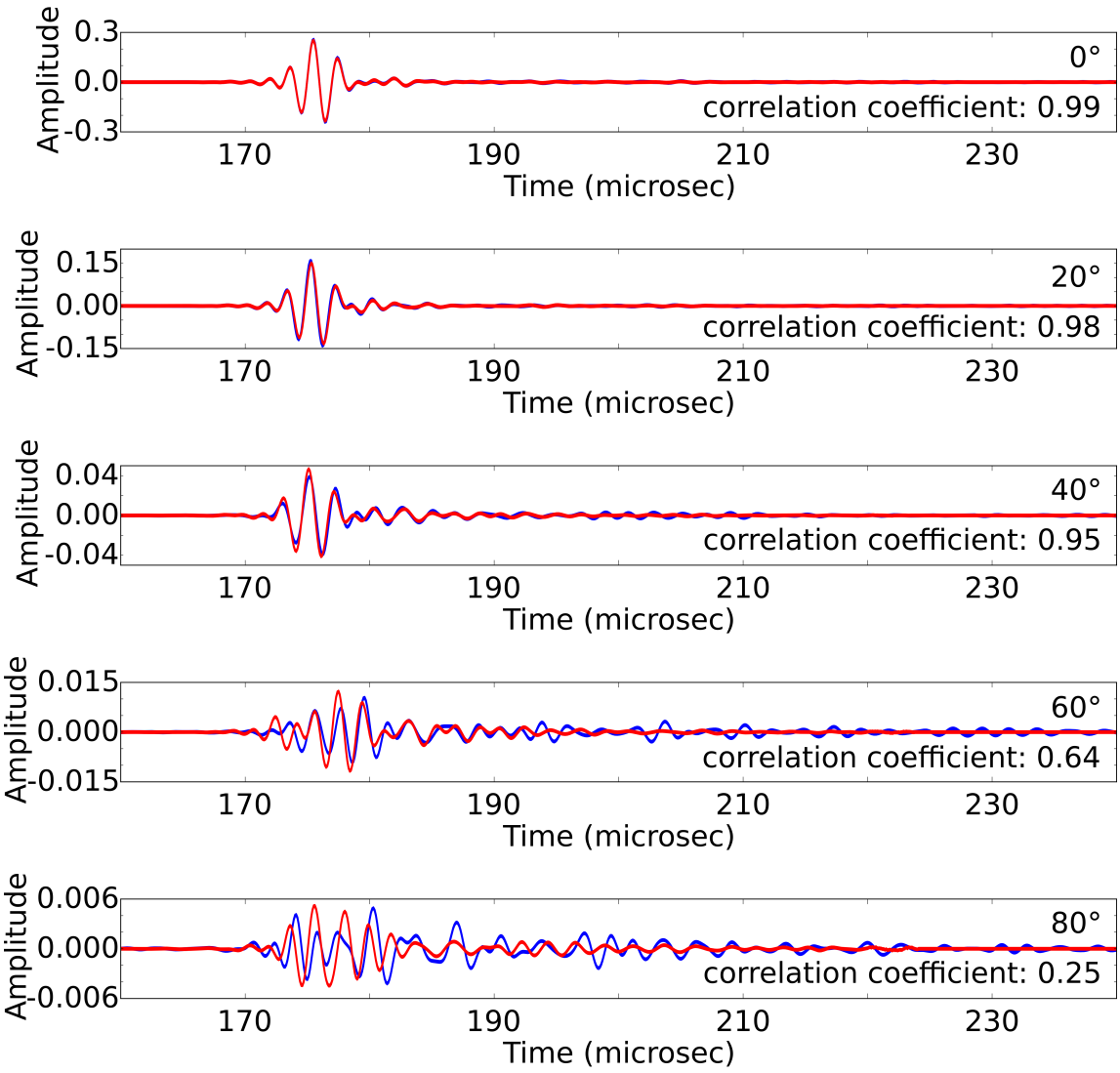

Figure 18. Comparison of the measured traces (blue) with the simulated traces (red), using the inverted equivalent source at different angles. The correlation coefficients are shown in each panel, respectively.

The procedure to obtain the numerically equivalent source in the zero-offset configuration is quite similar to the previous one, but it requires a deconvolution process before the inversion step (Figure 15). This is due to the fact that for zero-offset measurements the same transducer is used twice: first, as the source, and then, as the receiver. Therefore, an extra measurement is needed, using only the source transducer to measure the reflected wavefield from the water-air interface at normal incidence (at a distance of half of 259 mm). The deconvolution process is done in the frequency domain after a Fourier-transformation of all the recorded signals. Let us denote the laboratory trace recorded by the hydrophone opposite to the source

transducer as *trace 1* (Figure 16) and the trace recorded by the source transducer corresponding to the reflected wavefield from the water-air interface at normal incidence as *trace 2* (Figure 16).

The process can be summarized as follows:

- Step 1) Note that *trace 2* is the square of the source transfer function. Therefore, the square root of *trace 2* gives the source transfer function at 0°, i.e., in the opposite position to the source,

- Step 2) Because the hydrophone is omnidirectional, the receiver transfer function is the same at each angle α. Therefore, divide *trace 1* by the source transfer function (step 1) to determine the receiver transfer function $R(\omega)$,

- Step 3) Divide all the traces recorded by the hydrophone by the receiver transfer function $R(\omega)$ to get $S_\alpha(\omega)$ for each angle α (deconvolution in the time domain),

- Step 4) Take the square of $S_\alpha(\omega)$ for each α to obtain the zero-offset transfer function of the source transducer at each angle,

- Step 5) Inverse Fourier transform all the obtained traces to the time domain.

The data set derived using this deconvolution process is the input to the inversion process, which is the same as described above for the general offset case. According to our tests, the best fit between the measured and the inverted radiation patterns can be obtained with a disk radius of 6 mm, using 253 point sources and only one disk layer. Similar to the offset case, using more than 10 000 iterations did not provide any better result. The angle dependency in the goodness of fit is also valid for the zero-offset case. However, the range of the more accurate fit is broader (approximately ±35° around the center of the transducer). This is due to the fact that (relatively) more energy is focused in the central beam in this configuration, thus, the outer region (with lower signal-to-noise ratio) has less influence on the inversion of the main lobe.

2.3.4 Numerical calibration of the material properties

Because the characterization of the material samples yields a range of possible values for each measured property (Appendix A), an initial calibration is necessary to find the values to be used before the final simulations. The calibration consists of a zero-offset laboratory measurement, followed by an iterative fitting of the results of the numerical simulations of the same trace. The goal of this iterative fitting is to adjust the material parameters such that, the simulation yields the closest possible fit with the reference laboratory measurement. To have the least geometric effect on the calibration, a test point was chosen above the flat part of the Marseille-Benchie model (black cross in Figure 19). The velocities and Q-factors for P- and S-waves for the PVC were tested, while the densities of the PVC and the water, and the velocity of the P-waves in water were considered to be perfectly known. We note here that, in reality, the investigated parameters have a combined effect on the amplitude, phase, and arrival times, so the result of this calibration provides one possible solution in the parameter space. First, the P-wave velocity for the PVC was calibrated, then all the remaining differences between the reference laboratory trace and the simulated trace were attributed to V_S, Q_P, and Q_S.

The resulting parameters from the calibration were found to be V_P = 2260 m⁄s, V_S = 1050 m⁄s, Q_P = 28.7, and Q_S = 26. If we compare these values with those in Table 1, we can see that V_S and Q_S of the PVC are close to the measured values, but V_P and Q_P are significantly different. First, we need to highlight that accurately measuring attenuation is one of the major challenges of the laboratory work. Furthermore, the measured values strongly depend on the acquisition setup, i.e. the transducer height above the material sample. Namely, it has an important effect on the illumination of the material samples/physical model, resulting in different amplitudes recorded at different distances. Therefore the adjusted material parameters obtained by fitting a given reference laboratory trace are in fact not absolute, but only apparent values, like in the case of a real-life seismic data acquisition. This is why the reference trace must always be chosen in an area where the geometry is the closest to be one-dimensional.

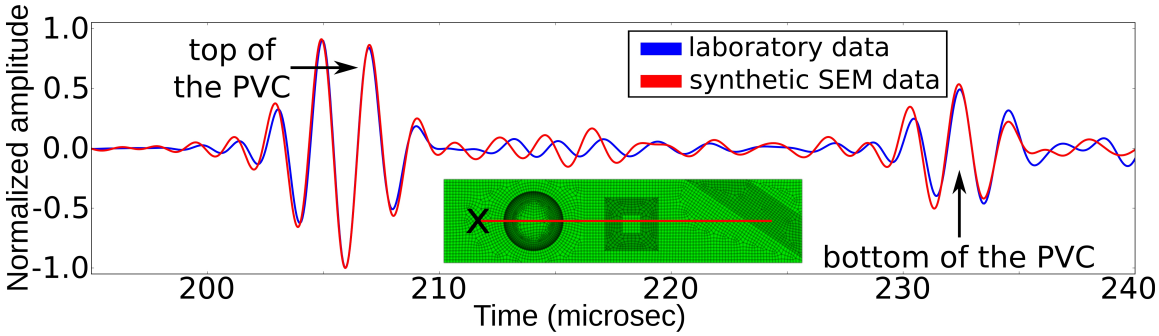

Figure 19. Comparison of the zero-offset laboratory trace with synthetic results for the test point to calibrate the material properties before the final simulations. The position of the test point is shown with the black cross.

2.4 About the finite-difference simulations

Although the primary numerical algorithm used in this thesis is the SEM, we also present finite-difference results in this part to show the capability of the method to reconstruct the complex wavefields recorded for the Marseille-Benchie model. The applied FDM is based on Virieux's (1986) velocity-stress formulation for an elastic medium. The spatial derivatives are computed using 8th order optimized differentiators (Holberg, 1987), whereas the temporal integration is 2nd order. The elastic scheme is extended to the viscoelastic case by the extension of the stress-strain relation (Ben-Menahem and Singh, 1981). For the free-surface implementation, the method of Mittet (2002) was used. The PML boundary conditions, the attenuation, and the source transducer were all implemented identical to the SEM (Sections 2.2.8, 2.3.2, and 2.3.3, respectively). The model geometry was discretized using a regular three-dimensional grid with a uniform grid spacing of 0.5 mm (corresponding to 10 m at seismic scale). It gives approximately 4.1 and 2.9 grid-points per the shortest wavelength for P- and S-waves, respectively. The FDM results presented in this thesis are the work of Børge Arntsen (NTNU, Trondheim, Norway), and they are showcased here as the result of the collaboration between the NTNU and the LMA (Arntsen et al., 2017, 2018).

PART 1

Chapter 3
Comparison of experimental and numerical data

3.1 Comparison of zero-offset data sets

Here, we consider more specifically three traces of the laboratory zero-offset section corresponding to the study line (red line in Figure 13). These traces (labeled as A, B, and C in Figure 9) are of particular interest because they contain diffracted waves generated by the feature edges, as well as reflections from the flat and curved surfaces of the model.

Trace A is located above the lower edge of the pyramid, where its flank meets the flat part (red cross in Figure 20). It is composed of several groups of reflections: from the side of the pyramid (denoted as event A1 in Figure 20), from the flat part (A3 and A4), from the bottom of the model below the flat part (A8 and A9), and below the dome (A10). Several groups of diffracted waves are also present, corresponding to diffractions: from the upper edge (A2) and the lower edge (A7) of the pyramid, and from the edge of the dome (A6). Event A5 is related to the truncated dome, which is not included in the simulations.

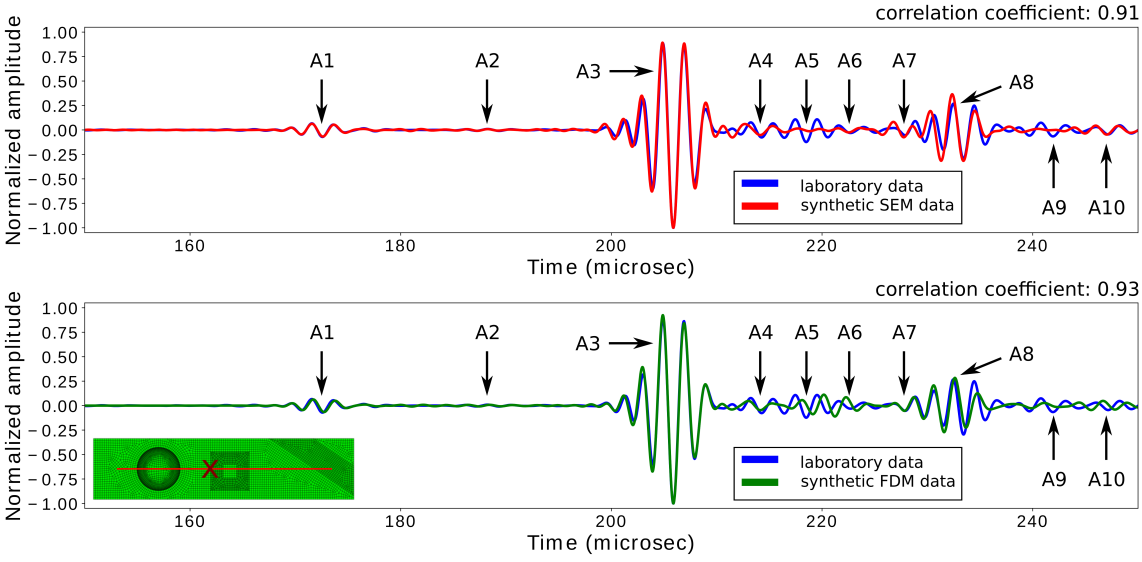

Figure 20. Comparison of zero-offset laboratory trace A with synthetic results obtained with the SEM (top) and the FDM (bottom). The physical interpretation of the annotated events is provided in the text.

Trace B is located half-way between the pyramid and the dome (yellow cross in Figure 21). It is composed of several groups of events associated with reflections: from the side of the dome (events B1 and B2 in Figure 21), from the side of the pyramid (B3), from the flat part (B4), and from the bottom of the model below the flat part (B6). Event B5 is the superposition of diffractions from the upper edge of the pyramid and from the edge of the dome. Event B7 corresponds to the superposition of a reflection from the bottom of the model below the dome and a diffraction from the lower edge of the pyramid.

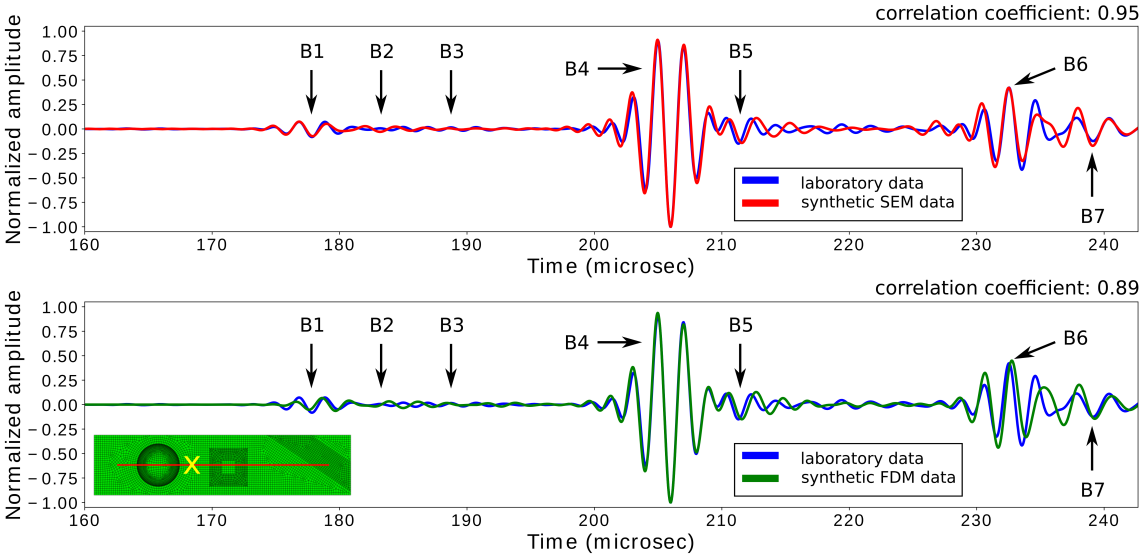

Figure 21. Comparison of zero-offset laboratory trace B with synthetic results obtained with the SEM (top) and the FDM (bottom). The physical interpretation of the annotated events is provided in the text.

Trace C is located on the other side of the dome, compared with traces A and B (Figure 22). It is composed of several groups of reflections: from the side of the dome (C1 and C2 in Figure 22), from the flat part (C3 and C4), and from the bottom of the model below the flat part (C6 and C7). Event C5 is a multiple of a diffraction from the lower edge of the dome, whereas event C8 is a multiple reflection.

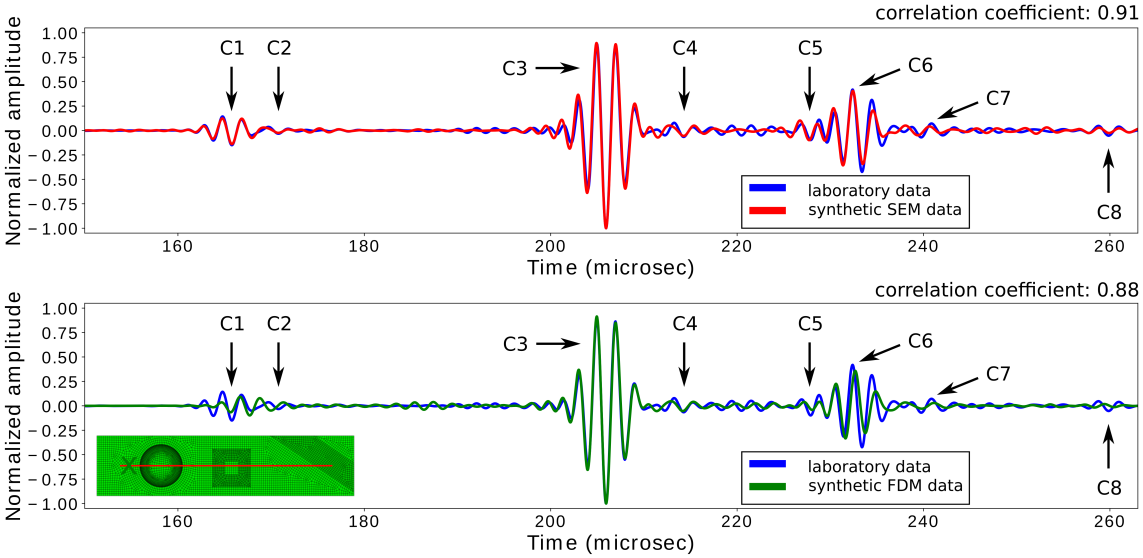

Figure 22. Comparison of zero-offset laboratory trace C with synthetic results obtained with the SEM (top) and the FDM (bottom). The physical interpretation of the annotated events is provided in the text.

It is important to note that the laboratory data are real data, so they also contain unknown noise recorded by the acquisition system. Furthermore, as shown in Figure 7, the source wavelet is a long signal, composed of a main event followed by a few tens of µs long low-energy tail with small amplitudes (ringing effect). It may explain the fact that some events are composed of two parts (e.g., events A8 and A9 in Figure 20; B1 and B2 in Figure 21; C1 and C2, C3 and C4, C6 and C7 in Figure 22).

Qualitative comparisons between laboratory and synthetic traces show a quite good fit in amplitude, phase, and travel time. Regardless of the trace location, synthetic traces show an almost perfect fit with the experimental data in time, phase, and amplitude for the reflected events from the top and bottom of the flat part of the model. The early and late parts of these arrivals sometimes reveal minor amplitude misfits, most probably due to the low-energy second part of the source signal, which may not be perfectly reconstructed by the source inversion, as well as the uncertainties in the attenuation parameters chosen for the simulations. Events associated with the side reflections and/or diffractions from the topographic features are also well restored by the simulations (see events A1 in Figure 20, B5 and B6 in Figure 21, and C1 and C8 in Figure 22).

PART 1

The correlation coefficients between the laboratory and the spectral-element traces are 0.91, 0.95, and 0.91 for traces A, B, and C, respectively. These good results are due to the fact that SEM has the ability to honor the model geometry, even for tilted and curved interfaces by using a non-structured mesh. The correlation coefficients between the laboratory and the finite-difference traces are 0.93, 0.89, and 0.88 for traces A, B, and C, respectively. These high values show a very good fit with the laboratory data, which is ensured by the high number of grid points per wavelength during the finite-difference simulations. Comparing either the correlation coefficients obtained by the two numerical methods, or the traces visually, both the FDM and the SEM show a very similar fit with the laboratory measurements. Both the arrival times and the amplitudes of the different arrivals are well restored, however, small differences can be pointed out. Event A1 is very well reconstructed by both methods, suggesting that the finite-difference grid is fine enough to represent the tilted sides of the pyramid. To the contrary, events B1 and C1 show some minor misfits between the finite-difference traces and the laboratory measurements. These small misfits suggest that the finite-difference grid should be even finer to better reconstruct the reflections from the strongly curved surface of the dome. The fact that the misfit is more pronounced for event C1 shows that the closer we are to the curved interface, the more misfit can be observed due to the grid representation of the geometry in the FDM. Diffractions are properly handled by both methods in general. For example event B5 is reconstructed to the same extent by both methods. However, the FDM shows some more misfit for event C5 than the SEM.

3.2 Comparison of offset data sets

Here, we consider more specifically two traces of the laboratory offset section, labeled as D and E in Figure 10. The source location is above the flank of the dome for both traces (yellow asterisk in Figures 23 and 24).

The receiver for trace D is located next to the ramp (blue triangle in Figure 23). The trace contains several groups of events, mainly associated with the direct source-receiver travel path (labeled as D1 in Figure 23), the reflection from the top of the truncated pyramid (D2), and the reflection from the curved surface of the dome (D3).

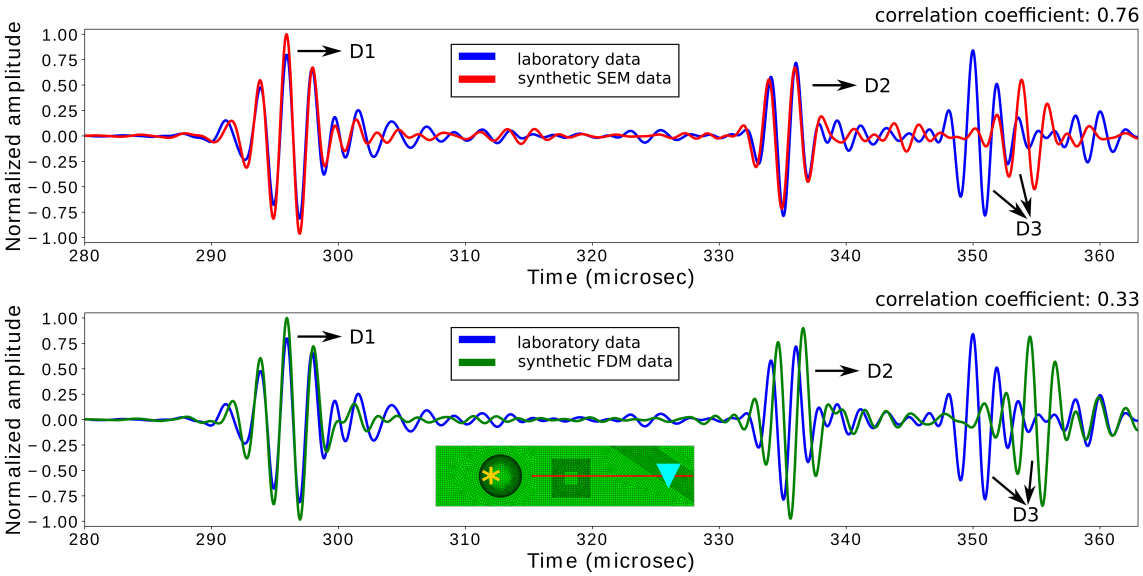

Figure 23. Comparison of offset laboratory trace D with synthetic results. The physical interpretation of the annotated events is provided in the text. Top: spectral-element simulation, bottom: finite-difference simulation.

The receiver for trace E is located between the dome and the pyramid (yellow triangle in Figure 24). Event E1 is the direct arrival from the source to the receiver. The other interpreted events are related to reflections from the dome (E2), from the flat part (E3), and from the pyramid (E4).

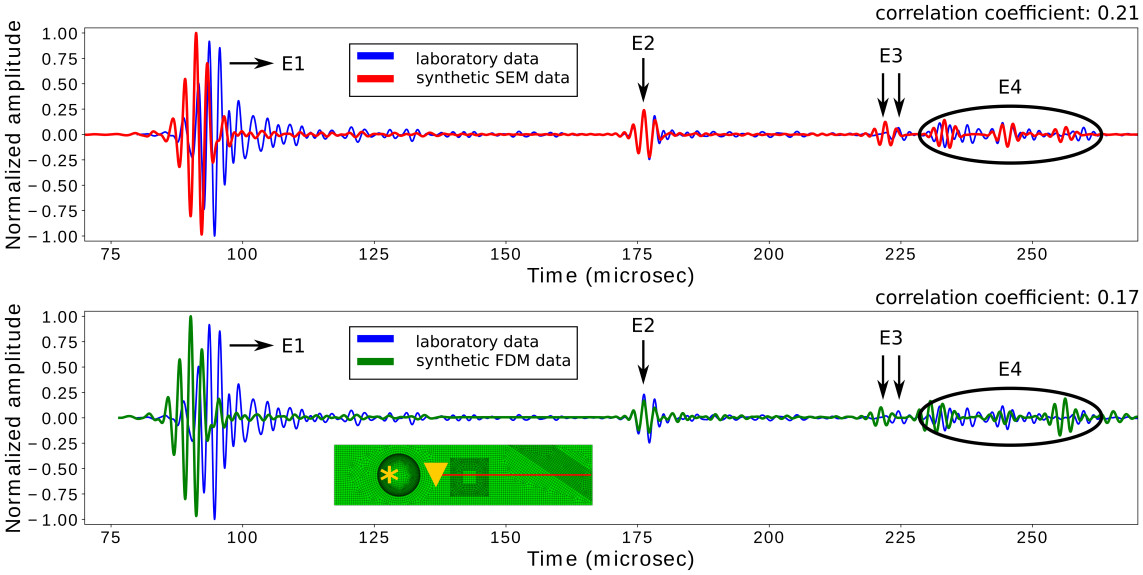

Figure 24. Comparison of offset laboratory trace E with synthetic results. The physical interpretation of the annotated events is provided in the text. Top: spectral-element simulation, bottom: finite-difference simulation.

A qualitative comparison between the simulated results and the laboratory data shows a good fit in arrival time, phase, and amplitude for some events (D1 and D2 (only for the SEM) in Figure 23, and E2 and some parts of E4 (only for the SEM) in Figure 24). However, other events related to reflections from the dome (D3), from the flat part (E3), and from the pyramid (E4) show significant arrival time and amplitude misfits. We note that the different traces show a different quality of wavefield reconstruction, corresponding to the same object, and depending on the offset. For example, the reflection from the dome is correctly reconstructed on trace E (event E2), but with a misfit on trace D (event D3). To the contrary, the comparisons show a perfect reconstruction of the reflection from the pyramid in the case of trace D (event D2) and a misfit for trace E (event E4).

The correlation coefficients between the measured and simulated trace D are 0.76 and 0.33 for the SEM and the FDM, respectively. Comparing the different numerical results with the laboratory trace in Figure 23, we see a significantly higher amplitude and arrival time misfit for the FDM for the reflection from the pyramid (event D2). This may be explained by the grid representation of the model geometry in the finite-difference simulations, similar to the misfits pointed out for the zero-offset traces above. The two numerical methods show more or less the same reconstruction of the reflection from the dome (D3), with the same arrival time misfit, but a smaller amplitude misfit in the case of the FDM.

In the case of trace E, the correlation coefficients between the laboratory and the synthetic results are 0.21 and 0.17 for the SEM and the FDM, respectively. These low values are due to the similarly high misfit for both algorithms in the reconstruction of the direct source-receiver path (event E1). This is proven by the fact that, if the direct arrival was not considered, the same correlation values for trace E would be 0.51 and 0.32, for the SEM and the FDM, respectively. We recall that the implementation of the numerically equivalent source has higher uncertainties for the low-energy later part of the source wavelet and the secondary lobes (due to the low signal-to-noise ratio of these events) than for the main lobe of the directivity pattern. Even if they carry less energy than the main lobe, the role of these higher order lobes in the illumination of the model should not be neglected in the case of offset configurations. Because the direct arrival is much more related to the secondary lobe for trace E than in the case of trace D, we can understand the difference in the lower quality reconstruction of the direct arrival for trace E, as opposed to the perfect reconstruction for trace D. The reflection from the dome on trace E (event E2) is well reconstructed by both numerical methods in time, but the FDM shows a lower amplitude than the

SEM/laboratory measurements. Reflections from the pyramid on trace E (event E4) show a very similar reconstruction by the two methods, but the FDM shows somewhat more misfits (e.g. the SEM can correctly reconstruct the measurements around 245 μs, whereas the FDM has both amplitude and arrival time misfits). We highlight again that these higher misfits pointed out for the FDM, compared with the spectral-element results, may be attributed to the grid representation of the model geometry. It means that the differences between the two numerical methods should entirely diminish with an even finer finite-difference grid.

3.3 Discussion

As shown above, both the SEM and the FDM can reproduce laboratory zero-offset data in terms of arrival time, phase, and amplitude with high accuracy. However, the fit between synthetic results and experimental offset data is significantly less accurate. We discuss here the possible explanations for this observation, including the experimental uncertainties and the numerical implementation of the directivity pattern of the source transducer, as well as the computational cost.

Laboratory data always contain noise and offset data sets generally have a lower signal-to-noise ratio than the zero-offset data. Moreover, uncertainties in the transducer positions also have an effect on the data. It is more significant in the offset case because there is a nonlinear combination of uncertainties in the source location, the source tilt angle, and the receiver position. This nonlinear combination makes it difficult to evaluate the role of one effect over the others. This effect is even more pronounced in the presence of strongly tilted and curved interfaces, causing wave defocusing.

Let us analyze here this source of misfit and quantify the order of magnitude of the possible resulting uncertainty. We show an example of the Marseille-Benchie model using the dome. The geometry of the problem is shown in Figure 25, where R denotes the radius of the dome, H is the height of the source transducer above the top of the dome, γ is the incidence angle, α is the angle of the reflected wave, l_1 is the distance from the source to the incidence point, θ is the angle between the vertical line below the source position and the incidence point from the center of the dome, l_2 is the distance between the incidence point and the source level along the line defined by θ, and the sum of x and y is the theoretical offset of the reflected wave. For now, we suppose that the source is located exactly above the top of the dome. We are interested

in the change in the offset of the arrival of a given ray due to an error $\delta\gamma$ in the incidence angle γ. If R, H, and γ are known, then θ can be calculated using the law of sines:

$$\theta=\pi-\gamma-\sin^{-1}\left(\frac{R+H}{R}\sin(\gamma)\right) \quad . (14)$$

Using simple trigonometry, we can now calculate x, l_1, l_2, α, and y:

$$x=(R+H)\tan(\theta) \quad , (15)$$

$$l_1=\sqrt{(R+H)^2+R^2-2R(R+H)\cos(\theta)} \quad , (16)$$

$$l_2=\frac{R+H}{\cos(\theta)}-R \quad , (17)$$

$$\alpha=\cos^{-1}\left(\frac{l_1^2+l_2^2-x^2}{2l_1l_2}\right) \quad , (18)$$

$$y=\frac{l_2\sin(\alpha)}{\cos(\theta+\alpha)} \quad . (19)$$

If the uncertainty of the incidence angle $\delta\gamma$ is known, then $\delta\theta$ can be calculated using equation 14, where $\delta\theta$ is the shift in θ due to the error in the incidence angle. Furthermore, we can also calculate the changes in x, l_1, l_2, α, and y:

$$\delta x=\frac{R+H}{\cos^2(\theta)}\delta\theta \quad , (20)$$

$$\delta l_1=\frac{R(R+H)\sin(\theta)\delta\theta}{l_1} \quad , (21)$$

$$\delta l_2=\frac{R+H}{\cos^2(\theta)}\sin(\theta)\delta\theta \quad , (22)$$

$$\delta\alpha=\frac{x\delta x-l_1\delta l_1-l_2\delta l_2}{l_1l_2\sin(\alpha)} \quad , (23)$$

$$\delta y=\delta l_2\frac{\sin(\alpha)}{\cos(\theta+\alpha)}+l_2\delta\left(\frac{\sin(\alpha)}{\cos(\theta+\alpha)}\right) \quad , (24)$$

where the sum of δx (equation 20) and δy (equation 24) is the shift in the offset of the reflected wave due to the error $\delta\gamma$ in the incidence angle γ. To quantify the order of magnitude of the offset error, we consider H=140 mm, R=51.25 mm, and γ=5°. Supposing an error of $\delta\gamma$=0.5° in the incidence angle, the point of illumination on the surface of the dome is shifted by 1.3 mm. Using equations 20 and 24, we get δx=5.2 mm and δy=1.5 mm, respectively. It means that an error of 0.5° in the incidence angle leads to a shift of 6.7 mm (134 m at seismic scale) in the arrival offset of the beam (i.e. in the receiver location), depending on the point of the illumination of the surface of the dome. This uncertainty may thus have a significant impact on the arrival time and the amplitude of the reflected and diffracted events. This is illustrated in Figure 26 for offset trace D, where two synthetic traces are compared using a 1° different tilt angle of the source transducer. Although the differences for the reflection from the dome are negligible, the direct arrival and the reflection from the pyramid show a significant misfit between the two traces.

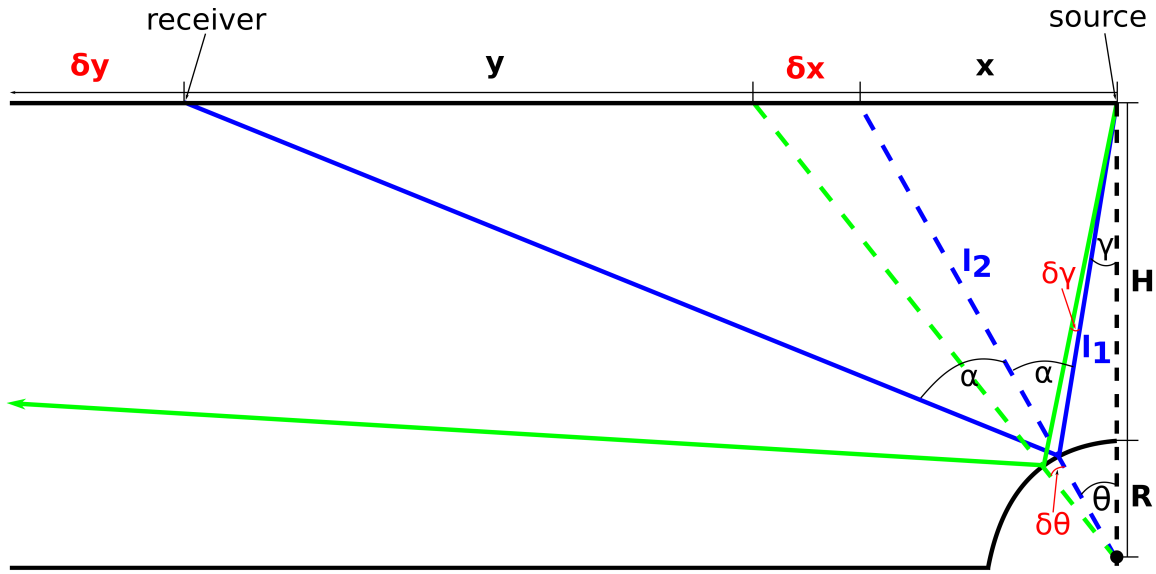

Figure 25. The effect of the uncertainties in the incidence angle on the wavefield.

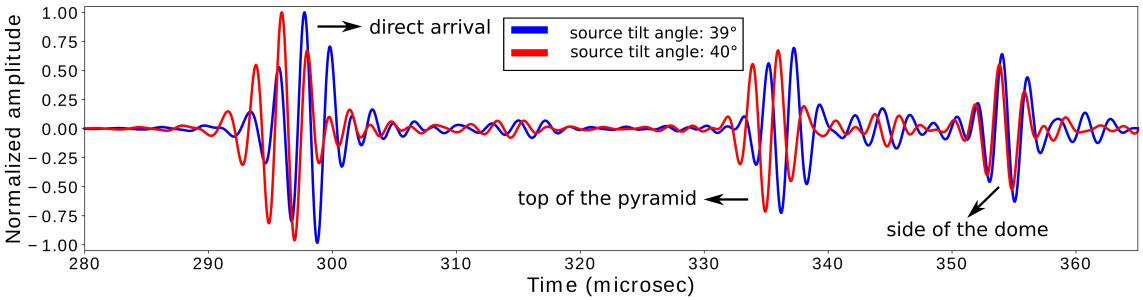

Figure 26. The effect of 1° difference in the tilt angle of the source transducer on the simulated SEM wavefield (offset trace D).

We note that the sometimes observable higher misfits for the finite-difference results compared with the SEM are related to the grid representation of the model geometry in the FDM. These misfits should entirely disappear with an even finer finite-difference grid.

We have proposed a strategy to numerically implement the directivity pattern of the real source transducer. This strategy permits to recover the main lobe of the emitted beam, in which most of the energy is concentrated. The excellent fit between synthetic results and laboratory zero-offset data shows that the strategy is efficient in zero-offset configurations because mostly the main lobe illuminates the model and contributes to the recorded data. Nevertheless, for offset data recorded in strong topographic environments, the proposed strategy is less accurate because the low-energy later part of the source wavelet (Figure 7) and the secondary lobes play an important role in the illumination of the model, even if they carry far less energy than the main event of the source wavelet in the main lobe (Figure 17). Indeed, in our case, they may interact with the dome and the pyramid (depending on the source location), influencing the amplitude and phase of the wavefield.

The computational cost of the numerical methods is often an important point, particularly in the operational context of seismic exploration. Here, we differentiate between the man-hour cost spent on the preparation of the simulations and the computational cost (i.e., the number of processors used for simulations times the actual running time of one simulation). In general, the SEM has a large man-hour cost, due to the non-structured hexahedral meshing. To illustrate this problem, we note that we spent a few weeks to find the optimal meshing strategy for the Marseille-Benchie model, without finding a satisfying strategy for the truncated dome. Contrary to finite-difference gridding, there is no quick or cheap solution to non-structured hexahedral meshing in terms of man-hour cost. Regarding the computational cost of

the method, we used Intel Xeon Sandy Bridge EP (E5-2680) processor cores for the spectral-element simulations. The initial meshing strategy resulted in a mesh that required 10150 core hours to simulate 350 μs of wave propagation (corresponding to 7 s at seismic scale). Using the optimized meshing strategy of Appendix B, this cost was reduced to 1611 or 2538 core hours, depending on the element size. The computational cost of the FDM was 32 GPU hours for the simulation of 350 μs of wave propagation, using Nvidia GForce GTX Titan X graphics cards. We note that depending on the graphics card, the CPU cost of Specfem must be divided by a factor of more than an order of magnitude to obtain the corresponding GPU hour value (Komatitsch et al., 2010). Therefore, in practice, the two methods have roughly the same computational cost for the Marseille-Benchie model. Based on this observation, in an operational context, the FDM can be optimal if the model geometry often changes due to the lengthy meshing step before the spectral-element simulations. However, the finite-difference grid must be very fine, as we have seen before.

PART 1

Conclusions of Part 1

The goal of Part 1 is to provide a workflow to adapt the numerical simulations and the small-scale laboratory experiments to each other, such that the two can be easily compared with high accuracy and confidence. We are also interested in the ability of the SEM and the FDM to accurately simulate complex 3D wavefields including (multiple) diffractions at the lowest possible computational and man-hour cost. We have thus compared 3D synthetic results with laboratory measurements in 3D zero-offset and 3D offset offshore reflection configurations for the Marseille-Benchie small-scale physical model. The model includes structures with steep flanks, sharp edges, corners, and curved interfaces. This complexity provides a challenge to any numerical method to reproduce the wavefield.

Prior to the simulations, we have focused on the input data/parameters, such as the material properties, the model geometry, and the characteristics of the source and receiver transducers. The material properties have been characterized in the laboratory and calibrated for the numerical simulations. The viscoelastic behavior of the material used in the model has been approximated with a set of standard linear solids in the numerical simulations. The real source transducer characteristics have been implemented based on a new approach, which consists of the laboratory characterization of the impulse response of the transducer, followed by an inversion step to obtain a numerically equivalent source for the numerical simulations. The zero-offset measurement requires an additional deconvolution step before the inversion because, in that case, only one transducer is used as both the source and the receiver.

We have suggested an optimization of the spectral-element computational cost, by using larger elements in the non-structured mesh and higher order polynomial basis functions. This technique helps to significantly reduce the computational cost while obtaining a similar level of accuracy. Comparison of the zero-offset synthetic and laboratory results has revealed an excellent fit in terms of arrival time, phase, and amplitude, for both the SEM and the FDM. Minor amplitude mismatches may be attributed to the noise recorded in the laboratory data, as well as to the inaccuracy of the proposed source implementation to reconstruct the low-energy secondary lobes of the source transducer, and the uncertainties in the attenuation parameters chosen for the simulations.

PART 1

Comparison of – both SEM and FDM – simulated and laboratory offset traces has exhibited a good fit in terms of amplitude, arrival time, and phase, but with significantly less accuracy for some arrivals than in the zero-offset case. This can be mainly attributed to the inaccuracies of the transducer positions during the laboratory measurements combined with the strong topography of the model, as well as to the smaller signal-to-noise ratio of the offset configuration.

Smaller misfits between the finite-difference and the spectral-element synthetic results may be attributed to the grid representation of the model geometry in the finite-difference simulations, which should be completely resolved with an even finer grid.

Considering the above-mentioned misfits and discoveries, we propose some points to work on in the future. Based on their importance and difficulty to be implemented, we divide them into near-term and long-term categories. The necessary near-term developments had to be addressed during the thesis before using the complex WAVES model in Part 2. These include:

- the development of a more accurate acquisition system to reduce the inaccuracies in the transducer positions during the laboratory measurements,
- a more accurate measurement of the tilt angle of the source transducer in offset configurations.

The long-term developments may take more time and some of them may need the expertise of metrologists. These include:

- revisiting the proposed numerical implementation of the real transducer to account more for the low-energy secondary lobes, and the low-energy late-arrivals of the source wavelet,
- reconsidering the laboratory techniques used to characterize the properties of the material samples, especially for S-waves, and for the attenuation parameters,
- assessing the noise level of the acquisition system and improving its signal-to-noise ratio,
- identifying the origin of the different noises measured temporarily or permanently in the laboratory,
- reducing the man-hour cost of the SEM due to the lengthy meshing step.

PART 2

APPLICATION TO A

REALISTIC GEOLOGIC SETUP –

THE WAVES MODEL

PART 2

Introduction

Geologic salt structures are economically important because hydrocarbon reservoirs are often situated in their proximities. These structures usually play a crucial role in the migration and the entrapment of the hydrocarbons, therefore the detailed understanding of their geologic layout is essential in exploration geophysics. Because salt often behaves and moves similar to fluids at the geologic time scale, it can have various forms, ranging from horizontal sheets to vertical 'plums', or even mushroom- and dome-shaped forms (see for example Tari et al., 2003, and Jackson and Hudec, 2017) (Figure 27). Salt is usually characterized with high velocity (approximately 4000-5000 m/s), especially when compared with typical sedimentary layers. The density of the salt is generally close to that of the sediments, but due to the higher velocity, the surfaces of the salt structures usually have a high reflectivity. Because only a small portion of the incident energy can propagate inside, or even across the salt, the proper imaging of their internal structures is a big challenge. Imaging structures below the salt layers (aka sub-salt imaging) is even more complicated, although sometimes inevitable for the complete understanding of the geologic setup. Various works have been published on (sub-)salt imaging, focusing on either the post-processing of already acquired data sets (e.g., Jiao et al., 2006, Ravaut et al., 2008, Oropeza et al., 2009), or on the acquisition techniques and the acquisition geometry (e.g., Krail, 1993, Lindsay et al., 2000, Long et al., 2013). A proper (sub-)salt imaging technique is still an ongoing challenge for seismic exploration.

PART 2

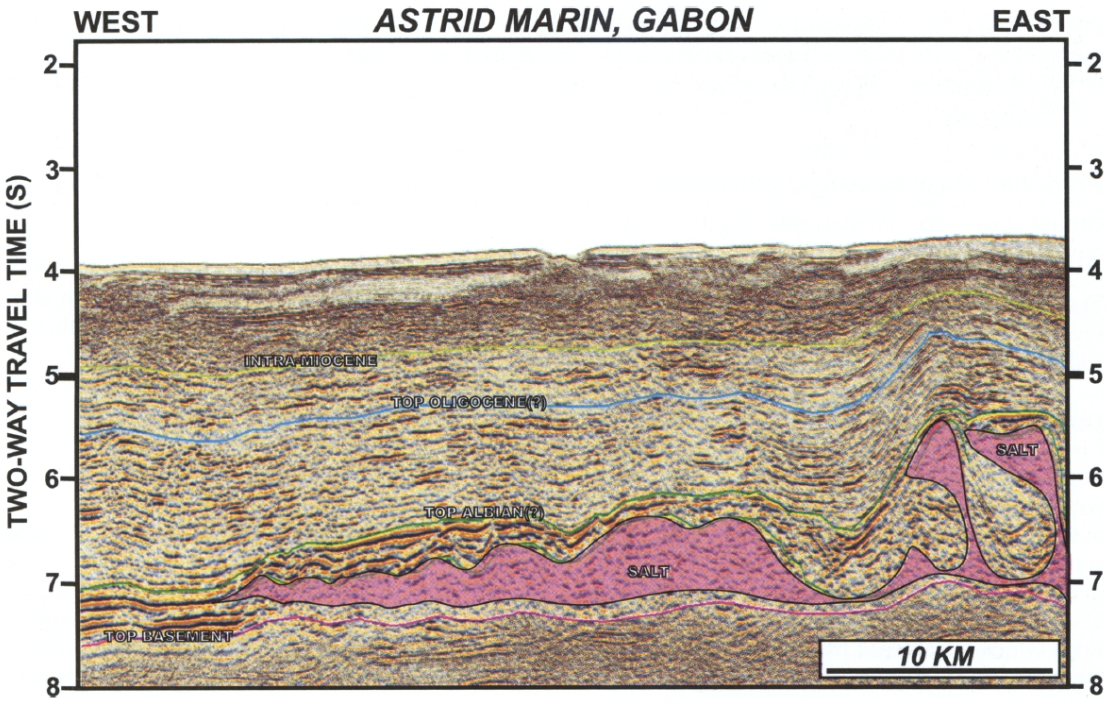

Figure 27. Example of the various forms of salt structures (in pink) on an interpreted seismic section from Gabon (from Tari et al., 2013, Figure 11).

As mentioned in the General Introduction, there is a strong interest in using small-scale physical models to evaluate the accuracy of the numerical algorithms used in seismic exploration (e.g., Igel et al., 2000, Campman et al., 2005, Mittet, 2017), and also to better understand the wave propagation phenomena in realistic geologic setups (e.g., Wapenaar and Berkhout, 1987, Favretto-Anrès and Rabau, 1997, Cooper et al., 2010). This interest is especially strong in the case of geologic setups including salt structures. Therefore the goal of this part is to respond to this demand by, first, building a realistic small-scale model, and then, precisely implementing the model and the laboratory experiments in the numerical domain. The WAVES model was designed with the intention to mimic a realistically challenging salt-dome geologic setup at laboratory scale. It includes a salt-dome in the middle, surrounded by different sedimentary layers, and a crystalline basement on the bottom. For the numerical implementation, we rely on the framework established in Part 1, following some technical modifications of the laboratory equipment to increase the precision of the transducer positioning and the tilt angle of the source transducer.

Chapter 1 is dedicated to the laboratory aspects. The physical model is described, including its geometry and the most important material properties. Then, we discuss the modifications of the acquisition system compared to Part 1, and the interpretation of some laboratory cross-sections are also showcased in zero-offset and offset configurations. Chapter 2 highlights the differences in the numerical simulations for the WAVES model compared to Part 1, including the implementation of the model geometry using a structured 3D mesh. The extension of the numerical calibration of the material properties to the multi-layered WAVES model is also discussed here. The comparison of the synthetic results with the laboratory measurements is presented in Chapter 3. Both 3D zero-offset and 3D offset cases are compared with the forward-simulated spectral-element results. The generally good fit between the measurements and the synthetic results are discussed in details, together with the occasional misfits and their explanations.

As showcased in the General Introduction, many different numerical algorithms are used in seismic exploration during survey design, data processing and interpretation (Robertsson et al., 2007), as well as in seismic imaging and inversion (Virieux et al., 2011). Reverse-time migration (RTM) is one of the most popular imaging techniques and it can reconstruct the seismic reflectors related to reflection coefficient contrasts (e.g., Zhang et al., 2003, Zhu et al., 2009). Applying the RTM to the laboratory data measured for the WAVES model is an optimal benchmarking opportunity for the established framework of Part 1. Therefore we showcase the RTM in Chapter 4, using the example of the WAVES model. First, the theoretical background of the RTM is briefly summarized together with the description of the necessary laboratory measurements, then the resulting RTM kernels are presented.

PART 2

Chapter 1
Small-scale seismic experiments

1.1 The WAVES model

The WAVES model represents the real geologic setup at the scale of 1:20 000. The physical model has a size of 400 x 270 x 95 mm^3, i.e. 8 x 5.4 x 1.9 km^3 at seismic scale. The model includes a salt-dome in the middle, surrounded by different sedimentary layers (Figure 28). Salt is represented by crystal (glass enriched with lead monoxide), and the sediments are represented by resins (Table 2). The resins are all based on the same base material, and some of them are enriched with a mixture of aluminum and silicon dioxide powder to increase their densities and the velocity of the ultrasonic waves. The aluminum layer on the bottom represents a typical crystalline basement, such as granite. The glass dome was manufactured by *La Fonderie de Verre*, while the other parts were manufactured by *VN Composites*, who also assembled the whole physical model. The assembly started with the aluminum plate, on which the first resin layer was poured (layer #4 in Figure 28). Then it was constantly rotated in an oven and the temperature was gradually decreased over a few hours to avoid air bubbles forming in the resin, and also to ensure the homogeneous distribution of the Al-SiO_2 powder in the base resin. After solidifying, the top surface of the resin layer was craved out according to the previous 3D plans. Finishing the fabrication of the first resin layer, the process continued with the next layer above (layer #3 in Figure 28), and so on. Before finishing the topmost resin layer (layer #1 in Figure 28), the glass dome was placed inside. Its coupling with the surrounding layers is ensured by a thin layer of the base resin.

PART 2

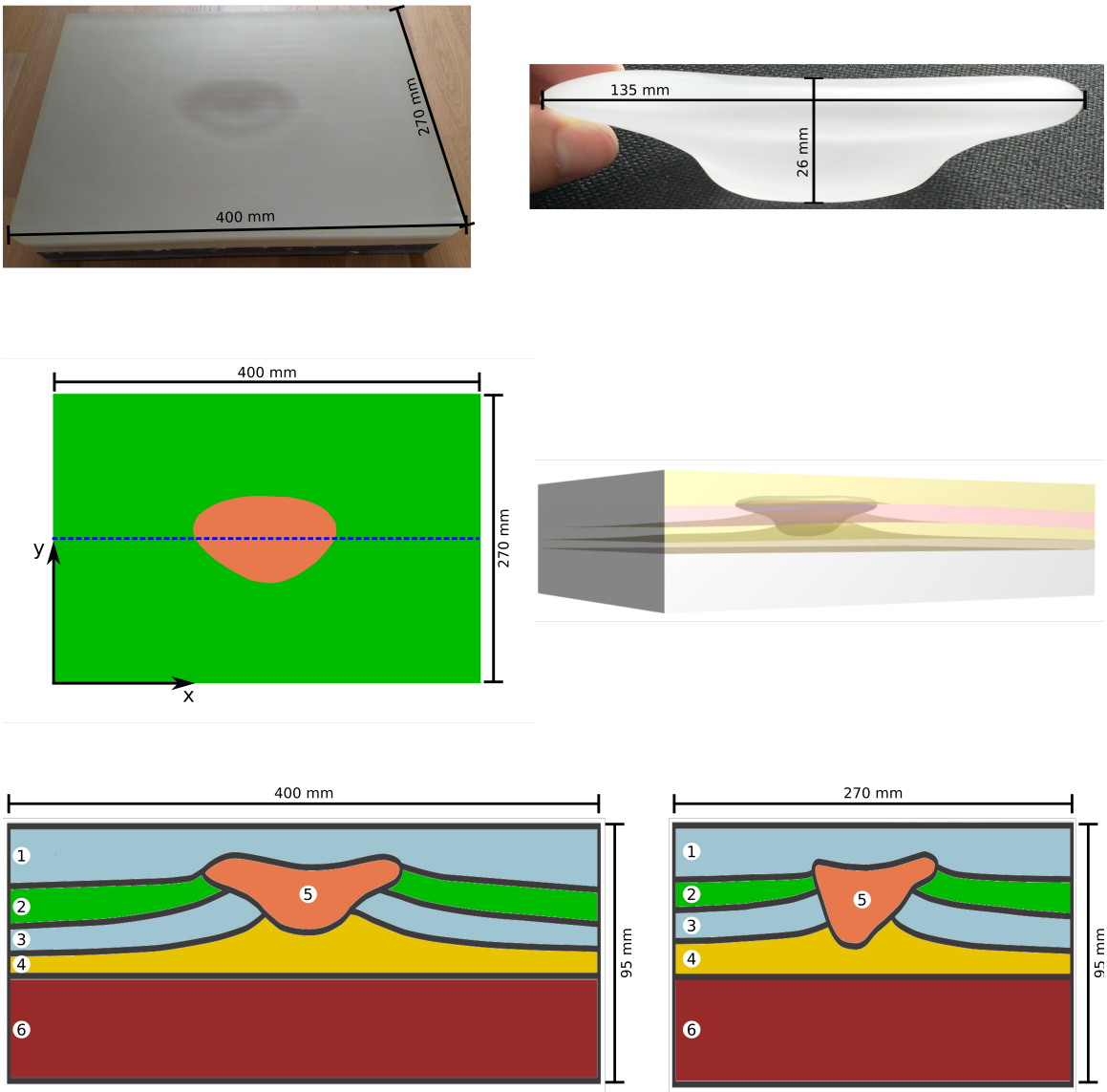

Figure 28. Top: the WAVES model after the assembly (left), the glass dome placed inside (right). Middle: top view of the WAVES model without the topmost layer, the blue dashed line denotes the study line discussed in the thesis (left), snapshot of the 3D geometry file (right). Bottom: perpendicular vertical cross-sections along the center lines of the model. The numbers denote the different materials, whose properties are shown in Table 2.

Similar to Part 1, the properties of the material samples of each material used in the WAVES model were characterized (Appendix A). The measured velocity and attenuation values (expressed as Q-factors) are close to constant and each material is considered to be homogeneous and isotropic for the frequency range of interest (250-650 kHz). According to both the literature and our measurements, we consider glass and aluminum to be elastic, i.e. Q_P and Q_S are infinite. Appendix A contains the measured values at each characterized frequency and Table 2 shows the values considered valid for the whole frequency range of interest after evaluating the measurement uncertainties as well.

Material	**Number in Figure 28**	**Density (kg/m^3)**	**V_P (m/s)**	**V_S (m/s)**	**Q_P**	**Q_S**
resin A	1, 3	1172 ± 2 (± 0.2 %)	2720 ± 13 (± 0.5 %)	1210 ± 144 (± 12 %)	25 ± 1 (± 4 %)	11 ± 4 (± 36 %)
resin B	2	1680 ± 10 (± 0.6 %)	3090 ± 16 (± 0.5 %)	1577 ± 25 (± 1.6 %)	26 ± 1 (± 4 %)	18 ± 3 (± 17 %)
resin C	4	1800 ± 10 (± 0.6 %)	3470 ± 21 (± 0.6 %)	1840 ± 101 (± 5 %)	53 ± 1 (± 2 %)	33 ± 9 (± 27 %)
crystal glass	5	3623 ± 10 (± 0.3 %)	4480 ± 43 (± 1 %)	2845 ± 464 (± 16 %)	∞	∞
aluminum	6	2710 ± 4 (± 0.2 %)	6441 ± 87 (± 1.4 %)	3573 ± 544 (± 15 %)	∞	∞

Table 2. Measured properties of the materials used in the WAVES model for the frequency range of interest (250–650 kHz).

PART 2

1.2 Improved experimental setup and laboratory data sets

Similar to Part 1, the WAVES model was immersed in a water tank during the measurements (Figure 3). Compared to the time when the measurements were conducted for the Marseille-Benchie model, the precision of the measurements has been significantly improved. As listed in the necessary near-term modifications in the Conclusions of Part 1, optic rulers have been installed to provide a precise a posteriori control of the transducer movements, as well as a digital protractor to measure more accurately the tilt angle of the source transducer. Due to these modifications, the uncertainty of the transducer movements has been reduced to ±5 μm (i.e. ±0.1 m at seismic scale), while the tilt angle of the source transducer can be measured with a precision of ±0.1°. Therefore the precision of the transducer movement and the source tilt angle have been improved by a factor of 100 and 10, respectively, compared to Part 1. The laboratory measurements have been conducted identical to Part 1, and we refer the reader to Section 1.2 in Part 1 for further details.

For the sake of brevity, we focus on a study line, located above the center line in the x-direction (dashed line in Figure 28 middle left, and along the section shown in Figure 28 bottom left). This acquisition line covers both rather simpler parts close to the sides, where the geometry consists of close-to-horizontal layers, and complex parts in the center, above the dome. Figure 29 shows the laboratory zero-offset data set for the study line, together with the interpretation of the main recorded events. The transducer was positioned 100±0.1 mm above the top surface of the model (i.e. 2000±2 m at seismic scale). Event a) represents the reflections from the top surface of the model, i.e. from the top of the *upper resin A* layer. Event b) represents the top of the *glass* dome. It mainly consists of reflections, between positions 120-270 mm. For positions less than 120 mm and greater than 270 mm diffractions from the edges of the dome can be observed. Events c), d), e), and f) represent the top surface of *resin B*, *lower resin A*, *resin C*, and *aluminum*, respectively. These events can be easily interpreted on the sides due to the relatively simple geometry. To the contrary, the closer we are to the center of the model, the harder it is to distinguish the same reflections due to the more complex geometry. Thanks to the broad-beam radiation pattern of the source transducer and the curved top surface of the dome, we can see a constructive interference of reflections in the center, leading to focusing of the energy, between 165-200 μs and between positions 170-240 mm. Event g) shows reflections from the bottom of the *aluminum*. The fact that reflections are recorded from the bottom of the *aluminum* shows that the imaging of the entire depth of the model is

possible, even though the resin layers are highly attenuating (Table 2). Similar to the Marseille-Benchie model, we can see velocity pull-up effects due to the time-domain visualization. Namely, events f) and g) represent reflections from two perfectly horizontal interfaces, but in Figure 29 they show some undulations. This is due to the varying velocity of the complex overburden of the aluminum, which leads to different arrival times of the reflected zero-offset waves at different horizontal positions.

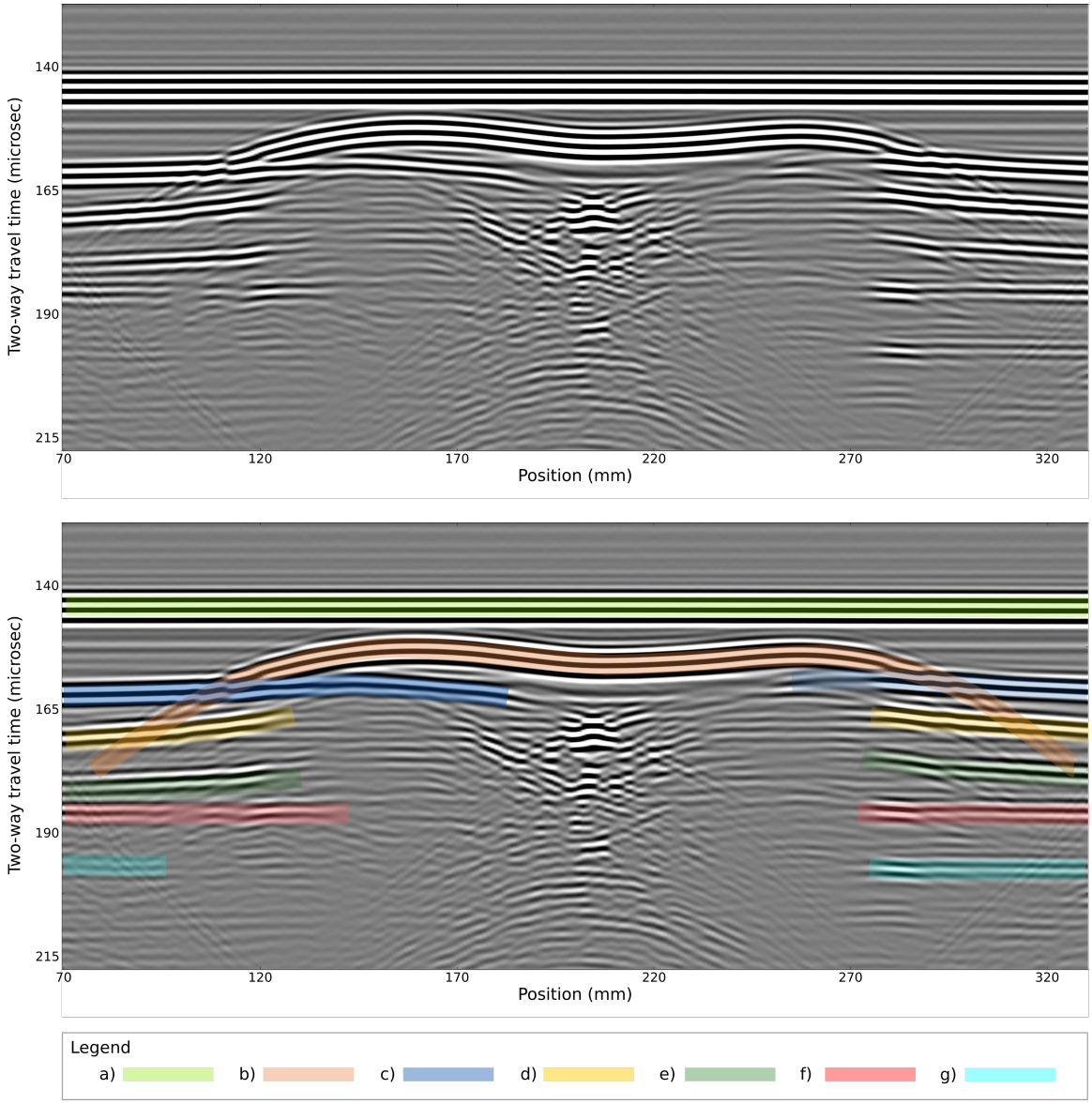

Figure 29. Cross-section of the laboratory zero-offset data set along the study line (top), and interpretation (bottom). Annotated events: reflections from the (a) top of *upper resin A*, (b) top of *glass dome*, (c) top of *resin B*, (d) top of *lower resin A*, (e) top of *resin C*, (f) top of *aluminum*, and (g) bottom of *aluminum*. The data was filtered between 250-650 kHz.

Figure 30 shows the acquisition layout of the laboratory offset data set presented in Figure 31. This latter is a common shot gather along the study line together with the interpretation of the main events. The source was positioned at y=390.17±0.50 mm and the tilt angle of the source transducer was 30±0.1°. Both the source and the receiver transducers were positioned 100±0.1 mm above the top surface of the model (i.e. 2000±2 m at seismic scale). The interpretation of the measured data set for the WAVES model without post-processing is much more challenging than in the case of the Marseille-Benchie model. This is due to the complex geometry of the multi-layered WAVES model. Event a) can be attributed to the direct arrival from the source, and event b) to the reflections from the top surface of the model, i.e. from the top of the *upper resin A* layer. To better understand the laboratory data, it must be post-processed, most typically with migration algorithms, to which we show an example in Chapter 4 (see Figure 47).

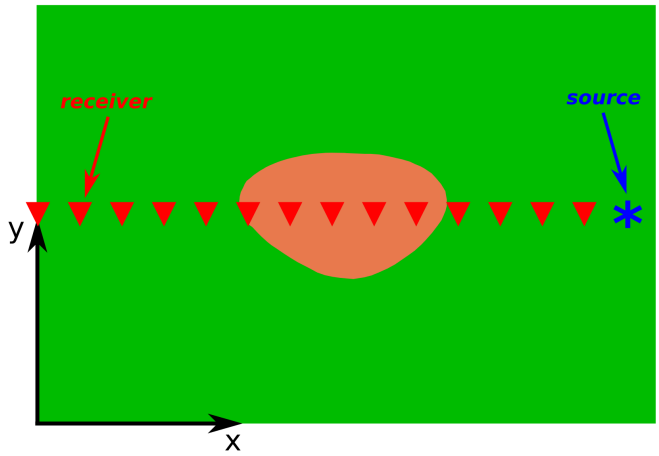

Figure 30. Acquisition geometry of the laboratory offset section presented in Figure 31.

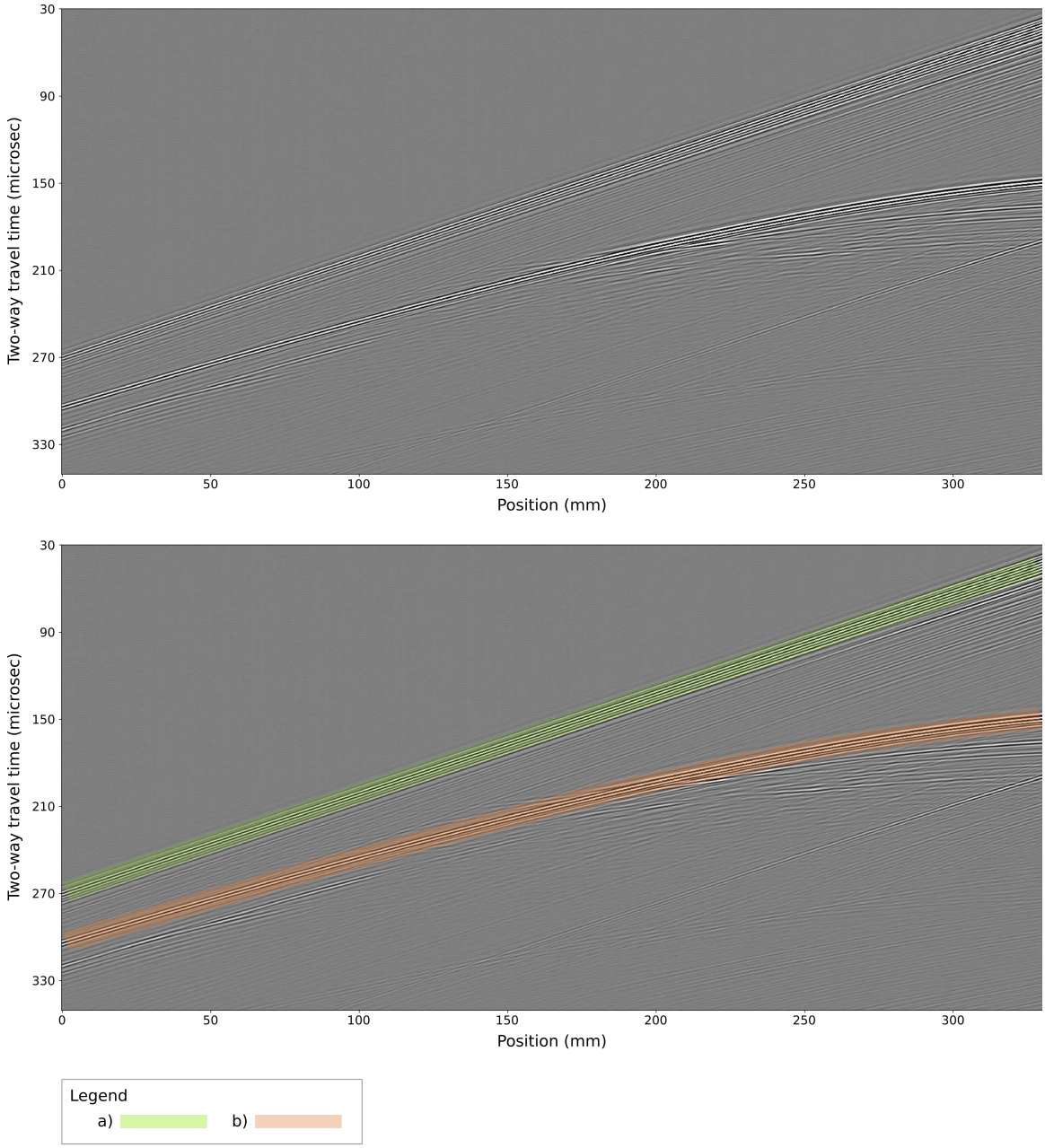

Figure 31. Cross-section of the laboratory offset data set along the study line (i.e. common shot gather) (top), and interpretation (bottom). Annotated events: (a) direct arrival, (b) reflection from the top of upper *resin A*. The data was filtered between 250-650 kHz.

PART 2

Chapter 2
Numerical modeling of the laboratory measurements

2.1 Spectral-element simulations with a structured mesh

We use the Specfem software package for the numerical simulations, as presented in Chapter 2 in Part 1. The only difference compared to Part 1 is the numerical implementation of the model geometry. Because the WAVES model has a complex multi-layered 3D geometry, obtaining a hexahedral non-structured mesh is extremely difficult. The main difficulty is not only to correctly mesh any domain of the model with hexahedral elements only but also to have a conform mesh on the boundaries between any two domains. In a conform mesh, all nodes which are on the boundary of two domains are shared by elements on both sides, and all elements on the boundaries must be connected to elements in the other domain by nodes (Figure 32). Although we tested several available open-source and commercial meshing tools, currently they are all unable to tackle this task for the WAVES model. Because a conform mesh is necessary for the numerical simulations, we had to use a different approach to numerically implement the model geometry.

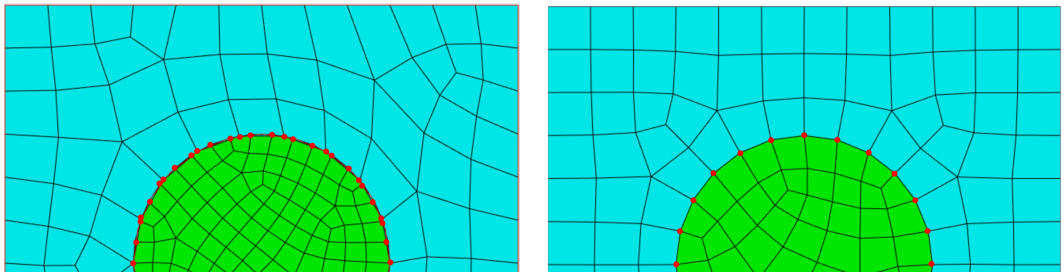

Figure 32. Examples of a 2D non-structured mesh using quadrangles to showcase the difference between a non-conform (left) and a conform (right) mesh. The red dots denote the nodes on the boundary of the two domains.

Our solution is to use a structured grid, similar to the FDM. It is not unusual to use spectral-element algorithms with a structured grid, especially in seismic inversion, where the mesh has to be updated after each iteration. Considering the minimum velocity of the model – namely, 1210 m/s for the S-waves in *resin A* – and the maximum target frequency (650 kHz), we used a regular grid with an equidistant grid spacing of 1.6 mm in each spatial directions. Because five GLL points per element are

used during the simulations, the grid spacing provides at least 3.8 and 3.1 GLL points per the shortest wavelength for P- and S-waves, respectively. This spatial discretization yields approximately 5.6 million elements, considering the water column above the model as well.

2.2 Numerical calibration of the material properties for a multi-layered model

As mentioned in Part 1, an initial calibration of the measured material properties is necessary before the final numerical simulations. Here we follow the procedure presented in Section 2.3.4 in Part 1 to calibrate the material properties of the WAVES model using the zero-offset configuration. The goal of the calibration is to adjust the material properties of each layer such that the synthetic traces fit the laboratory traces as much as possible. Compared to the Marseille-Benchie model where the properties of only one material had to be fitted, the WAVES model is more challenging due to its multi-layered geometry. Our strategy for the WAVES model is simple: at first, the properties of the topmost layer are calibrated, then, those of the second layer, and so on. Similar to Part 1, we chose a reference point 100±0.1 mm above the top surface of the model, and as close to the sides of the model as possible, where the geometry is close to a 2D layer-cake geometry. The calibration thus consists of two phases: first, the properties of each layer are calibrated, except those of the glass dome, using the reference trace, then, a second trace is used in the center of the model to fit the properties of the glass as well (Figure 33).

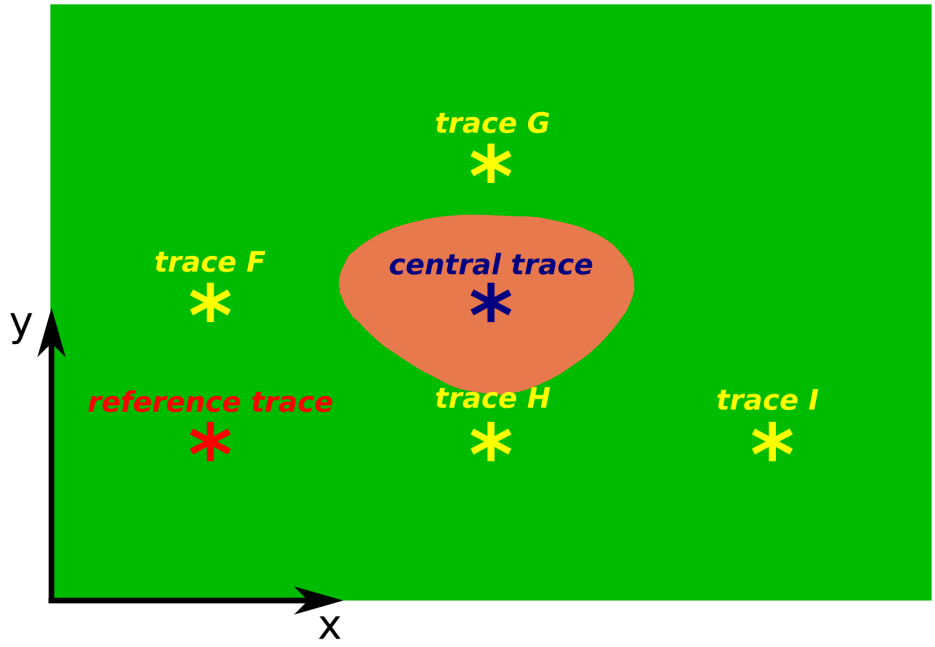

Figure 33. Location of the reference trace (red asterisk) and of the second trace used to calibrate the properties of the glass (blue asterisk). The yellow asterisks denote the position of the zero-offset examples showcased in Chapter 3.

Figure 34a shows the comparison of the reference laboratory trace with the result of the simulation, using the measured material properties (Table 2). Although the arrival time, amplitude and phase of the simulation are correct for the first event (reflection from the top of *upper resin A*), the later arrivals have extremely low amplitudes compared to the laboratory measurement. By adjusting the material parameters of the different layers, we can obtain an excellent fit between the laboratory and synthetic traces, as shown in Figure 34b. Table 3 shows the adjusted material properties and the change in terms of percentage compared to the measured material properties listed in Table 2. We note that, even though the same *resin A* is used twice in the model, we obtained different material properties for the upper and lower layers, especially for the attenuation parameters. Using the calibrated material properties of Table 3, we did an additional control measurement and simulation in the same horizontal position, but one centimeter closer to the surface of the model (i.e. 90±0.1 mm above the top surface of the model). Figure 35 shows that changing only the height of the transducer results in a different fit between laboratory and synthetic traces. It can be explained by the fact that, the illuminated zone of the model changes with the transducer height. Therefore we can clearly see the importance of the illuminated zone on the measurements, and on the calibration as well. Thus the adjusted material parameters

are rather apparent and not absolute, as it has already been pointed out in Part 1.

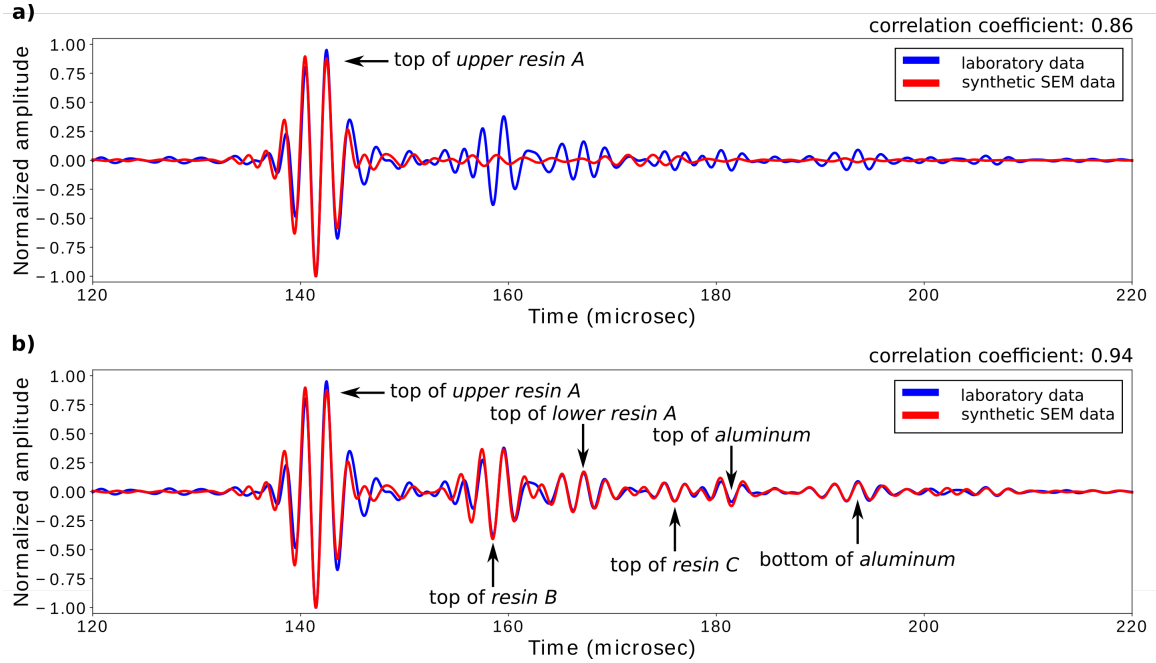

Figure 34. Comparison of the reference laboratory trace (blue) and the corresponding synthetic trace (red): a) using the measured material properties shown in Table 2, b) using the adjusted material properties shown in Table 3.

Layer	**Number in Figure 28**	**Density (kg/m^3)**	**V_P (m/s)**	**V_S (m/s)**	**Q_P**	**Q_S**
upper resin A	1	1172 (0 %)	2549 (-6 %)	1210 (0 %)	123.8 (376 %)	88 (389 %)
resin B	2	1680 (0 %)	3213 (4 %)	1577 (0 %)	27.3 (5 %)	23 (28 %)
lower resin A	3	1172 (0 %)	2560 (-6 %)	1210 (0 %)	41.7 (60 %)	30 (67 %)
resin C	4	1800 (0 %)	3050 (-12 %)	1840 (0 %)	30 (-43 %)	26 (-21 %)
aluminum	6	2710 (0 %)	6491 (< 1 %)	3573 (0 %)	∞ (0 %)	∞ (0 %)

Table 3. The calibrated material properties for the *resins* and the *aluminum*. The percentages show the differences compared to the measured values listed in Table 2.

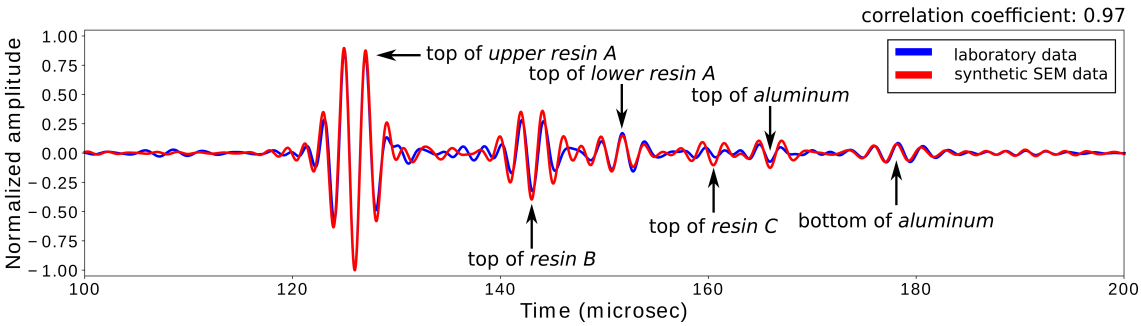

Figure 35. Comparison of the laboratory trace (blue) at the same horizontal position as the reference trace (Figure 34), but one centimeter closer to the model and the corresponding synthetic trace (red), using the adjusted material properties in Table 3.

After calibrating the material properties for the *resins* and the *aluminum*, a second trace was used in the center of the model to adjust the properties of the *glass* too (blue asterisk in Figure 33). Figure 36a shows the comparison of the laboratory trace with the synthetic results, using the adjusted material properties listed in Table 3. We can see that the two traces fit each other very well for the reflection from the top of the *upper resin A* layer. Figure 36b shows the same comparison between the laboratory trace and the synthetic results, but this time the material properties of the glass dome are also calibrated (Table 4). We can clearly see a good fit in Figure 36b between the laboratory and synthetic traces for the reflection from the bottom of the *glass* dome too, as well as for other events with later arrival times. The reflection from the top of the *glass* dome shows a good, but not a perfect fit, as mainly the amplitude is different from the laboratory measurement. To decrease this misfit, the properties of *upper resin A* had to be readjusted. In other words, it points out a need to adjust differently the properties of the same layer in different positions. It could mean that the materials used in the model would be heterogeneous, but that is not confirmed by our measurements for the material samples. On the contrary, the effect of the illuminated zone may also depend on the model geometry, especially in this case when the top surface of the dome is curved, and not only on the transducer height.

PART 2

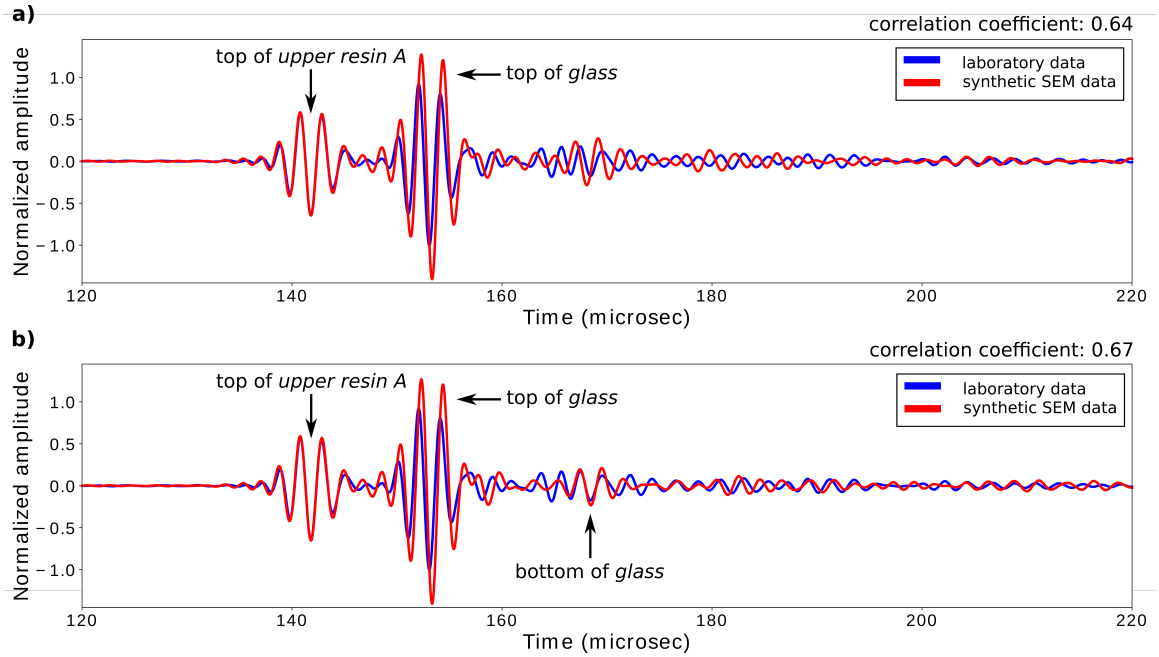

Figure 36. Comparison of the laboratory trace (blue) in the center of the model and the corresponding synthetic trace (red): a) using the adjusted material properties in Table 3, b) using the adjusted material properties in Table 4, which is calibrated for the properties of glass too.

Layer	**Number in Figure 28**	**Density (kg/m^3)**	**V_P (m/s)**	**V_S (m/s)**	**Q_P**	**Q_S**
glass	5	3623 (0 %)	4325 (-4 %)	2845 (0 %)	∞ (0 %)	∞ (0 %)

Table 4. The calibrated material properties for the *glass*. The percentages show the differences compared to the measured values listed in Table 2.

Chapter 3
Comparison of experimental data with forward simulations

3.1 Comparison of zero-offset data sets

Here, we consider more specifically four traces of the laboratory zero-offset data set, denoted with the yellow asterisks in Figure 33. These traces are located at different parts of the model to investigate the fit between the measurements and the simulations, using the calibrated material properties (Tables 3 and 4) at different positions.

Trace F is located about 130 mm (i.e. 2.6 km at seismic scale) far from the reference trace in the y-direction (Figure 33). The comparison of the laboratory measurement with the numerical result shows a good fit for most of the events (Figure 37a). The first three reflections (from the top of *upper resin A*, *resin B* and *lower resin A* layers, respectively) show a good fit in terms of the arrival time and amplitude. Furthermore, even the reflection from the top of *resin C* shows only some minor amplitude and arrival time misfits. On the contrary, the reflections from the top and bottom of the *aluminum* reveal a significant misfit in the arrival times. The correlation coefficient of the two traces is 0.93, highlighting the general good fit for both the arrival times and the amplitudes.

Trace G is located about 130 mm far from the reference trace in both the x- and y-directions, i.e. altogether 184 mm (i.e. 3.68 km at seismic scale) far from the reference trace (Figure 33). Although this trace shows a perfect fit for the reflection from the top of *upper resin A* layer, the later arrivals suffer from a varying degree of amplitude and arrival time misfits (Figure 37b). The simulated amplitude is especially high compared to the measurements for the reflection from the top of *resin B;* whereas erroneously low for the reflections from the top of *lower resin A*, and the bottom of the *aluminum*. The correlation coefficient of 0.82 reveals too the generally good phase and arrival time, and the occasionally imperfect amplitudes.

Trace H is located about 130 mm (i.e. 2.6 km at seismic scale) far from the reference trace in the x-direction, on the other side of the dome than trace G (Figure 33). Figure 37c shows a good fit between the measurements and the simulations for the reflection

from the top of the *upper resin A* layer. This is mainly true for the center of this event, as the beginning and the end show some minor amplitude misfits. The reflections from the top of *resin B* and *lower resin A* show some amplitude misfits, similar to trace G. On the contrary, the later arrivals of trace H show an almost perfect fit in both the arrival times and the amplitudes, as opposed to trace G. Because of the smaller amplitude misfits, trace H has also a higher correlation coefficient (0.87).

Trace I is located about 260 mm (i.e. 5.2 km at seismic scale) far from the reference trace in the x-direction (Figure 33). Figure 37d shows the comparison between the measurement and the simulation, revealing a generally good fit. The fit is especially good for the reflections from the top of *upper resin A*, and *resin B*. The reflections from the top of *lower resin A* and *resin C*, and from the bottom of the *aluminum* show some amplitude and arrival time misfits. On the contrary, the amplitude and arrival time misfits for the reflection from the top of the *aluminum* are significant. We also note the arrival recorded after the reflection from the top of the *upper resin A* layer, around 148 μs. This event is pronounced for the measurement, while not reconstructed with the simulation. This arrival is probably related to tiny air-bubbles accumulated on the surface of the physical model during the measurements, which can take even several days for the entire data set. Trace I has a correlation coefficient of 0.88, which would be even higher if the bubble-related event would not show a difference with the simulation.

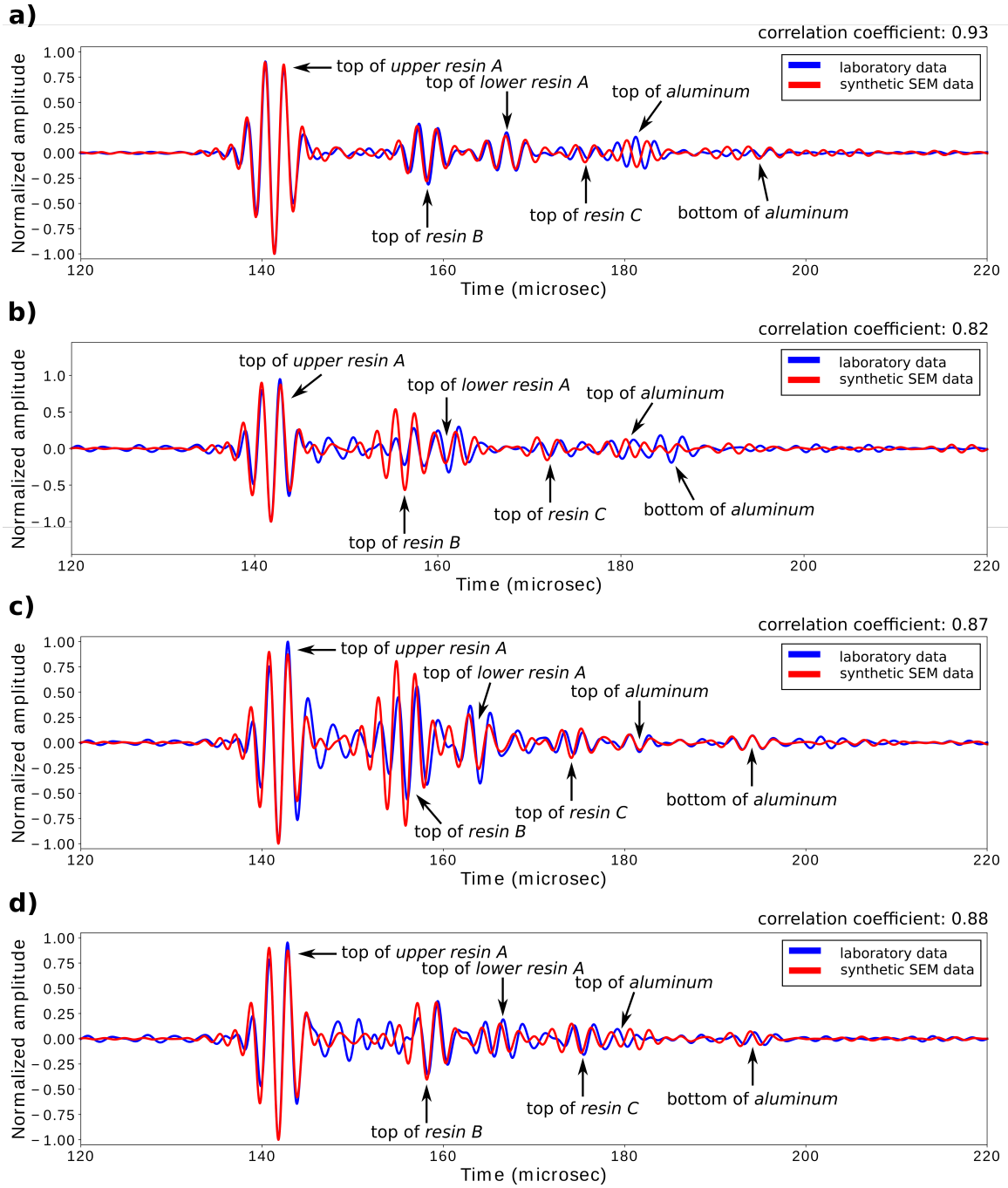

Figure 37. Comparison of zero-offset laboratory traces with the corresponding synthetic SEM results: a) trace F, b) trace G, c) trace H, d) trace I.

3.2 Comparison of offset data sets

Here, we consider more specifically two sets of offset traces, corresponding to two different source positions. All the sources and receivers were positioned in the center line of the model in the y-direction (y=135±0.5 mm). The two source positions are denoted with red and blue asterisks in Figure 38, respectively. The positions of the receivers are denoted with triangles of the corresponding colors. The tilt angle of the source transducer for all the traces was 31.3±0.1°. As noted in Section 3.2 in Part 1, the direct arrival can be reconstructed only with a varying goodness of fit in the offset configuration, due to the numerical implementation of the secondary lobes of the source transducer. Therefore we do not show here the direct arrival for any of the traces, as that would for example bias the correlation coefficients.

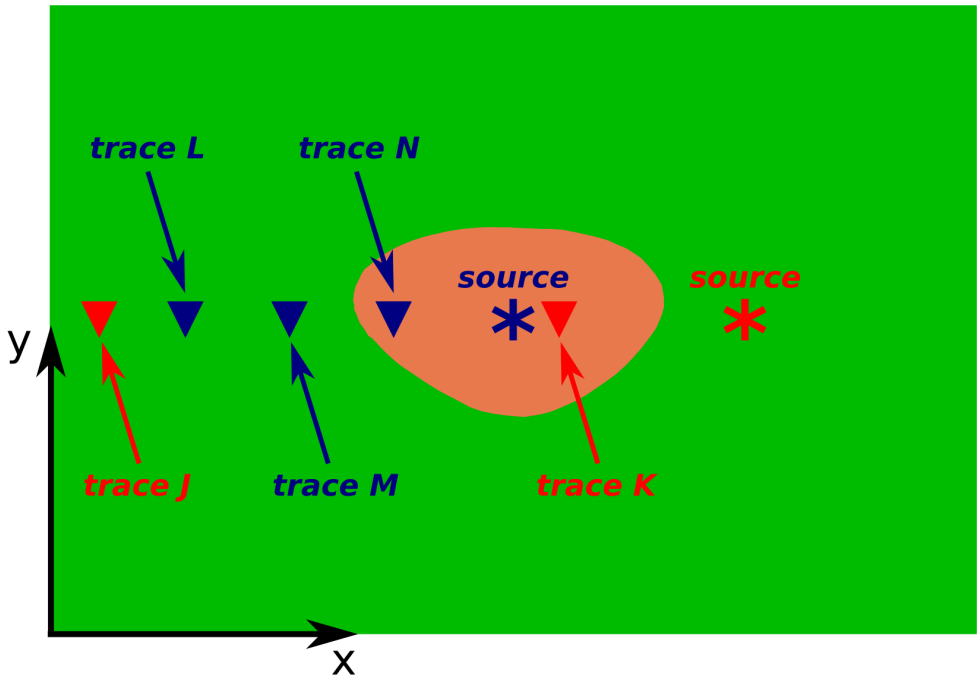

Figure 38. Location of the sources (asterisk) and receivers (triangles) associated to the two showcased offset experiments. The two data sets are denoted with red and blue colors, respectively.

3.2.1 First set of offset traces

The source was positioned at x=300±0.5 mm for traces J and K (Figure 38). Trace J corresponds to an offset of approximately 280 mm (i.e. 5.6 km at seismic scale). Figure 39a shows the comparison of the laboratory measurement with the synthetic result. The reflection from the top of *upper resin A* shows a good fit between the two traces, in terms of both the arrival time and the amplitude. Although the arrival time of the reflection from the top of the *glass dome* is correct for the synthetic trace, the simulated amplitude is somewhat lower compared to the measurement. The later arrivals which propagated through the *glass dome* cannot be easily interpreted one-by-one, because they belong to complex ray paths. Although the arrival time and phase of these events are correct, they show a varying amplitude misfit. The correlation coefficient of 0.84 also suggests a generally good fit between the measurement and the simulation.

Trace K was measured at an offset of approximately 80 mm (i.e. 1.6 km at seismic scale). The comparison of the measured and simulated traces in Figure 39b shows a good fit for the reflection from the top of *upper resin A*, similar to trace J. Following that, there are two arrivals corresponding to reflections from the top of the *glass dome*. This is due to the broad-beam radiation pattern of the source in combination with the curved top surface of the dome. These arrivals show some arrival time and amplitude misfits. The later arrivals, corresponding to waves propagating through the glass dome, show a similar pattern as for trace J. Namely, the arrival time of these events are mostly correct with some amplitude misfits. The correlation coefficient is 0.81, partly due to the erroneously low simulated amplitude of the later arrivals (e.g. at 180 μs).

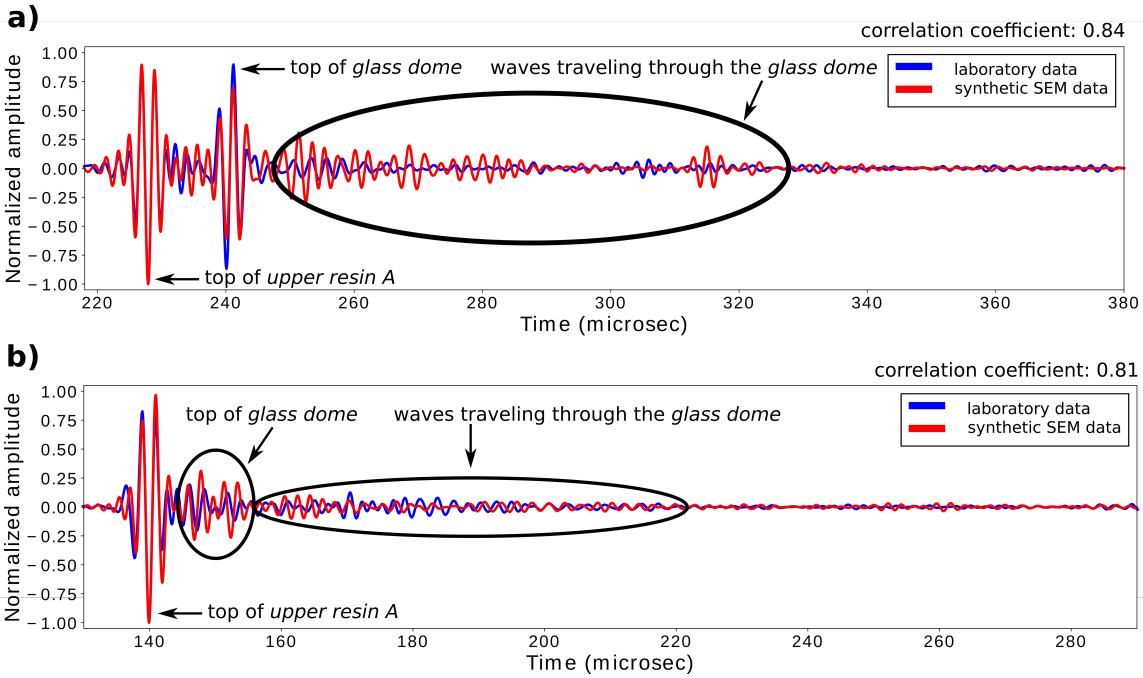

Figure 39. Comparison of offset laboratory traces with the corresponding synthetic SEM results: a) trace J, b) trace K.

3.2.2 Second set of offset traces

For the second set of offset traces, the source was positioned at x=200±0.5 mm (Figure 38). Trace L corresponds to an offset of approximately 140 mm (i.e. 2.8 km at seismic scale). The reflection from the top of *upper resin A* has the correct arrival time and amplitude, but the phase of the early and late parts of this event is somewhat distorted, compared to the laboratory trace (Figure 40a). The reflection from the top of the *glass dome* shows mainly some amplitude misfit. The simulated arrivals of the waves traveling through the *glass dome* show an erroneously low amplitude in general. It explains also the lower correlation coefficient of 0.78 compared with traces J and K above.

Trace M (Figure 40b) corresponds to an offset of approximately 90 mm (i.e. 1.8 km at seismic scale). The reflection from the top of *upper resin A* shows a good fit in time and amplitude. The early and late parts of this event have a somewhat superior fit in phase than for trace L. The two reflections from the top of the *glass dome* are of excellent fit in both arrival times and amplitudes. However, the later arrivals, corresponding to waves propagating through the dome, again reveal an erroneously low amplitude for the synthetic trace. The correlation coefficient is 0.81, and this higher value compared with trace L is due to the better fit at earlier times.

Trace N (Figure 40c) corresponds to an offset of approximately 50 mm (i.e. 1 km at seismic scale). This near-offset trace shows an excellent fit in arrival times and amplitudes for the reflections from both the top of *upper resin A* and the *glass dome*. For this trace, even the beginning of the complex arrivals related to rays propagating through the *glass dome* shows a good fit between the simulation and the measurement. Indeed the arrival at around 150 µs has both the good amplitude and arrival time with a minor phase misfit. Later parts of these arrivals show also a rather good fit in time. Similar to the previous traces, the simulated amplitude of these events after 180 µs are generally too low, explaining also the lower correlation coefficient of 0.78.

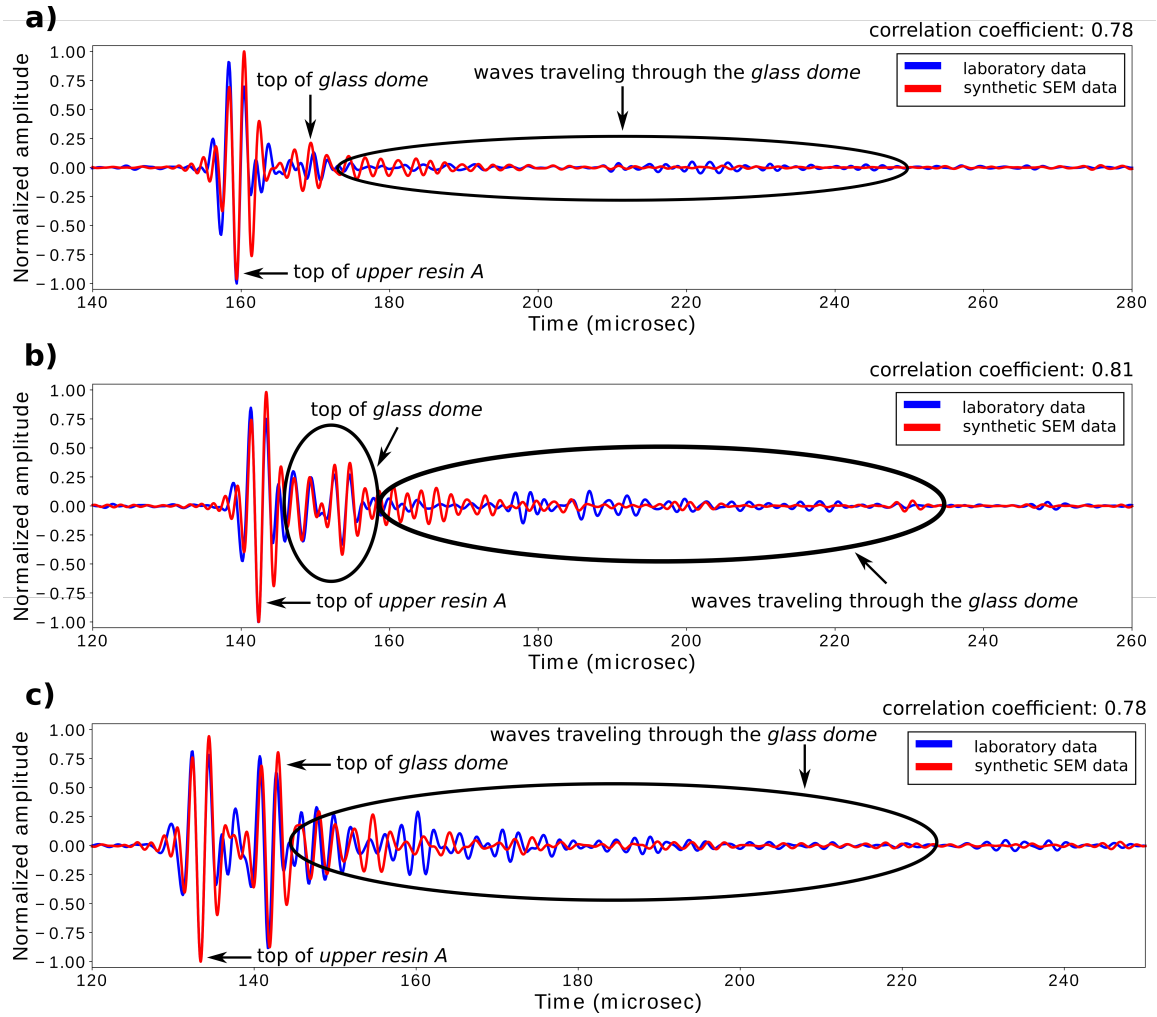

Figure 40. Comparison of offset laboratory traces with the corresponding synthetic SEM results: a) trace L, b) trace M, c) trace N.

3.3 Discussion

As shown above, we can accurately reconstruct the laboratory measurements for the WAVES model, using the SEM with a regular grid. In general, a good fit can be obtained between the laboratory zero-offset measurements and the numerical simulations. This is highlighted by the very-high correlation coefficients of at least 0.82 between the measured and simulated traces. Although the observed misfits are somewhat higher in the offset configuration, the correlation coefficients still suggest a good reconstruction of the laboratory offset traces as well, being at least 0.78.

There are several factors possibly contributing to the observed misfits:

- the fit may not be perfect due to the nature of the physical data sets, as pointed out in Part 1 (e.g., noise recorded in the laboratory and lower signal-to-noise ratio in the offset configuration),

- the numerical implementation of the source transducer is not perfect, as also pointed out in Part 1,

- although the precision of the laboratory measurements and the experimental data sets has been significantly improved for Part 2, there is still uncertainty in the transducer positions and in the tilt angle of the source,

- the model geometry is implemented in the numerical simulations with an equidistant grid. Such a grid cannot explicitly honor the discontinuities of the model. In the WAVES model, it concerns mainly the sides of the dome, especially the junctions of the different sedimentary layer boundaries next to the flanks of the dome. Considering the usually good fit in both zero-offset and offset configurations for the reflections from the curved top surface of the *glass dome*, we have a reassuring feedback on the current implementation of the geometry. Therefore we consider this effect to be minimal if any,

- we did a numerical calibration of the material properties for this multi-layered model. Although this procedure yields an excellent fit between the corresponding reference laboratory and synthetic traces, the obtained material properties are influenced by the illuminated zone of the model. That is, the calibrated properties are rather apparent than absolute, as they somewhat depend on the height and the horizontal position of the transducers,

- the *resins* used in the model have a high attenuation, resulting in low amplitudes of the late arrivals already for the laboratory traces. Therefore the relatively low simulated amplitudes of these late arrivals (traces J-M in Figures 39 and 40) can also be the result of uncertainties during the laboratory experiments,

- we note that the reflections from the top and bottom of the *aluminum* often show a high misfit in both arrival times and amplitudes, even in the zero-offset configuration. This misfit depends on the actual position of the measurements, as they are excellently reconstructed, for example, on trace H, but with a significant misfit on traces F and G. Because the earlier events usually show much less misfit on the same traces, at first it may appear surprising that the two perfectly horizontal interfaces of the *aluminum* provide the most difficulties for the simulations. Indeed, the coupling of the *aluminum* on both the top and the bottom were challenging. Namely, the coupling of *resin C* and the *aluminum* was challenging during the manufacturing of the physical model. The model is placed on sand to avoid any movement of the model during the measurements, therefore the coupling between the imperfectly compacted sand and the *aluminum* can also vary with the position.

Regarding the necessary computational resources, we used Intel Xeon Sandy Bridge EP (E5-2690) processors for the simulations. The computational cost was 1500 core hours to simulate 350 μs of wave propagation (corresponding to 7 s at seismic scale).

PART 2

Chapter 4
Reverse-time migration using the laboratory data - an example of using seismic imaging techniques to retrieve the geometry of the WAVES model

Seismic data is always recorded in the time domain, and as shown in Parts 1 and 2, the visualization of a seismic data set directly in the time domain does not show the real geometry of the subsurface. Therefore restoring the correct geometry is crucial before the interpretation of the measured data sets, in particular for complex geometries. For instance, as presented in Section 1.2, the interpretation of the laboratory offset data set for the WAVES model without the necessary post-processing is challenging. Then, in Section 3.2 we compared laboratory measurements with synthetic results in offset configuration, and the arrivals corresponding to complex ray paths could not be individually interpreted, due to the complex model geometry (Figure 28). Figure 41 illustrates the role of seismic data migration. After recording zero-offset data above a syncline (Figure 41 top), we can obtain the time-domain representation of the subsurface as shown in Figure 41 middle. This bow tie form clearly does not represent the real geometry, therefore a migration algorithm must be applied to the recorded data set to reconstruct the real geologic setup (Figure 41 bottom). This simple example already highlights the necessity of seismic data migration in exploration geophysics, which is even more important for a model with a complex geometry such as the WAVES model. In this case, there is definitely a strong need to apply some kind of post-processing, such as seismic migration, to reconstruct the geometry of the WAVES model using the experimental data.

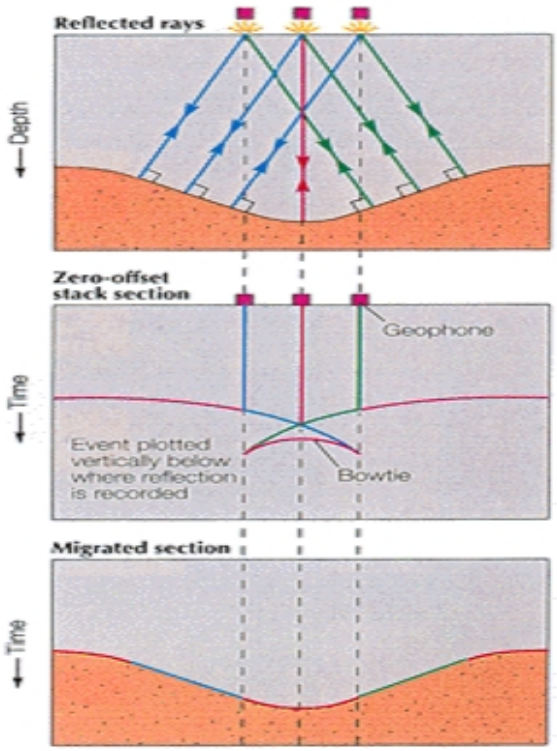

Figure 41. Illustration of the goal of seismic migration: acquisition geometry of a zero-offset data set above a syncline (top), the measured zero-offset image of the syncline in the time domain (middle), and the migrated data set in depth, representing the real geometry shown in the top image (bottom) (Courtesy of Schlumberger Oilfield Glossary, 2018).

Depending on the vertical and lateral heterogeneities, and the expected maximal tilt angle of the discontinuities, different migration algorithms have been developed (see e.g. Yilmaz, 1987). In this thesis, we use one of the most common seismic imaging techniques, the reverse-time migration (RTM). The RTM is based on the imaging principle (Claerbout, 1971), and it is capable to reconstruct the reflectors related to reflection coefficient contrasts, but it cannot determine the real amplitude of these reflectors (Zhang et al., 2003). Our main goal with applying the RTM to the laboratory data sets measured for the WAVES model is to validate the whole framework introduced in Part 1 and improved and adapted to the WAVES model in Part 2. Because the RTM yields a data set in the depth domain, if our framework is correct overall (including the laboratory measurements, the characterization of the material properties, and the numerical implementation of the transducer characteristics and the model geometry), the resulting RTM data set should fit perfectly the known geometry of the model.

4.1 Brief description of the method

The RTM is based on seismic reciprocity, which exploits the time-invariant property of the wave equation for a non-attenuating medium. Namely, this property makes it possible to record a wavefield in the time domain, and then focus back the wavefield at the source position by propagating back in time the registration at the original receiver position (in a last in-first out manner). In the context of time-reversal acoustics, seismic reciprocity was first used by Baysal et al. (1983) and later by Fink (1999).

The workflow of the applied RTM is shown in Figure 42. First, offset laboratory data is collected along the center line of the model in the x-direction (dashed line in Figure 28 middle left, and along the section shown in Figure 28 bottom left). We use three source tilt angles (19.7±0.1°, 25.1±0.1°, and 30±0.1°) and record multiple acquisition lines with a source spacing of 20±0.005 mm and a receiver spacing of 0.5±0.005 mm. These values correspond to a source spacing of 400±0.1 m and a receiver spacing of 10±0.1 m at seismic scale. Altogether 17 642 registrations on 42 survey lines are measured. Second, forward simulations are computed, using the same acquisition geometry as for the laboratory measurements. We conduct the simulations with the 2D version of the Specfem software package (Section 2.3 in Part 1) to save computational cost. Following the forward simulations, the differences of the recorded and simulated registrations are computed for each receiver. These differences provide the source time function of the so-called adjoint wavefield in the third step (e.g., Tromp et al., 2005, Virieux and Operto, 2009). The third step consists of two simulations at the same time, a forward simulation (identical to the second step) and the adjoint simulation, which means the forward propagation of the adjoint wavefield in time from the original receiver points of steps 1 and 2.

PART 2

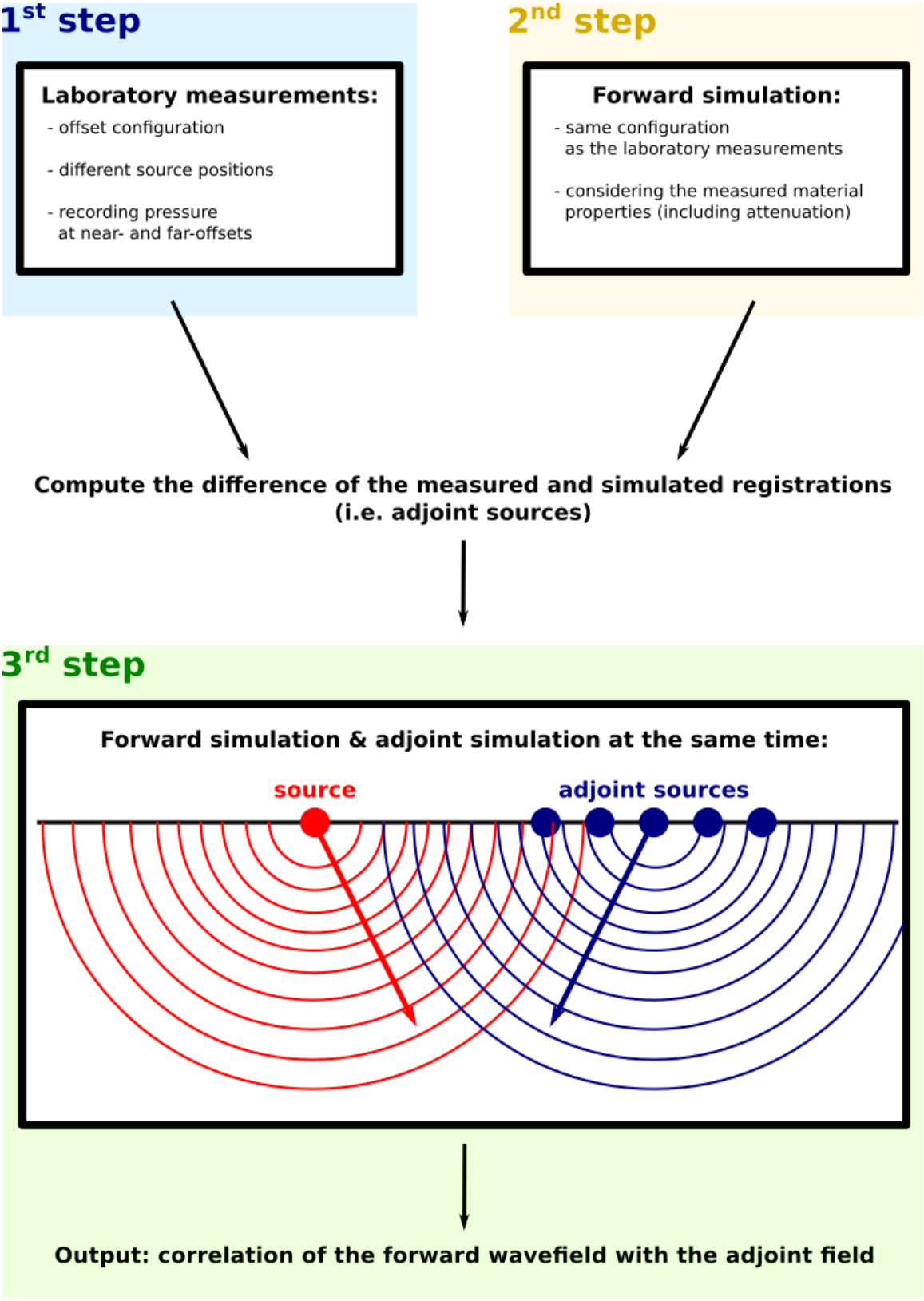

Figure 42. Workflow of the RTM.

The first idea, straightforward but clumsy and inappropriate, could be to use the "real"[4] model geometry and material properties for the forward and adjoint simulations of the RTM, as this would certainly make difficult the interpretation of the RTM results. Figure 43 top shows a 3D laboratory trace and the corresponding numerical trace simulated in 2D, using the "real" geometry and material properties. The source was positioned at x=19.995±0.5 mm, in the center line in y-direction, and 100±0.5 mm above the model. The receiver was located at x=79.830±0.5 mm, in the center line in y-direction, and 100±0.5 mm above the model. Similar to Section 2.3, the simulation can clearly reconstruct the reflections from the different discontinuities, however the simulated amplitudes are often higher than the measured ones and there are arrival time misfits as well, especially after 260 μs. If we took the difference of the measured and simulated traces, we would obtain the adjoint trace in Figure 43 bottom. Comparing Figure 43 top and bottom, we can see that the adjoint trace contains information mostly about the numerical simulation due to the systematically high amplitude of the simulated reflections. That is, we would certainly obtain high correlation values between the forward and adjoint wavefields, but the interpretation of the results would not be straightforward as the high correlation values would be (mostly) the result of the numerical implementation of the "real" geometry and material properties, and our main goal to validate the framework could not be achieved.

4 Here, "real" does not mean "exact", as there are (very) small differences (less than 0.1 mm) in the position of each interface of the model compared to those in the original 3D geometry files which were provided to the manufacturers of the physical model.

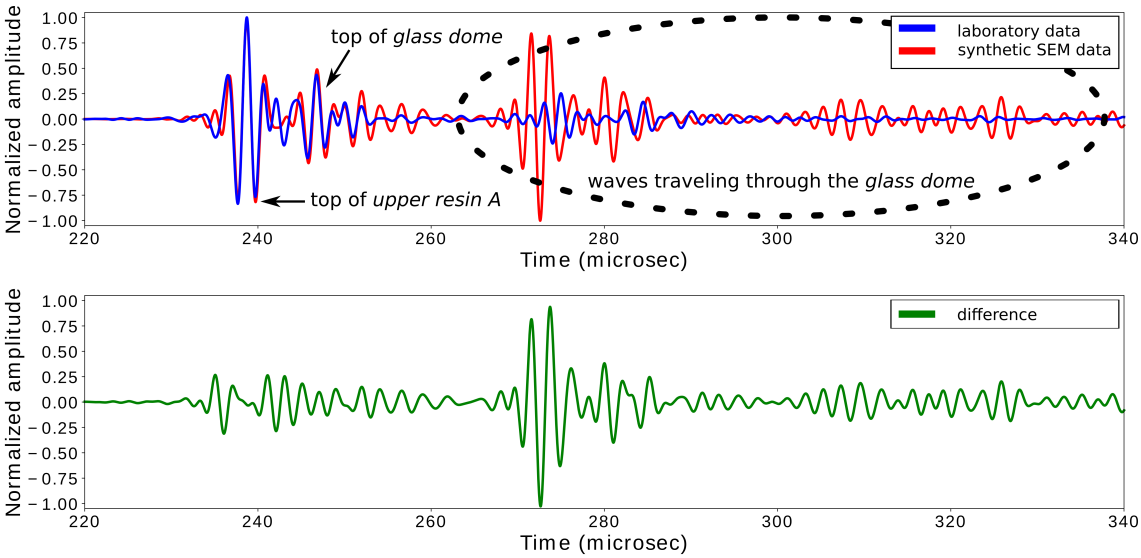

Figure 43. Illustration of the RTM calculations for the "real" model geometry and material properties. Top: laboratory trace (blue) and 2D simulated trace (red), bottom: difference (i.e. adjoint source).

We use a smoothed version of the "real" model instead, as that is the general practice in seismic exploration. Namely, a Gaussian filter with a kernel size of 12x12 mm is applied to each material property (V_P, V_S, ρ, Q_P, Q_S) to obtain a smooth model (Figure 44). Figure 45 top shows a 3D laboratory trace and the corresponding 2D simulated trace using the smoothed geometry, for the same source and receiver positions as for Figure 43. Compared to Figure 43, the simulated trace does not contain high-amplitude reflections from the model discontinuities as the model is smoothed in this case. Therefore, if the difference between the measured and simulated traces is computed, the adjoint trace in Figure 45 bottom preserves the information of the laboratory measurements. This way the interpretation of the final RTM results is straightforward, as any high correlation value corresponds to the information on the geometry that has been measured during the laboratory experiments.

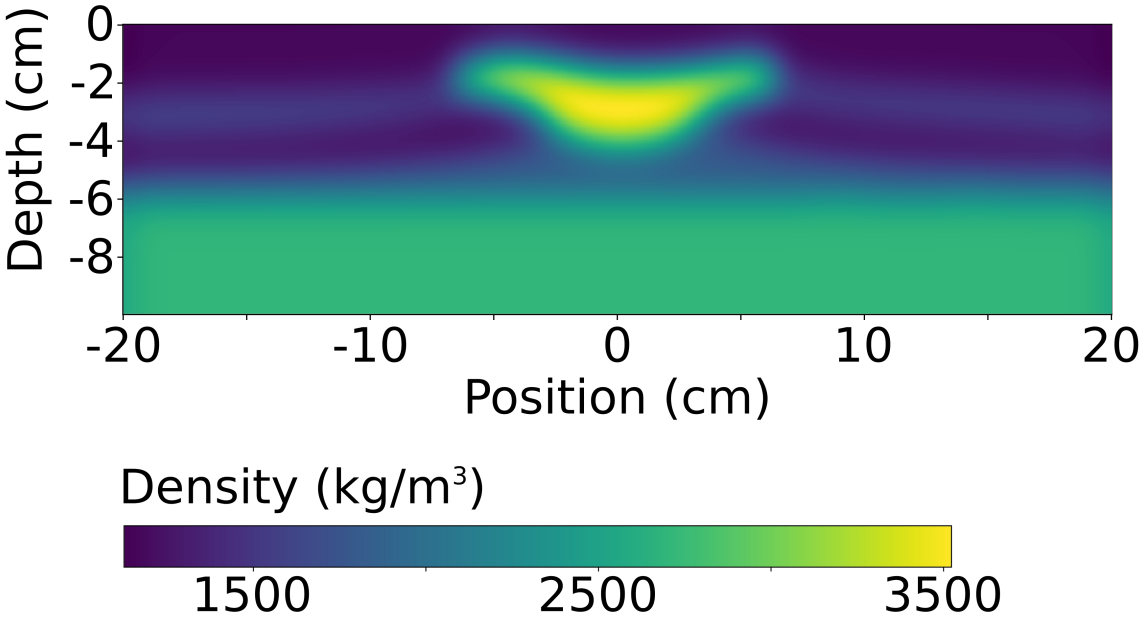

Figure 44. The smoothed density model used for the RTM calculations.

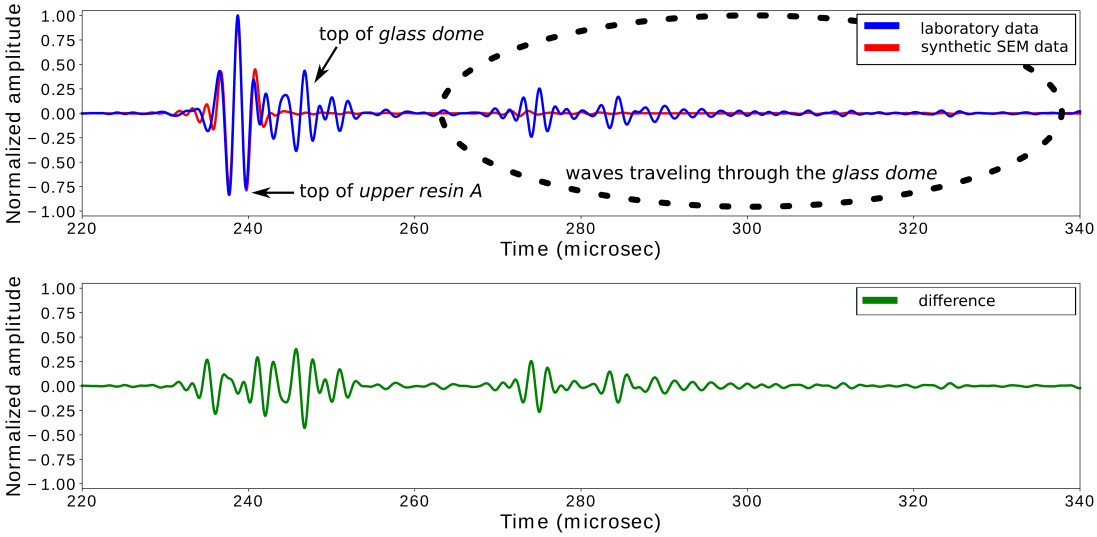

Figure 45. Illustration of the RTM calculations for the smoothed model, as shown in Figure 44. Top: laboratory trace (blue) and 2D simulated trace (red), bottom: difference (i.e. adjoint source).

Because the *resin* layers of the model have significant attenuation, it has to be considered during the calculations. We use the technique of *parsimonious disk storage* (aka *optimal checkpointing*) of the forward wavefield (Komatitsch et al., 2016). As part of this strategy, the so-called *checkpoint/restart files* are saved to the disk during the forward simulation in step 2. These files contain the displacement components and are typically stored for every few hundred time steps. Then in the

third step, the forward simulation is not run backward in time which would be numerically unstable, but rather forward, using the checkpoint/restart files. At any time, the simulation is run forward in time using the corresponding restart file, read back from the disk. Because the simulations are always conducted forward in time, they are always stable, even in the case of attenuating materials. The process is also exact as there is no filtering involved as opposed to, for example, Ammari et al. (2013).

In classical RTM the correlation of the forward and adjoint wavefields is calculated in the third step (Figure 42). However, there is a strong connection between full-waveform inversion (FWI) and the RTM (e.g. Tromp et al., 2005), therefore, sensitivity kernels can be defined also for the RTM and used similar to the FWI for the imaging and geologic interpretation of the subsurface (e.g., Virieux and Operto, 2009, Zhu et al., 2009). In this case, some derivatives of the cross-correlated wavefields are used. These derivatives (aka *sensitivity kernels*) depend on the formulation of the wave equation. We note that in practice, there is no one formulation to be chosen in any case, but rather it depends on the actual geologic setup and the recorded data itself (e.g., seismic exploration, global seismology etc.) (e.g. Zhu et al., 2009). Thus usually different formulations are computed and it requires an extensive knowledge and experience to choose the data set(s) to be interpreted with the most geological/geophysical relevance. We calculate the two most common formulations in this thesis, first the density ρ, bulk modulus κ, shear modulus μ formulation, then, the impedance ρ', compressional-wave speed α, shear-wave speed β formulation. An extensive explanation of the calculations can be found, for example, in Liu and Tromp (2006), Tromp et al. (2008), Zhu et al. (2009), Douma et al. (2010), and Luo et al. (2013). Here we present only the sensitivity kernels which are used in this thesis:

$$K_\rho(\boldsymbol{x}) = \int_0^T \rho(\boldsymbol{x})\,\partial_t \boldsymbol{s}^*(\boldsymbol{x}, T-t)\cdot\partial_t \boldsymbol{s}(\boldsymbol{x}, t)\,dt \quad , (25)$$

$$K_\kappa(\boldsymbol{x}) = -\int_0^T \kappa(\boldsymbol{x})[\nabla\cdot\boldsymbol{s}^*(\boldsymbol{x}, T-t)][\nabla\cdot\boldsymbol{s}(\boldsymbol{x}, t)]\,dt \quad , (26)$$

and

$$K_\mu(\boldsymbol{x}) = -\int_0^T 2\mu(\boldsymbol{x})\boldsymbol{D}^*(\boldsymbol{x}, T-t):\boldsymbol{D}(\boldsymbol{x}, t)\,dt \quad , (27)$$

namely, the density K_ρ, bulk modulus K_κ, and shear modulus K_μ kernels, respectively, where $\boldsymbol{x}$ is the spatial coordinate, the integral is over the time ($t = 0 \,..T$), $\boldsymbol{s}$ is the displacement, $\boldsymbol{s^*}$ is the adjoint source, $\boldsymbol{D} = \frac{1}{2}[\nabla \boldsymbol{s} + (\nabla \boldsymbol{s})^T] - \frac{1}{3}(\nabla \cdot \boldsymbol{s})\boldsymbol{I}$ and $\boldsymbol{D^*}$ are the traceless strain deviator and its adjoint, respectively (Tromp et al., 2005), and $\boldsymbol{I}$ is the identity matrix. The definition of the second set of sensitivity kernels are based on equations 25-27:

$$K_{\rho'} = K_\rho + K_\kappa + K_\mu \quad , (28)$$

$$K_\alpha = 2K_\kappa\left(1 + \frac{4}{3}\frac{\mu}{\kappa}\right) \quad , (29)$$

and

$$K_\beta = 2\left(K_\mu - \frac{4}{3}\frac{\mu}{\kappa}K_\kappa\right) \quad (30)$$

for the impedance $K_{\rho'}$, compressional-wave speed K_α, and shear-wave speed K_β kernels, respectively.

4.2 RTM results

Figure 46 shows the resulting sensitivity kernels obtained with the RTM. From the three kernels of the K_ρ-K_κ-K_μ formulation, K_κ seems to provide the most easily interpretable image (Figure 46b). Although this kernel shows artifacts as well, the different discontinuities of the model can be interpreted easier than for K_ρ or K_μ. As pointed out by Zhu et al. (2009), RTM images usually suffer from artifacts, due to diving waves, head waves, and backscattered waves. They suggest to rely on the impedance kernel $K_{\rho'}$, as that is the sum of K_ρ, K_κ, and K_μ (Equation 28), therefore the low-frequency artifacts cancel each other during the summation. This observation is confirmed for the WAVES model, as can be seen in Figure 46d. Considering either K_κ or $K_{\rho'}$, we can easily interpret the top of the physical model at a depth of zero cm. The other discontinuities of the model can also be interpreted, especially in the middle of the sections, where the model is more illuminated than towards the sides. Furthermore, there is a difference between the coherence of these discontinuities on the left and right sides of each section. That is because the source was always on the left side during the laboratory experiments, therefore the receiver could not image beyond the source position. Last but not least, we see a proper imaging of all sides of the glass dome, also on the bottom. The top of the aluminum at a depth of -5.5 cm can also be interpreted at its known position.

PART 2

In order to validate the resulting RTM images from the perspective of the spatial dimensions of the geometry, Figure 47 shows $K_{\rho'}$ superimposed to the color-coded known reference geometry. From a qualitative viewpoint, we can see an almost perfect fit between the sensitivity kernels and the original geometry for each domain of the model.

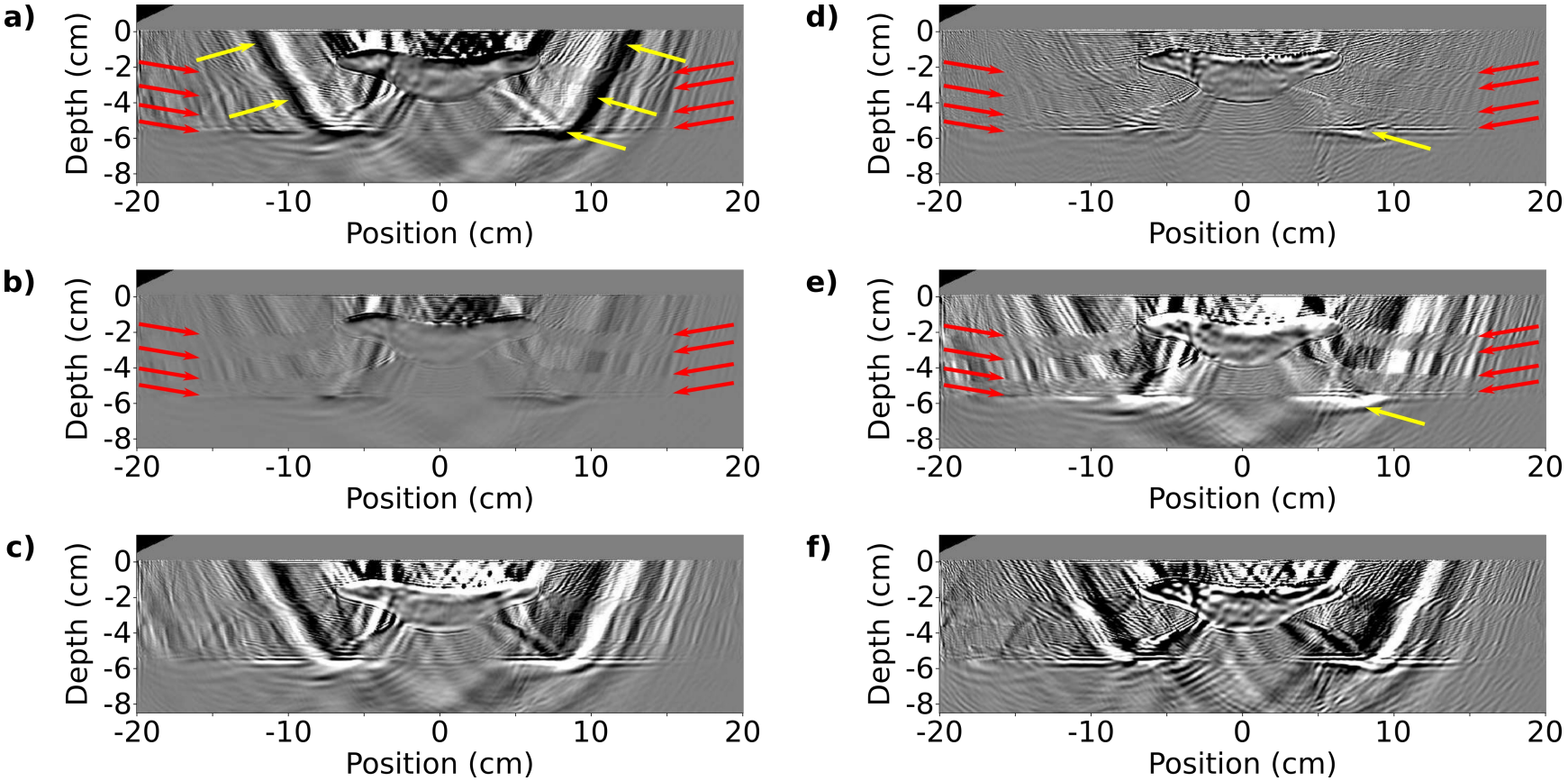

Figure 46. Sensitivity kernels obtained with the RTM: a) density kernel K_ρ, b) bulk modulus kernel K_κ, c) shear modulus kernel K_μ, d) impedance kernel $K_{\rho'}$, e) compressional-wave speed kernel K_α, and f) shear-wave speed kernel K_β. Yellow arrows: artifacts, red arrows: known model discontinuities.

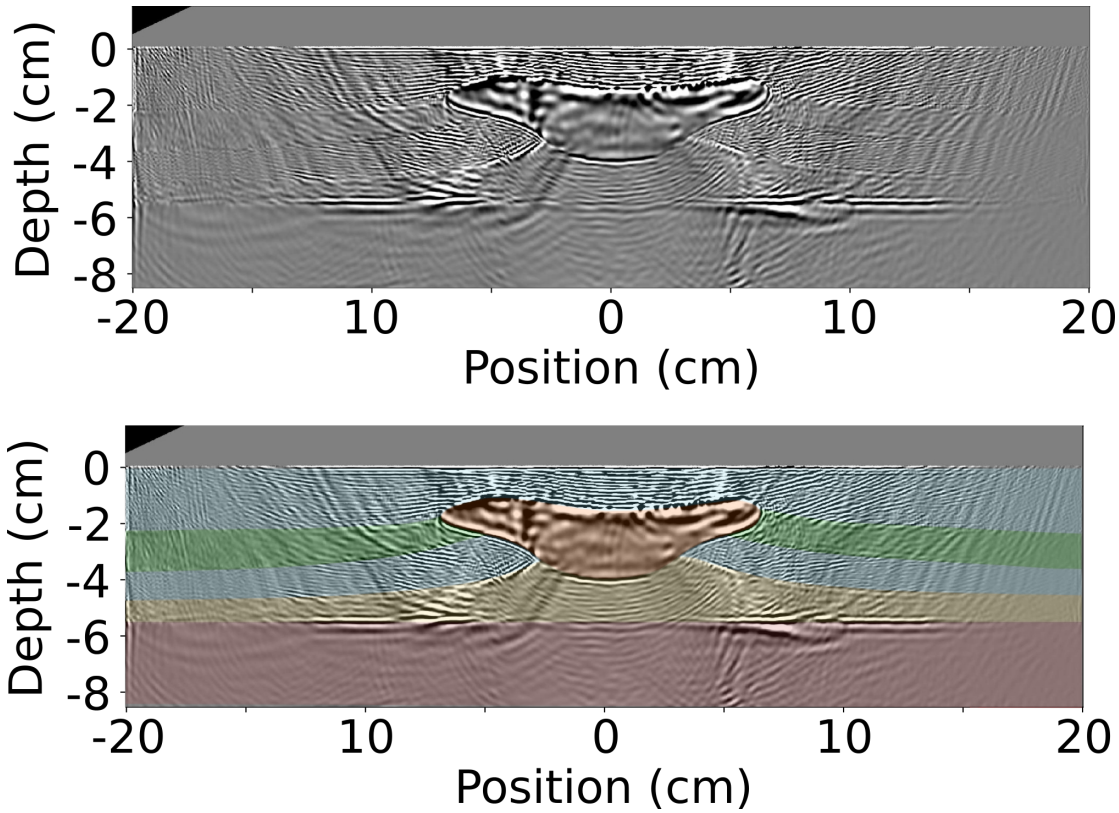

Figure 47. The impedance sensitivity kernel $K_{\rho'}$ obtained with the RTM. Top: the obtained kernel, bottom: the obtained kernel with an overlay of the original geometry (in color).

4.3 Discussion of the RTM results

As shown above, we can successfully reconstruct the original geometry of the WAVES model with a 2D RTM, using the 3D laboratory data sets. Density, bulk modulus, shear modulus, impedance, compressional-wave speed, and shear-wave speed kernels were calculated as part of the RTM. We found that the bulk modulus and the impedance kernels are the most suitable for the interpretation of these data sets. The known discontinuities of the model are almost all restored. The top surface of the physical model, as well as all sides of the glass dome, and the top of the aluminum are entirely recovered. The other discontinuities are well-reconstructed in the central positions, little less coherently at greater depths, or sometimes next to the dome. Artifacts can also be interpreted on the RTM images, which are partly normal with the RTM, due to diving waves, head waves, and backscattered waves. In accordance with the literature (e.g. Zhu et al., 2009), the impedance kernel suffers from fewer artifacts than for example the bulk modulus kernel.

Although the comparison of the RTM images with the original geometry shows an almost perfect overlap, we need to keep in mind the non-equivalence of the 2D and 3D for a complex geometry like the WAVES model. The RTM images could be improved by re-performing the RTM in 3D where sources and receivers were to be deployed out of the current acquisition plane, as well as by using more sources with a smaller source spacing.

PART 2

Conclusions of Part 2

The goal of Part 2 is to show that the framework, established in Part 1 to accurately implement the laboratory measurements for small-scale physical models in the numerical domain, can be successfully applied to the complex WAVES model as well. The model represents a realistic geologic setup, with a complex salt-dome in the middle (made of *glass*), surrounded by sedimentary layers (*resins*), and a crystalline basement (*aluminum*). The precision of the laboratory measurements has been significantly improved compared to Part 1. It concerns the accuracy of the lateral movement of the transducers and the tilt angle of the source transducer. We used the SEM to reconstruct the 3D zero-offset and 3D offset laboratory measurements. The numerical implementation is similar to Part 1, with the exception of the implementation of the model geometry. Because a conform 3D non-structured hexahedral mesh could not be obtained for the model, we resorted to an equidistant 3D grid. The same calibration is used for the multi-layered WAVES model as the procedure presented in Part 1. Because of the complex model geometry, first, the material properties of all the layers except the glass were calibrated for a reference trace. Then, a second trace in the center of the model was used to calibrate the properties of the glass too.

The comparison of the synthetic results with the laboratory measurements has revealed a very good fit for the arrival time, phase, and amplitude. The revealed minor amplitude mismatches may be attributed to the noise recorded in the laboratory data, as well as to the inaccuracy of the proposed source implementation to reconstruct the low-energy secondary lobes of the source transducer, and the uncertainties in the attenuation parameters chosen for the simulations. Furthermore, the initial concern that the grid representation of the model geometry may also contribute to the occasional arrival time and amplitude misfits is finally abandoned since there is a usually good fit in both zero-offset and offset configurations for the reflections from the curved top surface of the *glass dome*. Therefore we consider this effect to be minimal if any.

Following the comparison of the forward simulated traces with the laboratory measurements, we have presented some results of the 2D RTM using the laboratory data sets. Numerous data sets were recorded in the center line of the model for different source positions and source tilt angles. The sensitivity kernels have been computed with the help of a 2D RTM for a smoothed version of the known reference

model. The resulting RTM images show an accurate and coherent reconstruction of most of the 3D model discontinuities. A slightly less coherent image on the sides can be attributed to the lesser illumination of those regions. The RTM images also revealed some artifacts, which are partly usual with the RTM, while other artifacts are related to the modeling error. These misfits can be attributed to the same sources of misfits as for the forward simulations, as well as to the fact that the RTM was computed in 2D, while the model has a complex 3D geometry. Nevertheless, the almost perfect overlap between the RTM sensitivity kernels and the known model discontinuities provide a successful validation for the entire framework, including the laboratory measurements, the characterization of the material properties, and the numerical implementation of the transducer characteristics and the model geometry.

Based on the above-mentioned observations, we propose the following points to elaborate on the WAVES model:

- the long-term suggestions listed in Conclusions in Part 1 could significantly improve the accurate numerical reconstruction of the laboratory measurements for the WAVES model as well,
- although the accuracy of the lateral movement of the transducers has been significantly improved for the laboratory measurements, the absolute positioning inaccuracy should also be decreased. We note that it probably requires the help of metrologists,
- a 3D hexahedral non-structured mesh of the WAVES model could mitigate any possible effect of the current grid representation,
- the RTM should be re-calculated in 3D and using more sources with smaller source spacing to eliminate the artifacts related to the current 2D application.

GENERAL CONCLUSIONS

AND PERSPECTIVES

GENERAL CONCLUSIONS AND PERSPECTIVES

General conclusions

As presented in the General Introduction, there is a strong need to benchmark the numerical algorithms used in exploration geophysics with experimental data obtained for realistic small-scale models in laboratory conditions. However, such a comparison between laboratory and synthetic data requires a carefully chosen and jointly-adapted approach to both the laboratory experiments and the numerical modeling. On the one hand, the numerical tools must be adapted to the experimental configuration (e.g., implementing the real source characteristics, material properties, and acquisition conditions). On the other hand, the laboratory experiments have to be carried out keeping in mind the capabilities of the numerical tools (e.g. choosing the acquisition geometry such that the future computational cost will be the lowest possible). This highly challenging task is the goal of this PhD thesis. Thus, we have presented a framework, which at first reproduces offshore seismic measurements in laboratory conditions with the help of small-scale models, and then the numerical tools are adapted to the accurate synthetic reconstruction of the experiments.

We introduced the framework in Part 1, using the Marseille-Benchie model, which was designed to represent a moderately complex geometry. It contains various topographic features, such as a dome, a truncated smaller dome, a truncated pyramid and two flat parts separated by a ramp. This geometry ensures a complex wavefield, including reflections, diffractions, and multiples. The model is made of polyvinyl chloride (PVC), which was chosen because its material properties are considered to be close to those of the typical sedimentary layers. Because the model has only one layer and a flat bottom surface, the interpretation of the measurements is relatively straightforward. This moderately challenging geometry provides the necessary tool for the elaboration of the framework.

Prior to the finite-difference and spectral-element simulations, we have focused on the input data/parameters, such as the material properties, the model geometry, and the characteristics of the source and receiver transducers. The material properties have been characterized in the laboratory and calibrated for the numerical simulations. The viscoelastic behavior of the material used in the model has been approximated with a set of standard linear solids in the numerical simulations. The real source transducer characteristics have been implemented based on a new approach, which consists of the laboratory characterization of the impulse response of the transducer, followed by an inversion step to obtain a numerically equivalent source for the numerical

simulations. The zero-offset measurement requires an additional deconvolution step before the inversion because, in that case, only one transducer is used as the source and the receiver.

We have suggested an optimization of the spectral-element computational cost, by using larger elements in the non-structured mesh and higher order polynomial basis functions. This technique helps to significantly reduce the computational cost while obtaining a similar level of accuracy. Comparison of the zero-offset synthetic and laboratory results has revealed an excellent fit in terms of arrival time, phase, and amplitude, for both the SEM and the FDM. Minor amplitude mismatches may be attributed to the noise recorded in the laboratory data, as well as to the inaccuracy of the proposed source implementation to reconstruct the low-energy secondary lobes of the source transducer, and the uncertainties in the attenuation parameters chosen for the simulations.

Comparison of – both SEM and FDM – simulated and laboratory offset traces has exhibited a good fit in terms of amplitude, arrival time, and phase, but with significantly less accuracy for some arrivals than in the zero-offset case. This can be mainly attributed to the inaccuracies of the transducer positions during the laboratory measurements combined with the strong topography of the model, as well as to the smaller signal-to-noise ratio of the offset configuration.

Smaller misfits between the finite-difference and the spectral-element synthetic results may be attributed to the grid representation of the model geometry in the finite-difference simulations, which should be completely resolved with an even finer grid, but at a higher computational cost.

Based on these observations, we proposed some necessary near-term improvements of the framework. These include a more precise positioning of the transducers during the measurements and a more precise measurement of the tilt angle of the source transducer. Although these modifications took time, they were essential to obtain a better fit between the measurements and the simulations. Indeed, the precision of the lateral transducer movements and of the source tilt angle have been improved by a factor of 100 and 10, respectively.

Following these modifications, we extended the framework to the complex and multi-layered WAVES model in Part 2. The model represents a realistic geologic setup with a complex salt-dome in the middle (made of *glass*), surrounded by sedimentary layers

(*resins*) and a crystalline basement (*aluminum*). We used the SEM to reconstruct the 3D zero-offset and 3D offset laboratory measurements. The numerical implementation is similar to Part 1, with the exception of the implementation of the model geometry. Because a conform 3D non-structured hexahedral mesh could not be obtained for the model, we resorted to an equidistant 3D grid. The same calibration was used for the multi-layered WAVES model, as the procedure presented in Part 1. Because of the complex model geometry, first, the material properties of all the layers except the glass were calibrated for a reference trace. Then, a second trace in the center of the model was used to calibrate the properties of the glass too.

The comparison of the synthetic results with the laboratory measurements has revealed a very good fit for the arrival time, phase, and amplitude. The revealed minor amplitude mismatches may be attributed to the noise recorded in the laboratory data, as well as to the inaccuracy of the proposed source implementation to reconstruct the low-energy secondary lobes of the source transducer, and the uncertainties in the attenuation parameters chosen for the simulations. Furthermore, in theory, the grid representation of the model geometry could also contribute to the observed arrival time and amplitude misfits. However, we consider this effect to be minimal if any in this thesis, due to the usually good fit between the measured and simulated reflections from the curved top surface of the *glass dome*.

Following the comparison of the forward simulated traces with the laboratory measurements, we presented some results of the RTM using the laboratory data sets. Numerous data sets were recorded in the center line of the model for different source positions and source tilt angles. The sensitivity kernels have been computed with the help of a 2D RTM and a non-structured quadrangular mesh. The resulting RTM images show an accurate and coherent reconstruction of most of the model discontinuities. A slightly less coherent image on the sides can be attributed to the lesser illumination of those regions. The RTM images also revealed some artifacts, which are partly usual with the RTM, while other artifacts are related to the modeling error. These misfits can be attributed to the same sources of misfits as for the forward simulations, as well as to the fact that the RTM was computed in 2D, while the model has a complex 3D geometry. Nevertheless, the almost perfect overlap between the RTM sensitivity kernels and the real model discontinuities provide a successful validation for the entire framework, including the laboratory measurements, the characterization of the material properties, and the numerical implementation of the transducer characteristics and the model geometry.

GENERAL CONCLUSIONS AND PERSPECTIVES

Perspectives

The framework established in this thesis and the conclusions listed above open up the possibility of many future works. These can be divided into two categories: first, necessary long-term improvements of the framework to increase its precision and the follow-up of the work presented in this thesis for the Marseille-Benchie and the WAVES models; and second, using the proposed framework for other models and applications.

The long-term developments must be addressed to improve the overall accuracy of the framework. On the one hand, they concern the laboratory experiments, namely, decreasing further the uncertainties in the laboratory data sets by:

- most importantly increasing the precision of the absolute positioning of the transducers during the laboratory measurements,
- reconsidering the laboratory techniques used to characterize the properties of the material samples, especially for S-waves and for the attenuation parameters,
- assessing the noise level of the acquisition system and improving its signal-to-noise ratio,
- identifying the origin of the different noises measured temporarily or permanently in the laboratory.

On the other hand, the numerical modeling should also be improved by:

- mainly revisiting the proposed numerical implementation of the real transducer to account more for the low-energy secondary lobes and the low-energy late-arrivals of the source wavelet,
- reducing the man-hour cost of the SEM due to the lengthy meshing step, and elaborating a more automatic 3D hexahedral meshing algorithm which also yields an overall conform mesh.

As noted in the thesis, the Marseille-Benchie model has the advantage to yield a wavefield which is complex but more easily understandable than for example that of the WAVES model. Therefore the improvement of the precision of the framework should be verified also with the Marseille-Benchie model.

Re-performing the RTM in 3D for the WAVES model could eliminate any doubt about the possible artifacts present in the sensitivity kernels resulting from the difference between the 3D measurements and the 2D RTM. Should the 3D RTM results suffer

from much fewer artifacts than the presented 2D results, the inevitable need to perform RTM in 3D could be proven in general for seismic exploration.

Using the geologically realistic WAVES model and the framework presented in this thesis, other imaging techniques could also be tested. The framework provides a good benchmarking opportunity to test any newly developed imaging technique. For instance, a very interesting opportunity is to test the Marchenko imaging (e.g., Broggini et al., 2012, Wapenaar et al., 2014, van der Neut et al., 2015, Liu et al., 2017). Although the theoretical background of Marchenko imaging is well developed, there are still only a few works done where physical data sets are used to prove the practical abilities of the method (e.g. Becker et al., 2016, Ravasi et al., 2016). We note that the WAVES model is particularly challenging at the current state of the Marchenko imaging due to the high attenuation of the resin layers. As Evert (2016) noted, two-sided illumination is necessary in the case of a viscoelastic model. Moreover, currently reflected and transmitted wavefields must be recorded on both sides of the model. Should the Marchenko imaging be tested for the WAVES model, a further perspective is to test the effect of the acquisition geometry on the final results, especially in 3D.

We clearly see a high potential in using either the WAVES model or any other small-scale physical model to, for example, optimize the acquisition of field data sets before a complex seismic survey campaign. Although this thesis is focused on seismic applications, the presented framework can be used for other applications as well. As long as the underlying physics can be explained by the linear wave equation, the approach of the thesis can be used irrespectively from the frequency, e.g. in medical imaging using ultrasounds.

APPENDIX A

LABORATORY CHARACTERIZATION OF THE MATERIAL PROPERTIES

APPENDIX A

Marseille-Benchie model

As noted in Section 2.3.4 in Part 1, the material properties of the Marseille-Benchie model had to be characterized before the numerical simulations. The most important properties for seismic modeling are the density, the velocity, and the attenuation, and the velocity and attenuation parameters had to be characterized for both P- and S-waves. We use two samples from the same PVC block the model was built from. The two samples have different thickness, approximately 25 and 50 mm. Density can be determined by measuring the volume and the weight of the samples: 1440±10 kg/m3 (±0.7 %).

Because we are interested in the velocity and attenuation for the whole frequency range of interest (250-650 kHz), we used monochromatic sine waves at 50 kHz increments. The samples are placed between two transducers, one of which is the source, and the other one is the receiver. Transmitted waves are used, which are generated by a function generator (Figure A1). In order to characterize the velocity and the attenuation of the S-waves too, the samples are rotated to generate S-waves inside them. For P-wave measurements the samples are positioned normal to the transducers, that is the incidence angle θ is 0° (Figure A1).

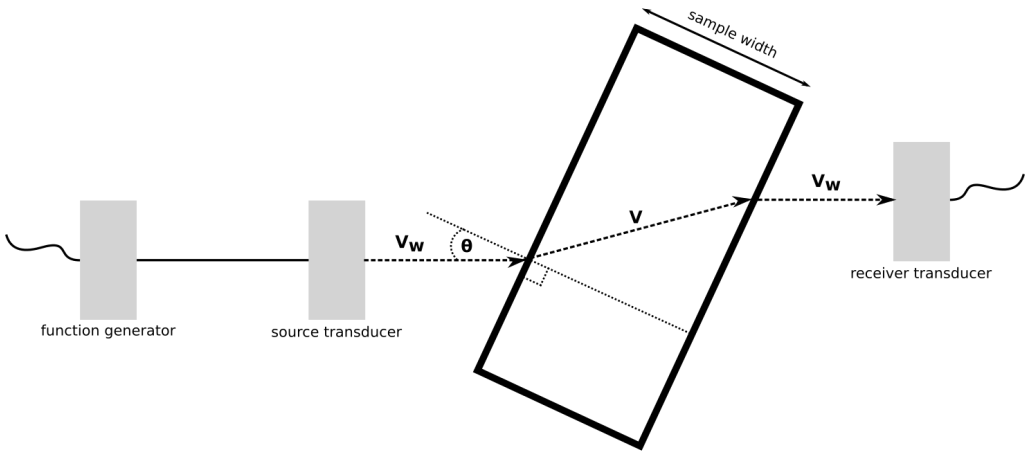

Figure A1. Schematic figure of the experimental setup to characterize the properties of the material samples. V_w and V denote the velocity of the ultrasonic waves in water and the sample, respectively, and θ is the incidence angle of the waves.

To determine the velocity of the waves propagating in the samples, we measure the arrival time of the transmitted waves through the two samples of different thickness.

APPENDIX A

Following Lasaygues and Pithioux (2002) and using the laboratory setup of Figure A1, the velocity of P- and S-waves can be determined:

$$V = \frac{V_w}{\sqrt{1 + \frac{V_w \Delta t}{e}\left(\frac{V_w \Delta t}{e} - 2\cos\theta\right)}} \quad , (A1)$$

where V is the P- or S-wave velocity in the sample, V_w is the velocity of sound waves in water, Δt is the difference in the arrival times through the two samples, e is the difference in the thickness of the two samples, and θ is the incidence angle. The amplitudes of the transmitted signals are measured to characterize the attenuation of the samples, and the attenuation α of either P- or S-waves can be calculated:

$$\alpha = \frac{\ln\left(A_2 / A_1\right)}{8.686\, e \cos\left(\theta\right)} \quad , (A2)$$

where α is calculated in dB/m, A_1 and A_2 denote the measured amplitudes for the thicker and the thinner samples, respectively (Figure A2).

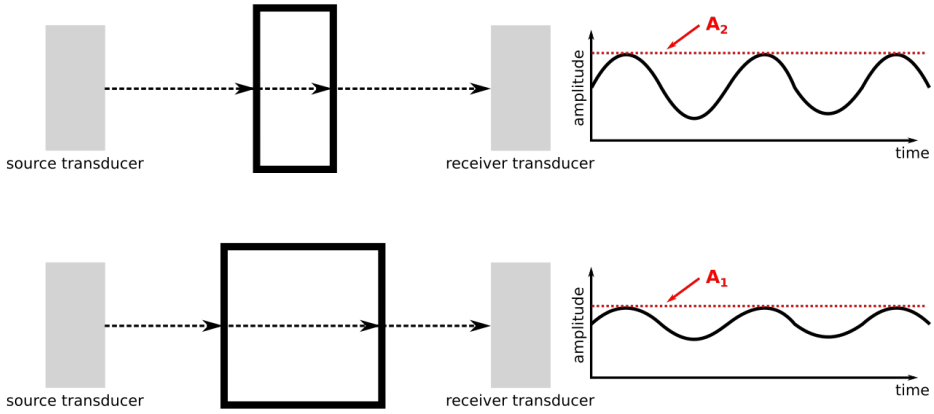

Figure A2. Illustration of the amplitudes measured through material samples of different thickness, using monochromatic sine waves. A_1 and A_2 denote the measured amplitudes through the thicker and thinner samples, respectively.

Figures A3 and A4 show the measured velocity and attenuation values (for both P- and S-waves), respectively. In each figure, vertical lines denote the assessed uncertainty of each measurement, and the maximal uncertainties are less than 0.1%, 47%, 0.4%, and 30% for V_P, V_S, α_P, and α_S, respectively. The significantly higher uncertainty for the S-waves is the result of their lower signal-to-noise ratios. This is the consequence of the higher intrinsic attenuation of S-waves, which is even more

pronounced due to their longer travel paths because of the acquisition setup (i.e. due to the rotated samples for S-wave characterization as shown in Figure A1). Moreover, the uncertainty of the incidence angle is significant for the S-waves, while that is negligible for the P-waves. Some measurements are not shown in Figures A3 and A4 due to their low reliabilities because of, for example, their low signal-to-noise or wavelength-to-sample width ratios, especially at low frequencies. Therefore these measurements are also omitted when the material properties for the whole frequency range of interest are calculated.

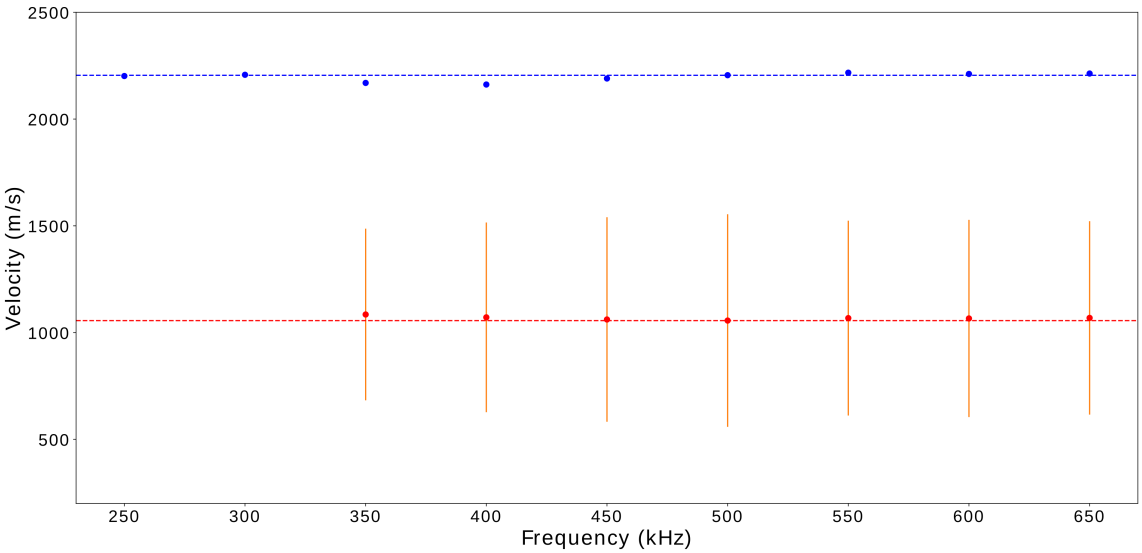

Figure A3. Measured velocity values for the PVC samples (dots) for P-waves (blue) and S-waves (red). The vertical lines show the assessed uncertainty of the measurements. The horizontal dashed lines show the value considered valid for the overall frequency range of interest (250-650 kHz).

APPENDIX A

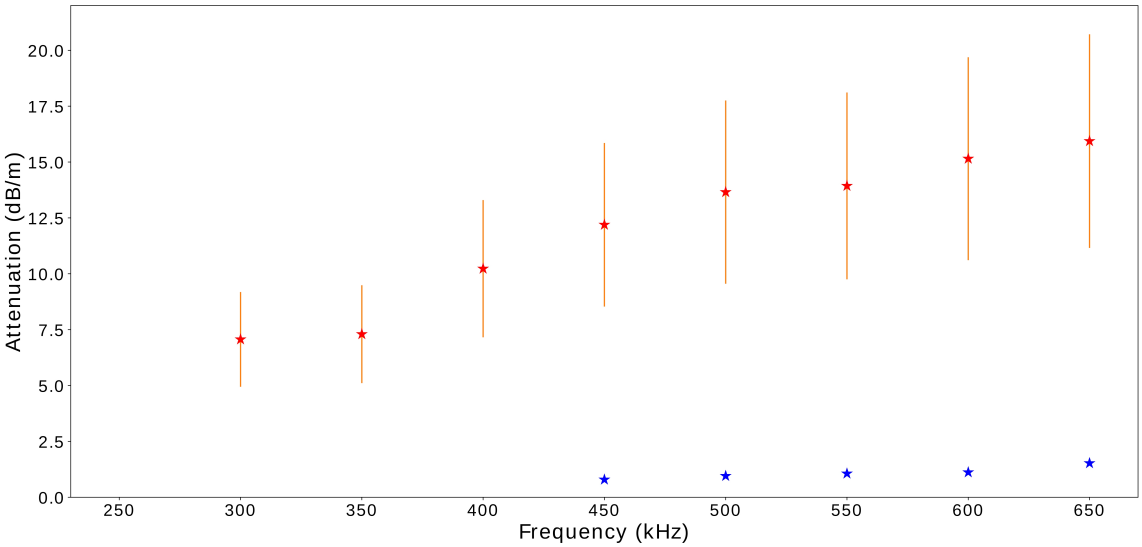

Figure A4. Measured attenuation for the PVC samples (stars) for P-waves (blue) and S-waves (red). The vertical lines show the assessed uncertainty of the measurements.

Because exploration geophysics, and therefore the numerical tools used in seismic exploration as well, rely on Q-factors instead of the direct attenuation values presented in Figure A4, we converted the measurements into the necessary Q_P and Q_S values:

$$Q = \frac{\pi f}{\alpha V} \quad , \text{(A3)}$$

where f denotes the frequency. Because the velocity (Equation A1) is necessary to convert attenuation values (Equation A2) into Q-factors, there is an accumulation of uncertainties in the obtained Q-factors. This is especially true for the S-waves, because of the already significant uncertainties in V_s. This is highlighted by the maximal uncertainties of 0.4% and 76% for Q_P and Q_S, respectively, which are much higher than those of the direct attenuation parameters above. Figure A5 shows the measured Q-factors for the PVC samples. We can see that although the attenuation values (Figure A4) vary with the frequency, the Q-factors are relatively constant for the frequency range of interest (Figure A5). The values considered to be valid for the overall frequency band are listed in Table 1.

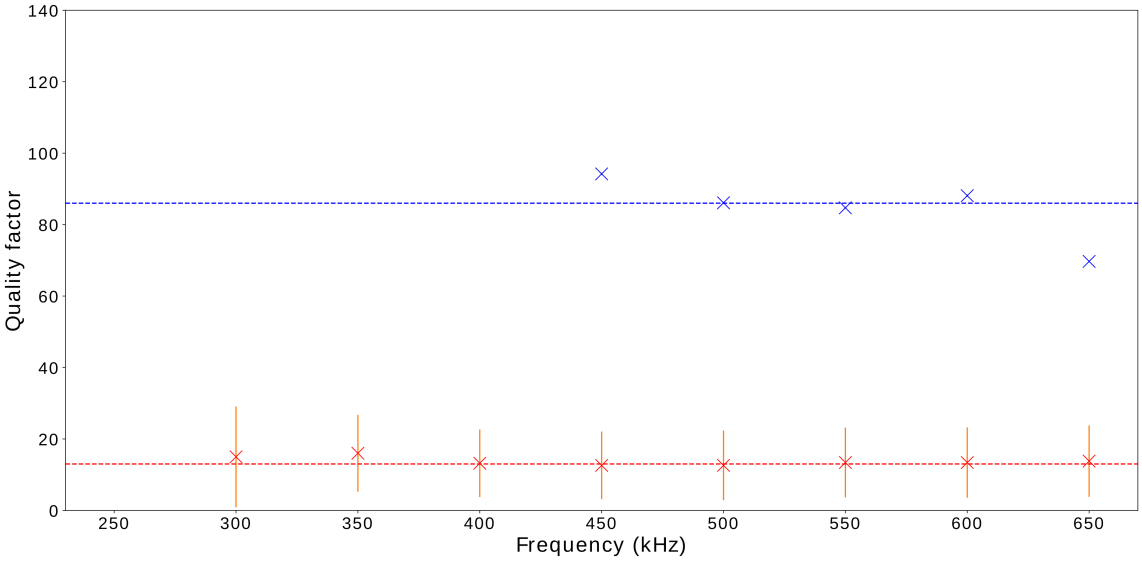

Figure A5. Measured Q-factors for the PVC samples (crosses) for P-waves (blue) and S-waves (red). The vertical lines show the assessed uncertainty of the measurements. The horizontal dashed lines show the value considered valid for the overall frequency range of interest (250-650 kHz).

APPENDIX A

WAVES model

The same techniques are used to characterize the material properties of each material used in the WAVES model. Table A1 shows the measured densities for each sample together with the associated uncertainties.

Material	Density (kg/m^3)
resin A	1172 ± 2 (± 0.17 %)
resin B	1680 ± 10 (± 0.60 %)
resin C	1800 ± 10 (± 0.56 %)
glass	3623 ± 10 (± 0.28 %)
aluminum	2710 ± 4 (± 0.15 %)

Table A1. Measured densities for each material used in the WAVES model and the associated uncertainties.

Similar to the Marseille-Benchie model, each measurement at each frequency was carefully analyzed, and based on, for example, the signal-to-noise ratio of the measurements or the wavelength-to-sample width ratio, we did not consider all the measurements at all the frequencies for the final assessment of the material properties. Figures A6 - A16 show the measured material properties and their associated uncertainties for *resin A*, *resin B*, *resin C*, *glass*, and *aluminum* samples, respectively. The maximal uncertainty of the measurements is shown in Table A1.

APPENDIX A

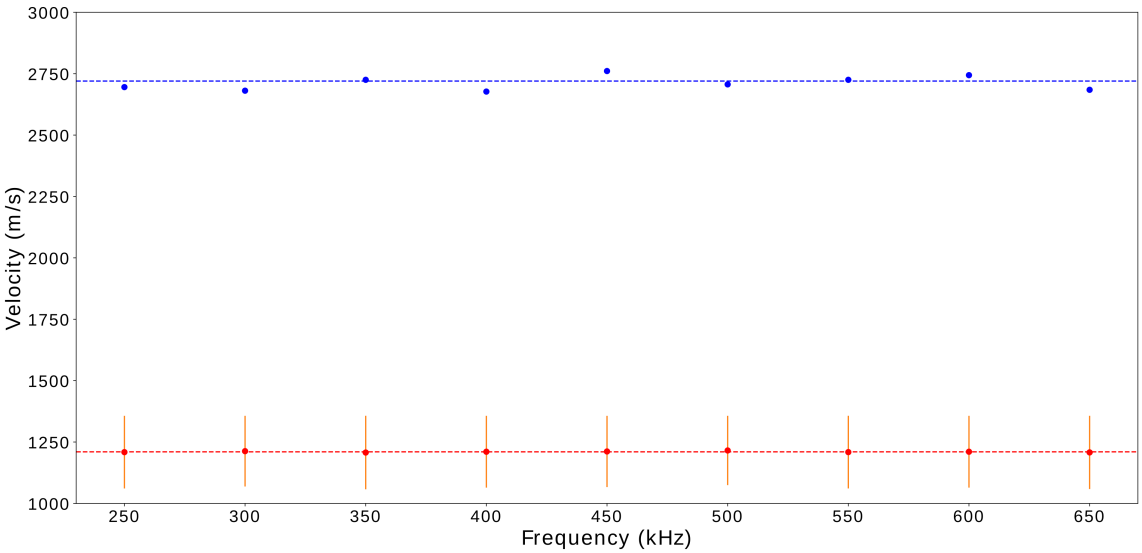

Figure A6. Measured velocity values for the *resin A* samples (dots) for P-waves (blue) and S-waves (red). The vertical lines show the assessed uncertainty of the measurements. The horizontal dashed lines show the value considered valid for the overall frequency range of interest (250-650 kHz).

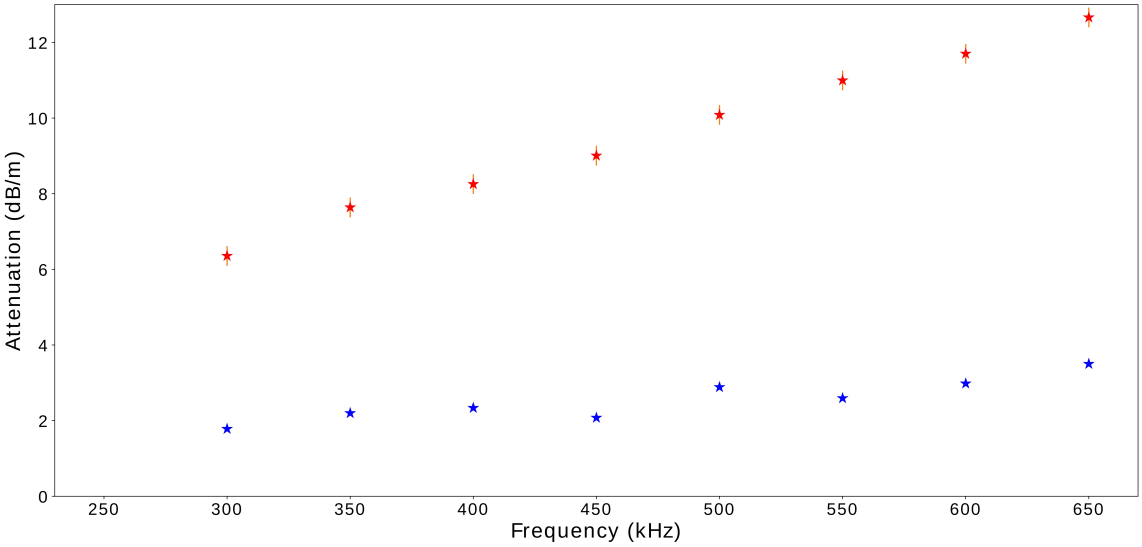

Figure A7. Measured attenuation for the *resin A* samples (stars) for P-waves (blue) and S-waves (red). The vertical lines show the assessed uncertainty of the measurements.

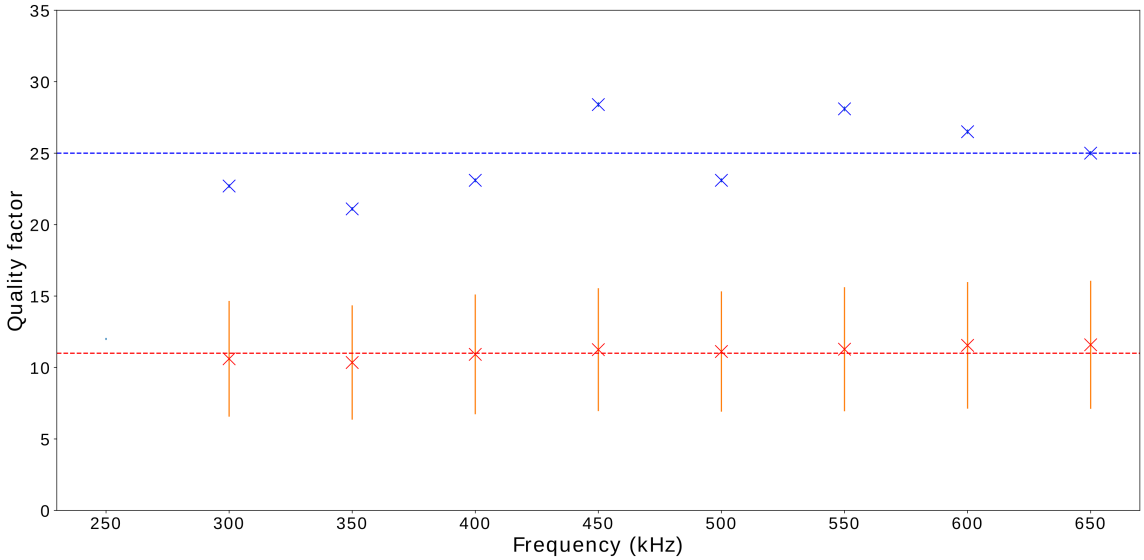

Figure A8. Measured Q-factors for the *resin A* samples (crosses) for P-waves (blue) and S-waves (red). The vertical lines show the assessed uncertainty of the measurements. The horizontal dashed lines show the value considered valid for the overall frequency range of interest (250-650 kHz).

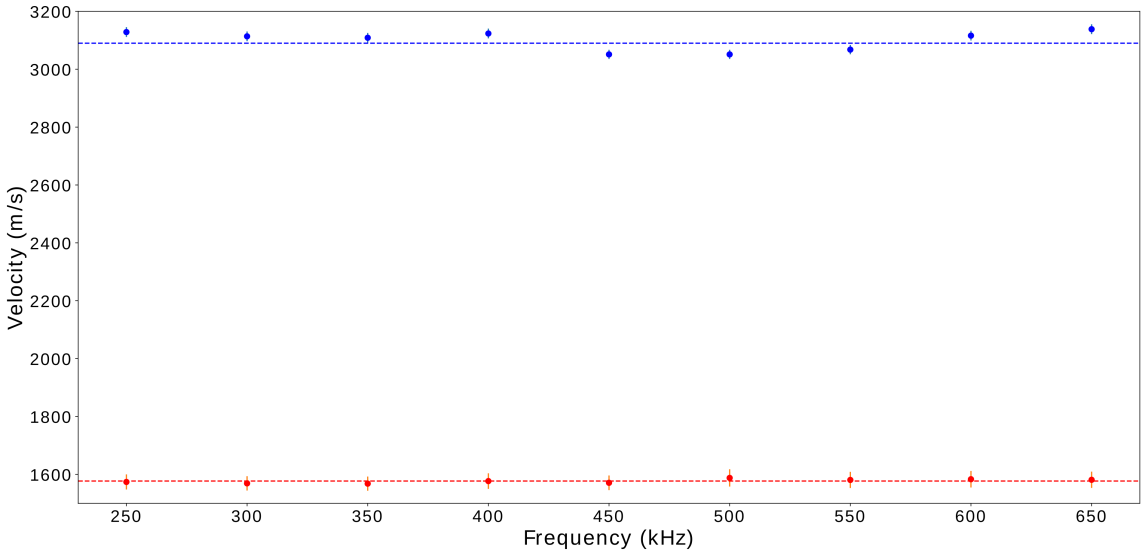

Figure A9. Measured velocity values for the *resin B* samples (dots) for P-waves (blue) and S-waves (red). The vertical lines show the assessed uncertainty of the measurements. The horizontal dashed lines show the value considered valid for the overall frequency range of interest (250-650 kHz).

APPENDIX A

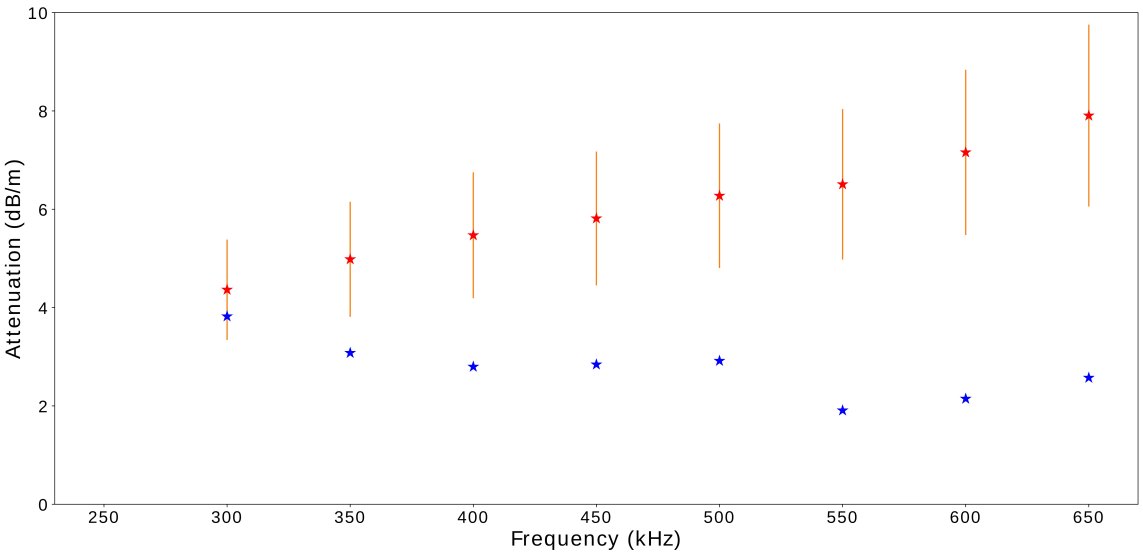

Figure A10. Measured attenuation for the *resin B* samples (stars) for P-waves (blue) and S-waves (red). The vertical lines show the assessed uncertainty of the measurements.

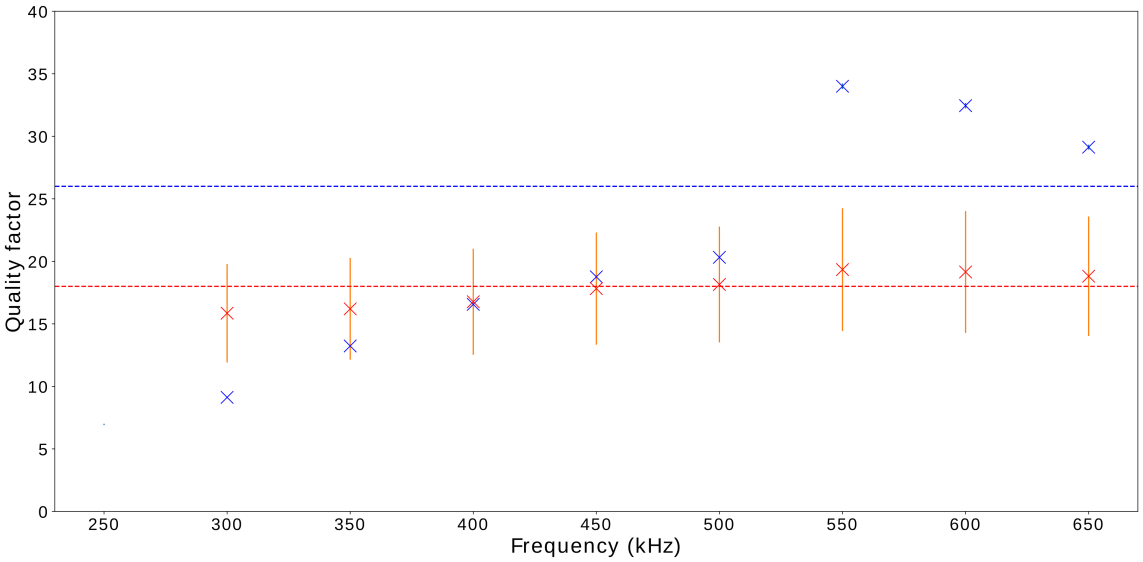

Figure A11. Measured Q-factors for the *resin B* samples (crosses) for P-waves (blue) and S-waves (red). The vertical lines show the assessed uncertainty of the measurements. The horizontal dashed lines show the value considered valid for the overall frequency range of interest (250-650 kHz).

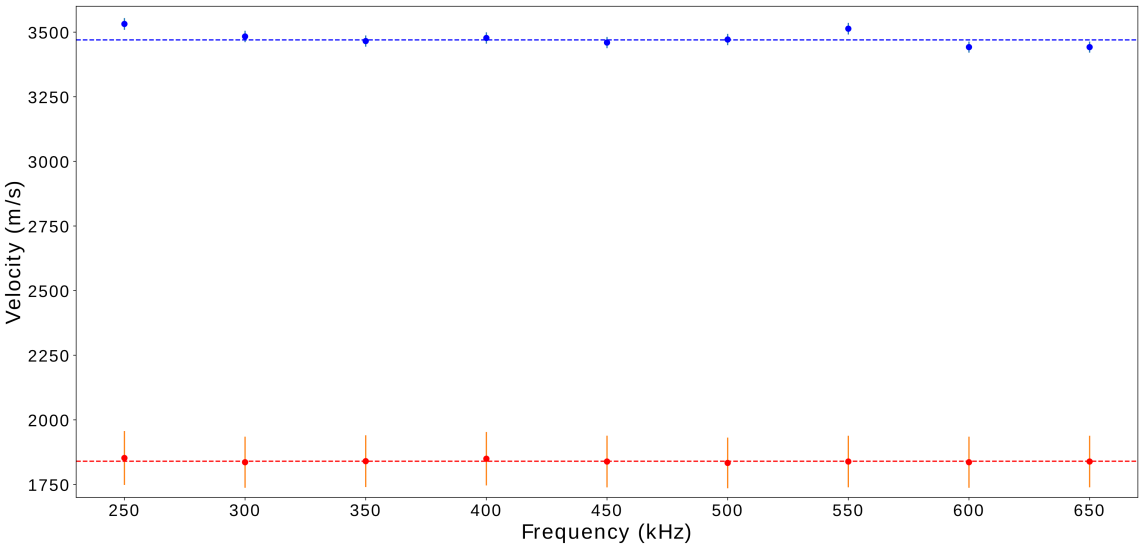

Figure A12. Measured velocity values for the *resin C* samples (dots) for P-waves (blue) and S-waves (red). The vertical lines show the assessed uncertainty of the measurements. The horizontal dashed lines show the value considered valid for the overall frequency range of interest (250-650 kHz).

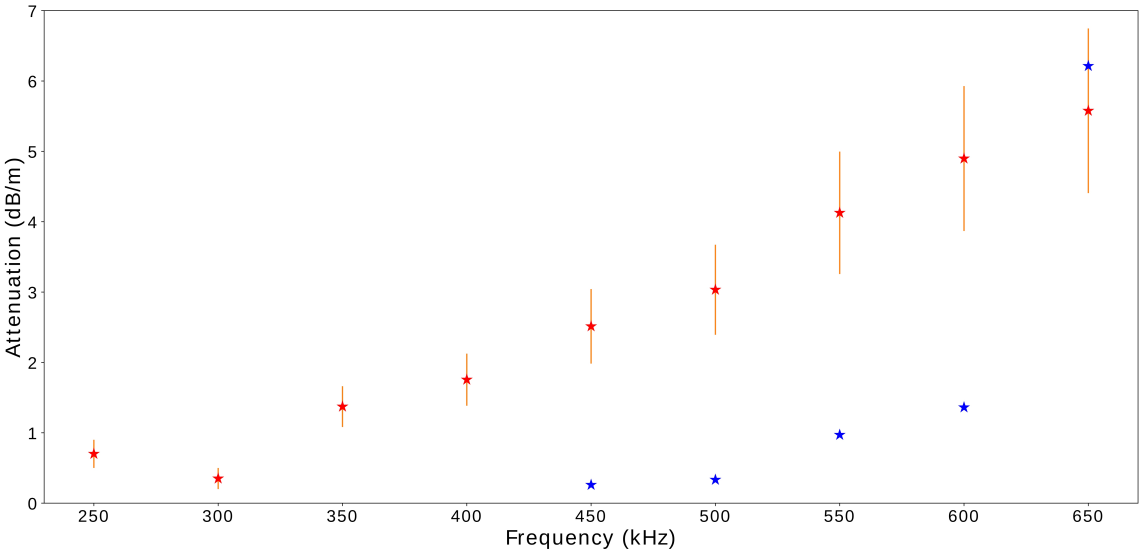

Figure A13. Measured attenuation for the *resin C* samples (stars) for P-waves (blue) and S-waves (red). The vertical lines show the assessed uncertainty of the measurements.

APPENDIX A

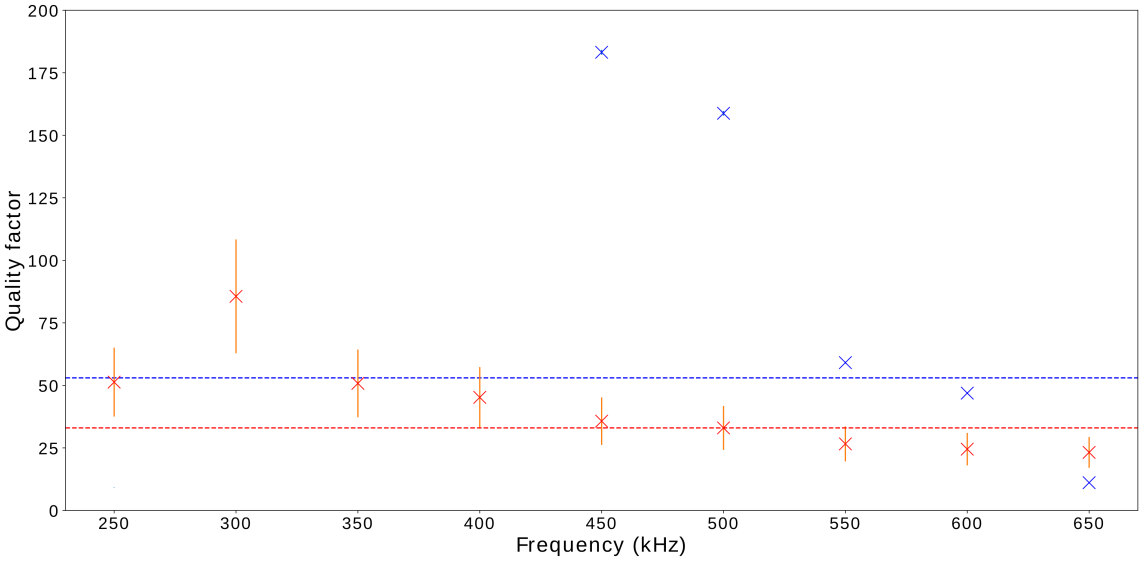

Figure A14. Measured Q-factors for the *resin C* samples (crosses) for P-waves (blue) and S-waves (red). The vertical lines show the assessed uncertainty of the measurements. The horizontal dashed lines show the value considered valid for the overall frequency range of interest (250-650 kHz).

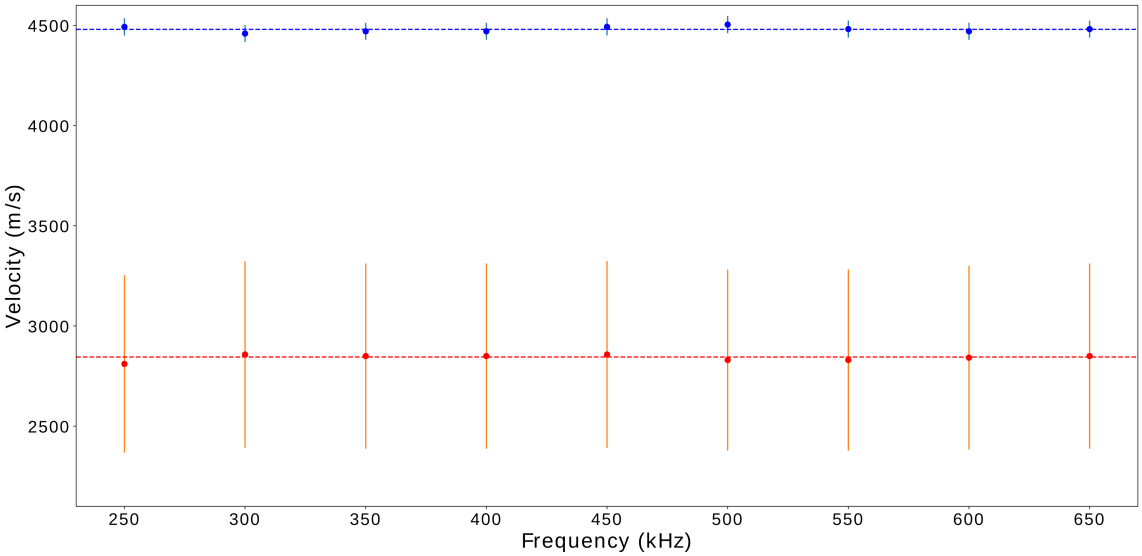

Figure A15. Measured velocity values for the *glass* samples (dots) for P-waves (blue) and S-waves (red). The vertical lines show the assessed uncertainty of the measurements. The horizontal dashed lines show the value considered valid for the overall frequency range of interest (250-650 kHz).

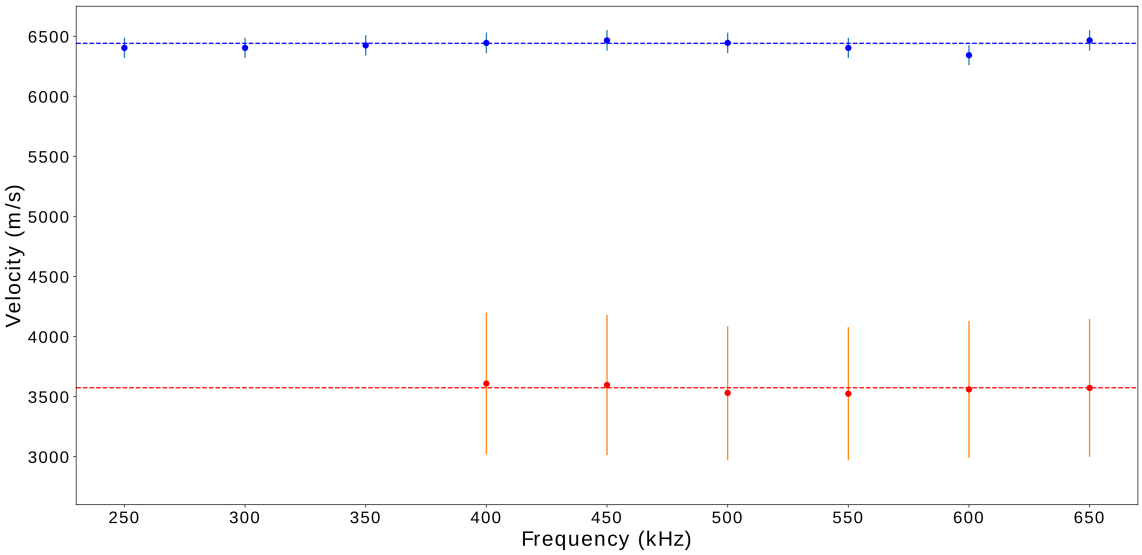

Figure A16. Measured velocity values for the *aluminum* samples (dots) for P-waves (blue) and S-waves (red). The vertical lines show the assessed uncertainty of the measurements. The horizontal dashed lines show the value considered valid for the overall frequency range of interest (250-650 kHz).

Material	**V_P (%)**	**V_S (%)**	**α_P (%)**	**α_S (%)**	**Q_P (%)**	**Q_S (%)**
resin A	0.5	12.5	0.1	26.1	0.6	39
resin B	0.6	1.9	0.1	14.8	0.8	27
resin C	0.7	5.7	0.3	21.2	0.8	26.9
glass	1	16.4	n.a.	n.a.	n.a.	n.a.
aluminum	1.4	16.4	n.a.	n.a.	n.a.	n.a.

Table A2. The maximal uncertainty of the measurements.

APPENDIX B

MESH OPTIMIZATION TO REDUCE THE SPECTRAL-ELEMENT COMPUTATIONAL COST

As mentioned in Chapter 2.3.1 in Part 1, finding the appropriate meshing strategy for a complex geometry using a non-structured hexahedral mesh is a time-consuming procedure. Thus, our goal here is to reduce the computational cost without modifying the meshing strategy. In other words, we use the same subdivision of the whole model into subdomains and the same meshing order of the different subdomains.

Our optimization takes advantage of the fact that the accuracy of the spectral-element simulations is not directly constrained by the element size, but rather by the number of GLL points per wavelength. This means that we can increase the element size and keep a similar level of accuracy of the simulations by increasing the order of the polynomial basis functions. This technique is widely discussed in the literature as *h*−, *p*−, or *h*−*p convergence*, where *h* stands for the element size and *p* denotes the polynomial order of the basis functions (e.g., Hughes, 1987, Maday and Rønquist, 1990, Seriani and Priolo, 1994, Vos et al., 2010, Oliveira and Seriani, 2011). For the initial meshing of the model we have used basis functions of order N=4, meaning that N+1=5 GLL points were used in each element.

We consider the mesh presented in Figures 13-14 as the reference for this appendix. As shown in Chapter 3, the reference mesh yields accurate synthetic results compared with the zero-offset laboratory data. When creating a non-structured mesh, the element size has a distribution as shown in Figure 14. This is due to the geometric constraints on the meshing algorithm, resulting in various element sizes. Cubit/Trelis uses a target element size because the meshing algorithm aims to mesh the model such that the average of the element sizes is close to this target value. For the reference mesh a target edge length of 1.1 mm is necessary to have the largest elements below the required threshold of 1.6 mm. For the sake of brevity, we use

relative target element sizes hereafter by considering the target element size of the reference mesh as being equal to one. We note that small changes in the target element size result in the same distribution of the element sizes, only the size of each element is multiplied by the factor of the change. According to our experience this remains true even for such a complex geometry as the Marseille-Benchie model if the change is at most a factor of 0.2-5. Because our meshing strategy involves the subdivision of the model into several subdomains, there is an upper limit to increase the element size. With our decomposition strategy, using approximately five times larger elements than the reference value is the upper limit. It comes from the fact that above this value, the element size becomes too high compared with the dimensions of some of the subdomains. We emphasize that using larger elements does not result in a less accurate representation of even the curved interfaces because curved hexahedral elements are used (Figure 11 right). It means that the numerical tool can account for curved edges and surfaces of each element, instead of only straight lines and planar surfaces (Komatitsch and Vilotte, 1998, Fichtner, 2010).

We have tested two different approaches. The first one consists of fixing the polynomial order of the basis functions and changing the element size. The second one keeps the element size fixed and changes the polynomial order. To evaluate the results, we have run the same zero-offset simulations using the different meshes and compared the resulting synthetic traces with traces obtained with the reference mesh. To evaluate the tests, we have used zero-offset traces B and C (Figures 21 and 22). To obtain a quantitative comparison, we have computed the root-mean-square (rms) difference between each synthetic trace and the reference trace. Figure B1 shows the relative computational cost and the rms misfit for different element sizes, using the sixth-order polynomial basis functions. The results suggest that the optimum is around relative element sizes of 2.25–2.5. Using smaller elements increases the computational cost, whereas using larger elements increases the rms misfit without any significant gain in the relative computational cost.

Considering that the optimal element size is approximately 2.5 (based on Figure B1), the effect of the polynomial order has to be examined as well. Figure B2 shows the relative computational cost and the rms misfit for different polynomial orders, using a relative element size of 2.5. The results show that the polynomial order of eight yields the smallest rms misfit (approximately 0.008). Even though the rms misfit is somewhat higher for order six (approximately 0.05), its computational cost is more than three times lower than that of order eight. We note that the rms misfit does not show a monotonous trend for any of the traces, neither in Figure B1 nor in Figure B2.

This is probably due to the non-structured mesh. Maday and Rønquist (1990) mathematically proved that a monotonous trend in the misfit curves can be expected only for a structured mesh, but not necessarily for a non-structured mesh.

Figure B3 shows the comparison of the traces using the optimized mesh (relative element size of 2.5) and sixth-order basis functions with the reference traces. The optimized mesh provides an excellent fit with the reference solutions in general. Due to the larger elements, some minor oscillations can be seen, probably due to mesh dispersion. However, their amplitude and difference from the reference solutions are negligible. Considering that the relative computational cost is only 15.7% of the reference simulation, we suggest using the optimized meshing strategy. Moreover, the effect of mesh dispersion can be reduced by using a relative element size of 2.25 instead of 2.5. In that case, the relative computational cost is still 25% of the reference, in return for a bit higher accuracy than with a relative element size of 2.5.

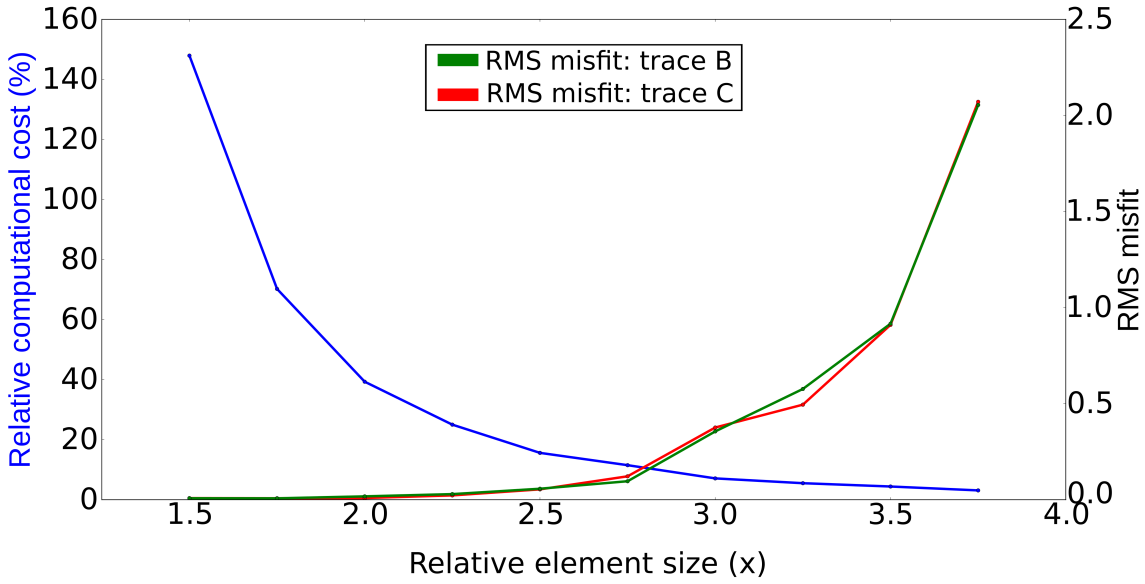

Figure B1. Relative computational cost (blue) and rms misfit (green: trace B, red: trace C) for varying element size, using the sixth-order polynomial basis functions.

APPENDIX B

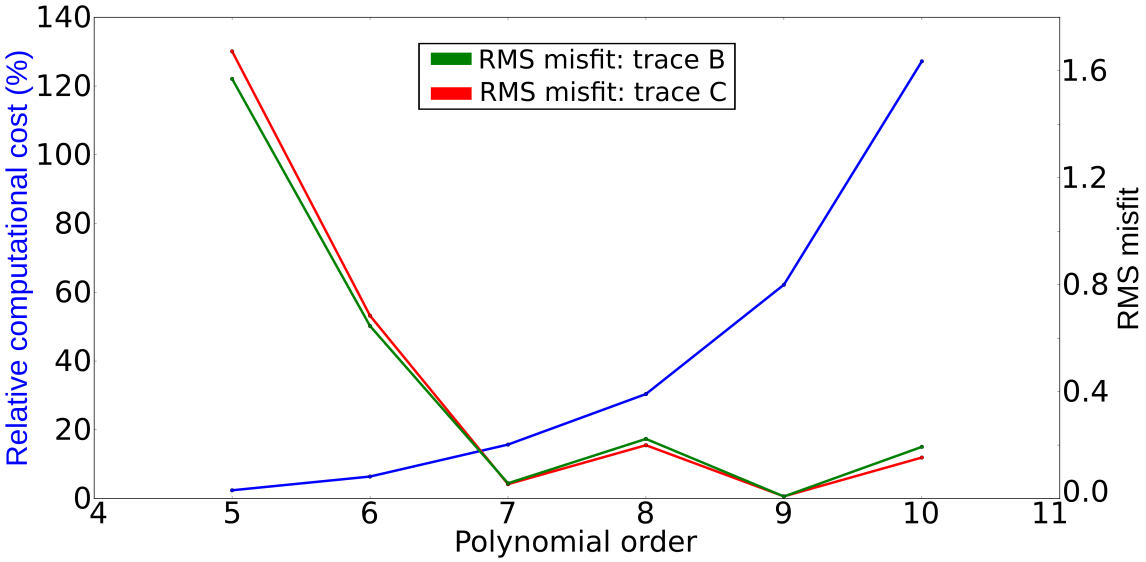

Figure B2. Relative computational cost (blue) and rms misfit (green: trace B, red: trace C) for varying order of the polynomial basis functions, using a relative element size of 2.5.

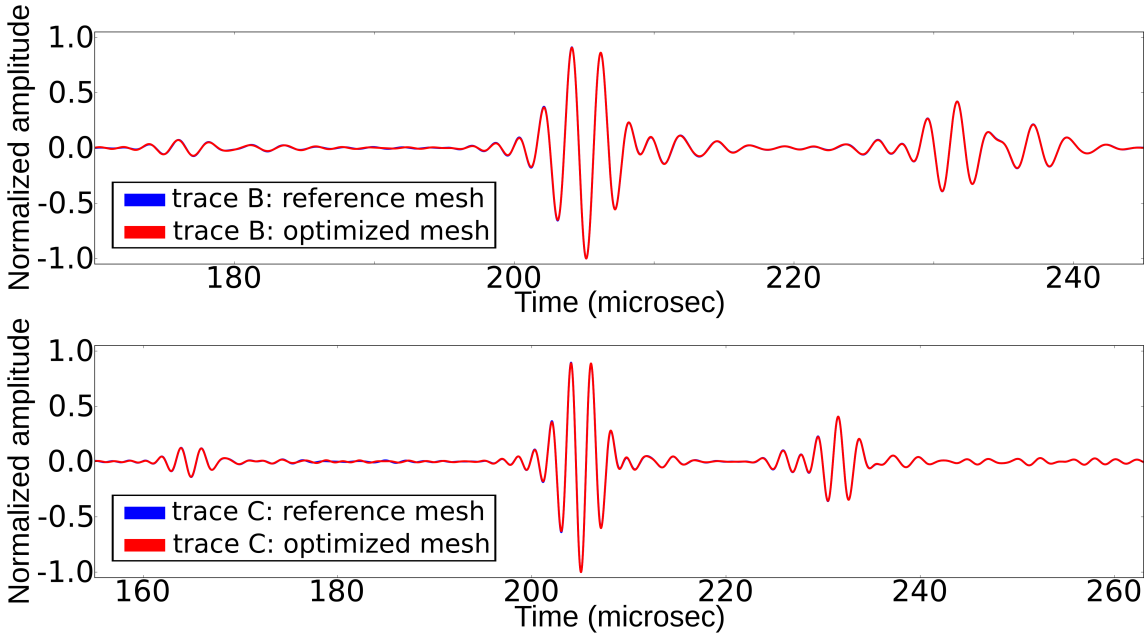

Figure B3. Comparison of zero-offset synthetic traces using the reference mesh (blue) and the optimized mesh with a relative element size of 2.5 and sixth-order basis functions (red): (a) trace B and (b) trace C.

REFERENCES

Aki, K., and Richards, P. G., 1980, Quantitative seismology, theory and methods: W. H. Freeman.

Alterman, Z., and Karal, F., 1968, Propagation of elastic waves in layered media by finite difference methods: Bulletin of the Seismological Society of America, **58**(1), 367-398.

Ammari, H., Bretin, E., Garnier, J., and Wahab, A., 2013, Time-reversal algorithms in viscoelastic media: European Journal of Applied Mathematics, **24**(4), 565–600.

Arntsen, B., Solymosi, B., Favretto-Cristini, N., Raknes, E. B., and Ursin, B., 2017, Accuracy of finite-difference modeling: ROSE Meeting, Trondheim, Norway.

Arntsen, B., Solymosi, B., Favretto-Cristini, N., Raknes, E. B., and Ursin, B., 2018, Verification of seismic modeling using laboratory ultrasonic data: ROSE Meeting, Trondheim, Norway.

Bao, H., Bielak, J., Ghattas, O., Kallivokas, L. F., O'Hallaron, D. R., Shewchuk, J. R., and Xu, J., 1998, Large-scale simulation of elastic wave propagation in heterogeneous media on parallel computers: Computer Methods in Applied Mechanics and Engineering, **152**(1-2), 85-102.

Baysal, E., Kosloff, D. D., and Sherwood, J. W., 1983, Reverse time migration: Geophysics, **48**(11), 1514-1524.

Becker, T., Elison, P., Van Manen, D.-J., Donahue, C., Greenhalgh, S., Broggini, F., and Robertsson, J., 2016, Experimental Marchenko focusing in a variable diameter sound wave tube: SEG 2016 Technical Program, SEG, pp. 5144-5148.

Ben-Menahem, A., and Singh, S. J., 1981, Seismic waves and sources: Springer-Verlag.

Berenger, J.-P., 1994, A perfectly matched layer for the absorption of electromagnetic waves: Journal of Computational Physics, **114**(2), 185-200.

REFERENCES

Blacker, T., 1994, CUBIT Mesh Generation Environment Users Manual, https://cubit.sandia.gov/public/13.2/help_manual/WebHelp/cubit_users_manual.html, accessed 03 September 2018.

Blanc, E., Komatitsch, D., Chaljub, E., Lombard, B., and Xie, Z, 2016, Highly-accurate stability-preserving optimization of the Zener viscoelastic model, with application to wave propagation in the presence of strong attenuation: Geophysical Journal International, **205**, 427-439.

Boore, D. M., 1972, Finite difference methods for seismic wave propagation in heterogeneous materials: Methods in Computational Physics, **11**, 1-37.

Bottero, A., Cristini, P., Komatitsch, D., and Asch, M., 2016, An axisymmetric time-domain spectral-element method for full-wave simulations: Application to ocean acoustics: The Journal of the Acoustical Society of America, **140**(5), 3520-3530.

Bretaudeau, F., Leparoux, D., Durand, O., and Abraham, O., 2011, Small-scale modeling of onshore seismic experiment: A tool to validate numerical modeling and seismic imaging methods: Geophysics, **76**(5), T101-T112.

Bretaudeau, F., Brossier, R., Leparoux, D., Abraham, O., and Virieux, J., 2013, 2D elastic full-waveform imaging of the near-surface: Application to synthetic and physical modelling data sets: Near Surface Geophysics, **11**(3), 307-316.

Broggini, F., Snieder, R., and Wapenaar, K., 2012, Focusing the wavefield inside an unknown 1D medium: Beyond seismic interferometry, Geophysics, **77**(5), A25-A28.

Campman, X. H., van Wijk, K., Scales, J. A., and Herman, G. C., 2005, Imaging and suppressing near-receiver scattered surface waves: Geophysics, **70**(2), V21-V29.

Capdeville, Y., Larmat, C., Vilotte, J.-P., and Montagner, J.-P., 2002, A new coupled spectral element and modal solution method for global seismology: A first application to the scattering induced by a plume-like anomaly: Geophysical Research Letters, **29**(9), 32-1-32-4.

Capdeville, Y., Chaljub, E., and Montagner, J., 2003, Coupling the spectral element method with a modal solution for elastic wave propagation in global earth models: Geophysical Journal International, **152**(1), 34-67.

Carcione, J. M., 2010, A generalization of the Fourier pseudospectral method.: Geophysics, **75**(6), A53-A56.

Carrington, L., Komatitsch, D., Laurenzano, M., Tikir, M., Michéa, D., Le Goff, N., Snavely, A., and Tromp, J., 2008, High-frequency simulations of global seismic wave propagation using SPECFEM3D GLOBE on 62 thousand processor cores: Proceedings of the 2008 ACM/IEEE Conference on Supercomputing, 1–11 (Article #60).

Casasanta, L., and Gray, S. H., 2015, Converted-wave beam migration with sparse sources or receivers: Geophysical Prospecting, **63**(3), 534-551.

Červený, V., 1987, Ray tracing algorithms in three-dimensional laterally varying layered structures in Seismic Tomography: Springer, pp. 99-133.

Červený, V., 2001, Seismic ray theory: Cambridge University Press.

Chai, X., Wang, S., Wei, J., Li, J., and Yin, H., 2015, Reflectivity inversion for attenuated seismic data: Physical modeling and field data experiments: Geophysics, **81**(1), T11-T24.

Chaljub, E., Capdeville, Y., and Vilotte, J.-P., 2003, Solving elastodynamics in a fluid–solid heterogeneous sphere: a parallel spectral element approximation on non-conforming grids: Journal of Computational Physics, **187**(2), 457-491.

Chaljub, E., Komatitsch, D., Vilotte, J.-P., Capdeville, Y., Valette, B., and Festa, G., 2007, Spectral-element analysis in seismology: Advances in Geophysics, **48**, 365-419.

Chaljub, E., Maufroy, E., Moczo, P., Kristek, J., Hollender, F., Bard, P.-Y., Priolo, E., Klin, P., De Martin, F., and Zhang, Z., 2015, 3-D numerical simulations of earthquake ground motion in sedimentary basins: testing accuracy through stringent models: Geophysical Journal International, **201**(1), 90-111.

Chang, C.-H., Chang, Y.-F., and Tseng, P.-Y., 2017, Azimuthal variation of converted-wave amplitude in a reservoir with vertically aligned fractures - a physical model study: Geophysical Prospecting, **65**(1), 221-228.

REFERENCES

Chauris, H., and Benjemaa, M., 2010, Seismic wave-equation demigration/migration: Geophysics, **75**(3), S111-S119.

Claerbout, J. F., 1971, Toward a unified theory of reflector mapping: Geophysics, **36**(3), 467-481.

Clayton, R., and Engquist, B., 1977, Absorbing boundary conditions for acoustic and elastic wave equations: Bulletin of the Seismological Society of America, **67**(6), 1529-1540.

Collino, F., and Tsogka, C., 2001, Application of the perfectly matched absorbing layer model to the linear elastodynamic problem in anisotropic heterogeneous media: Geophysics, **66**(1), 294-307.

Cooper, J. K., Lawton, D. C., and Margrave, G. F., 2010, The wedge model revisited: A physical modeling experiment: Geophysics, **75**(2), T15-T21.

Courant, R., Friedrichs, K., and Lewy, H., 1928, Über die partiellen Differenzengleichungen der mathematischen Physik: Mathematische Annalen, **100**(1), 32-74.

Cristini, P., and Komatitsch, D., 2012, Some illustrative examples of the use of a spectral-element method in ocean acoustics: The Journal of the Acoustical Society of America, **131**(3), EL229-EL235.

Dahlen, F., and Tromp, J., 1998, Theoretical global seismology: Princeton University Press.

Davis, P. J., and Rabinowitz, P., 1984, Methods of numerical integration: Courier Corporation.

De Basabe, J. D., and Sen, M. K., 2014, A comparison of finite-difference and spectral-element methods for elastic wave propagation in media with a fluid-solid interface: Geophysical Journal International, **200**(1), 278-298.

Dombradi, E., Sokoutis, D., Bada, G., Cloetingh, S., and Horvath, F., 2010, Modelling recent deformation of the Pannonian lithosphere: Lithospheric folding and tectonic topography: Tectonophysics, **484**(1-4), 103-118.

Douma, H., Yingst, D., Vasconcelos, I., and Tromp, J., 2010, On the connection between artifact filtering in reverse-time migration and adjoint tomography: Geophysics, **75**(6), S219–S223.

Ebrom, D. A., and McDonald, J. A, 1994, Seismic physical modeling: SEG.

Ekanem, A., Wei, J., Li, X.-Y., Chapman, M., and Main, I., 2013, P-wave attenuation anisotropy in fractured media: A seismic physical modelling study: Geophysical Prospecting, **61**(1), 420-433.

Emerman, S. H., and Stephen, R. A., 1983, Comment on “Absorbing boundary conditions for acoustic and elastic wave equations” by R. Clayton and B. Engquist, Bulletin of the Seismological Society of America, **73**(2), 661-665.

Emmerich, H., and Korn, M., 1987, Incorporation of attenuation into time-domain computations of seismic wave fields: Geophysics, **52**(9), 1252-1264.

Engquist, B, and Majda, A., 1977, Absorbing boundary conditions for the numerical simulation of waves: Mathematics of Computation, **31**(139), 629-651.

Evert, S., 2016, Green’s Function Retrieval and Marchenko Imaging in a Dissipative Acoustic Medium: Physical Review Letters, **116**, 164301-1-164301-6.

Faccioli, E., Maggio, F., Paolucci, R., and Quarteroni, A., 1997, 2D and 3D elastic wave propagation by a pseudo-spectral domain decomposition method: Journal of Seismology, **1**(3), 237-251.

Favretto-Anrès, N., and Rabau, G., 1997, Excitation of the Stoneley-Scholte wave at the boundary between an ideal fluid and a viscoelastic solid: Journal of Sound and Vibration, **203**(2), 193-208.

Favretto-Anrès, N., and Sessarego, J.-P., 1999, Identification of shear wave parameters of viscoelastic solids by laboratory measurements of Stoneley-Scholte waves: Acta Acustica united with Acustica, **85**(4), 505-516.

REFERENCES

Favretto-Cristini, N., Tantsereva, A., Cristini, P., Ursin, B., Komatitsch, D., and Aizenberg, A., 2014, Numerical modeling of zero-offset laboratory data in a strong topographic environment : Results for a spectral-element method and a discretized Kirchhoff integral method: Earthquake Science, **27**(4), 391-399.

Favretto-Cristini, N., Aizenberg, A. M., Ursin, B., Cristini, P., and Tantsereva, A., 2017, Analysis of Wave Scattering from a Viscoelastic Layer with Complex Shape: Journal of Computational Acoustics, **25**(3), 1750023-1-1750023-12.

Fehler, M. C., and Keliher, P. J., 2011, SEAM Phase I: Challenges of subsalt imaging in Tertiary basins, with emphasis on deepwater Gulf of Mexico: SEG.

Festa, G., Delavaud, E., and Vilotte, J.-P., 2005, Interaction between surface waves and absorbing boundaries for wave propagation in geological basins: 2D numerical simulations: Geophysical Research Letters, **32**(20), L20306.

Festa, G., and Vilotte, J.-P., 2005, The Newmark scheme as velocity–stress time-staggering: an efficient PML implementation for spectral element simulations of elastodynamics: Geophysical Journal International, **161**(3), 789-812.

Fichtner, A., 2010, Full seismic waveform modelling and inversion: Springer-Verlag.

Fichtner, A., Igel, H., Bunge, H.-P., and Kennett, B. L., 2009, Simulation and inversion of seismic wave propagation on continental scales based on a spectral-element method: Journal of Numerical Analysis, Industrial and Applied Mathematics, **4**(1-2), 11-22.

Fink, M., 1999, Time-reversed acoustics: Scientific American, **281**(5), 91-97.

French, W. S., 1974, Two-dimensional and three-dimensional migration of model-experiment reflection profiles: Geophysics, **39**(3), 265-277.

Higdon, R. L., 1991, Absorbing boundary conditions for elastic waves: Geophysics, **56**(2), 231-241.

Holberg, O., 1987, Computational aspects of the choice of operator and sampling interval for numerical differentiation in large-scale simulation of wave phenomena: Geophysical Prospecting, **35**(6), 629-655.

de Hoop, A. T., 1958, Representation theorems for the displacement in an elastic solid and their applications to elastodynamic diffraction theory, PhD thesis: Technische Hogeschool Delft.

Hooper, A., 2008, A multi-temporal InSAR method incorporating both persistent scatterer and small baseline approaches: Geophysical Research Letters, **35**(16), L16302.

Hughes, T. J., 1987, The finite element method: linear static and dynamic finite element analysis: Prentice-Hall International Inc.

Igel, H., Takeuchi, N., Geller, R. J., Megnin, C., Bunge, H.-P., Clevede, E., Dalkolmo, J., and Romanowicz, B., 2000, The COSY Project: verification of global seismic modeling algorithms: Physics of the Earth and Planetary Interiors, **119**(1-2), 3-23.

Ikelle, L. T., and Amundsen, L., 2005, Introduction to Petroleum Seismology: SEG.

Jackson, M. P., and Hudec, M. R., 2017, Salt tectonics: Principles and practice: Cambridge University Press.

Jiao, J., Lowrey, D., Willis, J., and Solano, D., 2006, An improved methodology for sub-salt velocity analysis: SEG 2006 Technical Program Expanded Abstracts, SEG, pp. 3105-3109.

Julian, B., and Gubbins, D., 1977, Three-dimensional seismic ray tracing: Journal of Geophysics, **43**, 95-113.

Kelly, K., Ward, R., Treitel, S., and Alford, R., 1976, Synthetic seismograms: a finite-difference approach: Geophysics, **41**(1), 2-27.

Kennett, B., 1981, Elastic Wave Propagation in Stratified Media in Seismic WAVE Propagation in Stratified Media: Cambridge University Press., pp. 79-167.

Keys, R. G., 1985, Absorbing boundary conditions for acoustic media: Geophysics **50**(6), 892-902.

REFERENCES

Komatitsch, D., and Vilotte, J.-P., 1998, The spectral element method: an efficient tool to simulate the seismic response of 2D and 3D geological structures: Bulletin of the Seismological Society of America, **88**(2), 368-392.

Komatitsch, D., and Tromp, J., 2002, Spectral-element simulations of global seismic wave propagation - I. Validation: Geophysical Journal International, **149**(2), 390-412.

Komatitsch, D., and Tromp, J., 2003, A perfectly matched layer absorbing boundary condition for the second-order seismic wave equation: Geophysical Journal International, **154**(1), 146-153.

Komatitsch, D., S. Tsuboi, C. Ji, and J. Tromp, 2003, A 14.6 billion degrees of freedom, 5 teraflops, 2.5 terabyte earthquake simulation on the earth simulator: Proceedings of the 2003 ACM/IEEE Conference on Supercomputing.

Komatitsch, D., Liu, Q., Tromp, J., Suss, P., Stidham, C., and Shaw, J. H., 2004, Simulations of ground motion in the Los Angeles basin based upon the spectral-element method: Bulletin of the Seismological Society of America, **94**(1), 187-206.

Komatitsch, D., Erlebacher, G., Göddeke, D., and Michéa, D., 2010, High-order finite-element seismic wave propagation modeling with MPI on a large GPU cluster: Journal of Computational Physics, **229**, 7692-7714.

Komatitsch, D., Xie, Z., Bozdag, E., Sales de Andrade, E., Peter, D., Liu, Q., and Tromp, J., 2016, Anelastic sensitivity kernels with parsimonious storage for adjoint tomography and full waveform inversion: Geophysical Journal International, **206**, 1467-1478.

Koopmann, G. H., Song, L., and Fahnline, J. B., 1989, A method for computing acoustic fields based on the principle of wave superposition: The Journal of the Acoustical Society of America **86**(6), 2433-2438.

Kosloff, D., and Baysal, E., 1982, Forward modeling by a Fourier method: Geophysics, **47**(10), 1402-1412.

Kosloff, D., Kessler, D., Filho, A., Tessmer, E., Behle, A., and Strahilevitz, R., 1990, Solution of the equations of dynamic elasticity by a Chebychev spectral method: Geophysics, **55**(6), 734-748.

Krail, P., 1993, Sub-salt acquisiton with a marine vertical cable: SEG 1993 Technical Program Expanded Abstracts, SEG, pp. 1376-1376.

Kristek, J., Moczo, P., and Galis, M., 2009, A brief summary of some PML formulations and discretizations for the velocity-stress equation of seismic motion: Studia Geophysica et Geodaetica, **53**(4), 459.

Lamb, H., 1904, On the Propagation of Tremors over the Surface of an Elastic Solid: Philosophical Transactions of the Royal Society A: Mathematical, Physical and Engineering Sciences, **203**(359-371), 1-42.

Lasaygues, P., and Pithioux, M., 2002, Ultrasonic characterization of orthotropic elastic bovine bones: Ultrasonics, **39**(8), 567-573.

Li, J., Shen, Y., and Zhang, W., 2018, Three-Dimensional Passive-Source Reverse-Time Migration of Converted Waves: The Method: Journal of Geophysical Research: Solid Earth, **123**(2), 1419-1434.

Lindsay, R. O., May Jr, W. P., and Towner, W. C., 2000, 3-D seismic investigation for sub-salt reservoir properties-onshore Republic of Yemen: SEG 2000 Technical Program Expanded Abstracts, SEG, pp. 619-622.

Liu, H.-P., Anderson, D. L., and Kanamori, H., 1976, Velocity dispersion due to anelasticity; implications for seismology and mantle composition: Geophysical Journal International, **47**(1), 41-58.

Liu, Q. , and Tromp, J., 2006, Finite-frequency kernels based on adjoint methods: Bulletin of the Seismological Society of America, **96**(6), 2383–2397.

Liu, Y., Landrø, M., Arntsen, B., van der Neut, J., Wapenaar, K., 2017, A new approach to separate seismic time-lapse time shifts in the reservoir and overburden: Geophysics, **82**(6), Q67-Q78.

Long, A., von Abendorff, E., Purves, M., and Norris, J., 2013, Simultaneous long offset (SLO) towed streamer seismic acquisition: ASEG-PESA 2013 Expanded Abstract: SEG.

REFERENCES

Luo, Y., Tromp, J., Denel, B., and Calandra, H., 2013, 3D coupled acoustic-elastic migration with topography and bathymetry based on spectral-element and adjoint methods: Geophysics, **78**(4), S193-S202.

Lysmer, J., and Drake, L. A., 1972, A finite element method for seismology: Methods in Computational Physics, **11**, 181-216.

Madariaga, R., 1976, Dynamics of an expanding circular fault: Bulletin of the Seismological Society of America: **66**(3), 639-666.

Maday, Y., and Rønquist, E. M., 1990, Optimal error analysis of spectral methods with emphasis on non-constant coefficients and deformed geometries: Computer Methods in Applied Mechanics and Engineering, **80**(1-3), 91-115.

Mahrer, K. D., 1986, An empirical study of instability and improvement of absorbing boundary conditions for the elastic wave equation: Geophysics, **51**(7), 1499-1501.

Mahrer, K. D., 1990, Numerical time step instability and Stacey's and Clayton-Engquist's absorbing
boundary conditions: Bulletin of the Seismological Society of America, **80**, 213–217.

Nagaso, M., Moysan, J., Benjeddou, S., Massacret, N., Ploix, M-A., Komatitsch, D., and Lhuillier, C., 2016, Ultrasonic thermometry simulation in a random fluctuating medium: evidence of the acoustic signature of a one-percent temperature difference: Ultrasonics, **68**, 61-70.

Mittet, R., 2002, Free-surface boundary conditions for elastic staggered-grid modeling schemes, Geophysics, **67**(5), 1616-1623.

Mittet, R., 2017, On the internal interfaces in finite-difference schemes: Geophysics, **82**(4), T159-T182.

Moczo, P., Bystrick, E., Kristek, J., Carcione, J. M., and Bouchon, M., 1997, Hybrid modeling of P-SV seismic motion at inhomogeneous viscoelastic topographic structures: Bulletin of the Seismological Society of America, **87**(5), 1305-1323.

Moczo, P., J. Ampuero, J. Kristek, S. Day, M. Kristekova, P. Pazak, M. Galis, and H. Igel, eds., 2006, Comparison of numerical methods for seismic wave propagation and source dynamics — the SPICE code validation: Proceedings of International Symposium on the Effects of Surface Geology on Seismic Motion, 3, 1–10.

Moczo, P., Kristek, J., Galis, M., Pazak, P., and Balazovjech, M., 2007, The finite-difference and finite-element modeling of seismic wave propagation and earthquake motion: Acta Physica Slovaca, **57**(2), 177-406.

Moczo, P., Kristek, J., Galis, M., and Pazak, P., 2010, On accuracy of the finite-difference and finite-element schemes with respect to P-wave to S-wave speed ratio: Geophysical Journal International, **182**(1), 493-510.

Mulder, W, 1999, Spurious modes in finite-element discretizations of the wave equation may not be all that bad: Applied Numerical Mathematics, **30**(4), 425-445.

van der Neut, J., Vasconcelos, I., and Wapenaar, K., 2015, On Green's function retrieval by iterative substitution of the coupled Marchenko equations: Geophysical Journal International, **203**(2), 792-813.

Newmark, N. M., 1959, A method of computation for structural dynamics: Journal of the Engineering Mechanics Division, **85**(3), 67-94.

Nissen-Meyer, T., Fournier, A., and Dahlen, F. A., 2007, A two-dimensional spectral-element method for computing spherical-earth seismograms – I. Moment-tensor source: Geophysical Journal International, **168**(3), 1067-1092.

Oliveira, S., and Seriani, G., 2011, Effect of element distortion on the numerical dispersion of spectral element methods: Communications in Computational Physics, **9**(4), 937-958.

Oropeza, S., Sarrazin, I., and Campos, R., 2009, Sub-Salt AVO and Seismic Inversion analysis: An example from deep water, Gulf of Mexico, in '11th International Congress of the Brazilian Geophysical Society & EXPOGEF 2009, Salvador, Bahia, Brazil, 24-28 August 2009', pp. 182-185.

REFERENCES

Pageot, D., D. Leparoux, M. Le Feuvre, O. Durand, P. Côte, and Y. Capdeville, 2017, Improving the seismic small-scale modelling by comparison with numerical methods: Geophysical Journal International, **211**, 637-649.

Pant, D., Greenhalgh, S., and Zhou, B., 1992, Physical and numerical model study of diffraction effects on seismic profiles over simple structures: Geophysical Journal International, **108**(3), 906-916.

Patera, A. T., 1984, A spectral element method for fluid dynamics: laminar flow in a channel expansion: Journal of Computational Physics, **54**(3), 468-488.

Peter, D., D. Komatitsch, Y. Luo, R. Martin, N. Le Goff, E. Casarotti, P. Le Loher, F. Magnoni, Q. Liu, C. Blitz, T. Nissen-Meyer, P. Basini, and J. Tromp, 2011, Forward and adjoint simulations of seismic wave propagation on fully unstructured hexahedral meshes: Geophysical Journal International, **186**, 721-739.

Pratt, R. G., 1999, Seismic waveform inversion in the frequency domain, Part I: Theory and verification in a physical scale model: Geophysics, **64**(3), 888-901.

Quarteroni, A., Tagliani, A., and Zampieri, E., 1998, Generalized Galerkin approximations of elastic waves with absorbing boundary conditions: Computer Methods in Applied Mechanics and Engineering, **163**(1-4), 323-341.

Ravasi, M., Vasconcelos, I., Kritski, A., Curtis, A., Filho, C. A. d. C., and Meles, G. A., 2016, Target-oriented Marchenko imaging of a North Sea field: Geophysical Supplements to the Monthly Notices of the Royal Astronomical Society, **205**(1), 99-104.

Ravaut, C., Alerini, M., Pannetier-Lescoffit, S., and Thomassen, E., 2008, Sub-salt imaging by full-waveform inversion: a parameter analysis: SEG 2008 Technical Program Expanded Abstracts, SEG, pp. 1940-1944.

Rawlinson, N., Hauser, J., and Sambridge, M., 2008, Seismic ray tracing and wavefront tracking in laterally heterogeneous media: Advances in Geophysics, **49**, 203-273.

Robertsson, J. O., Bednar, B., Blanch, J., Kostov, C., and van Manen, D.-J., 2007, Introduction to the supplement on seismic modeling with applications to acquisition, processing, and interpretation: Geophysics, **72**(5), SM1-SM4.

Seriani, G., and Priolo, E., 1994, Spectral element method for acoustic wave simulation in heterogeneous media: Finite Elements in Analysis and Design, **16**(3-4), 337-348.

Seriani, G., Priolo, E., Pregarz, A., and Cohen, G., 1995, Modelling waves in anisotropic media by a spectral element method, in Proceedings of the third international conference on mathematical and numerical aspects of wave propagation, pp. 289-298.

Seriani, G., 1998, 3-D large-scale wave propagation modeling by spectral element method on Cray T3E multiprocessor, Computer Methods in Applied Mechanics and Engineering, **164**(1-2), 235-247.

Shepherd, J. F., and Johnson, C. R., 2008, Hexahedral mesh generation constraints: Engineering with Computers, **24**(3), 195-213.

Sherlock, D., McKenna, J., and Evans, B., 2000, Time-lapse 3-D seismic physical modelling: Exploration Geophysics, **31**, 310-314.

Solymosi, B., Favretto-Cristini, N., Monteiller, V., Cristini, P., Ursin, B., Komatitsch, D., and Arntsen, B., 2017, Comparing spectral-element numerical results with laboratory data: an example for a topographical model: 79th EAGE Conference & Exhibition, Extended Abstract, EAGE, We B4 02.

Solymosi, B., Favretto-Cristini, N., Monteiller, V., Komatitsch, D., Cristini, P., Arntsen, B., and Ursin, B., 2018, How to adapt numerical simulation of wave propagation and ultrasonic laboratory experiments to be comparable - A case study for a complex topographic model: Geophysics, **83**(4), T195-T207.

Stacey, R., 1988, Improved transparent boundary formulations for the elastic-wave equation: Bulletin of the Seismological Society of America, **78**(6), 2089-2097.

REFERENCES

Staten, M. L., Kerr, R. A., Owen, S. J., Blacker, T. D., Stupazzini, M., and Shimada, K., 2010, Unconstrained plastering - Hexahedral mesh generation via advancing-front geometry decomposition: International Journal for Numerical Methods in Engineering, **81**(2), 135-171.

Stewart, R. R., Dyaur, N., Omoboya, B., De Figueiredo, J., Willis, M., and & Sil, S., 2012, Physical modeling of anisotropic domains: Ultrasonic imaging of laser-etched fractures in glass: Geophysics, **78**(1), D11-D19.

Tang, B., Xu, S., and Zhang, Y., 2011, Aliasing in RTM 3D angle gathers: SEG 2011 Technical Program Expanded Abstracts, SEG, pp. 3310-3314.

Tantsereva, A., Ursin, B., Favretto-Cristini, N., Cristini, P., and Aizenberg, A. M., 2014a, Numerical modeling of 3D zero-offset laboratory data by a discretized Kirchhoff integral method: Geophysics, **79**(2), T77-T90.

Tantsereva, A., Ursin, B., Favretto-Cristini, N., Cristini, P., and Aizenberg, A. M., 2014b, Erratum to: "Numerical modeling of 3D zero-offset laboratory data by a discretized Kirchhoff integral method": Geophysics, **79**(5), Y3-Y4.

Tari, G., Molnar, J., and Ashton, P., 2003, Examples of salt tectonics from West Africa: a comparative approach: Geological Society, London, Special Publications, **207**(1), 85-104.

Tessmer, E., and Kosloff, D., 1994, 3-D elastic modeling with surface topography by a Chebychev spectral method: Geophysics, **59**(3), 464-473.

Toshinawa, T., and Ohmachi, T., 1992, Love-wave propagation in a three-dimensional sedimentary basin: Bulletin of the Seismological Society of America, **82**(4), 1661-1677.

Tromp, J., Tape, C., and Liu, Q., 2005, Seismic tomography, adjoint methods, time reversal and banana-doughnut kernels: Geophysical Journal International, **160**(1), 195-216.

Tromp, J., Komatitsch, D., and Liu, Q., 2008, Spectral-element and adjoint methods in seismology: Communications in Computational Physics, **3**(1), 1–32.

Virieux, J., 1984, SH-wave propagation in heterogeneous media: Velocity-stress finite-difference method: Geophysics, **49**(11), 1933-1942.

Virieux, J., 1986, P-SV wave propagation in heterogeneous media: Velocity-stress finite-difference method: Geophysics, **51**(4), 889-901.

Virieux, J., and Farra, V., 1991, Ray tracing in 3-D complex isotropic media: an analysis of the problem: Geophysics, **56**(12), 2057-2069.

Virieux, J., Calandra, H., and Plessix, R.-É., 2011, A review of the spectral, pseudo-spectral, finite-difference and finite-element modelling techniques for geophysical imaging: Geophysical Prospecting, **59**(5), 794-813.

Virieux, J., and Operto, S., 2009, An overview of full-waveform inversion in exploration geophysics: Geophysics, **74**(6), WCC1-WCC26.

Vos, P. E., Sherwin, S. J., and Kirby, R. M., 2010, From h to p efficiently: Implementing finite and spectral/hp element methods to achieve optimal performance for low-and high-order discretisations: Journal of Computational Physics, **229**(13), 5161-5181.

Wapenaar, C., and Berkhout, A., 1987, Three-dimensional target-oriented pre-stack migration, First Break, **5**(6), 217-227.

Wapenaar, K., Thorbecke, J., Van Der Neut, J., Broggini, F., Slob, E., and Snieder, R., 2014, Marchenko imaging: Geophysics, **79**(3), WA39-WA57.

Xie, Z., Matzen, R., Cristini, P., Komatitsch, D., and Martin, R., 2016, A perfectly matched layer for fluid-solid problems: Application to ocean-acoustics simulations with solid ocean bottoms: Journal of the Acoustical Society of America, **140**(1), 165-175.

Xu, C., Di, B., and Wei, J., 2016, A physical modeling study of seismic features of karst cave reservoirs in the Tarim Basin, China: Geophysics, **81**(1), B31-B41.

Yilmaz, O., 1987, Seismic Data Processing: SEG.

REFERENCES

Zemanek, J., 1971, Beam behavior within the nearfield of a vibrating piston: Journal of the Acoustical Society of America, **49**(1B), 181-191.

Zhang, Y., Zhang, G., and Bleistein, N., 2003, True amplitude wave equation migration arising from true amplitude one-way wave equations: Inverse Problems, **19**(5), 1113-1138.

Zheng, Y., and Huang, X., 2002, Anisotropic perfectly matched layers for elastic waves in cartesian and curvilinear coordinates: Technical report, Massachusetts Institute of Technology, Earth Resources Laboratory.

Zhu, H., Luo, Y, Nissen-Meyer, T., Morency, C., and Tromp, J., 2009, Elastic imaging and time-lapse migration based on adjoint methods: Geophysics, **74**(6), WCA167-WCA177.